IOWA STATE UNIVERSITY
Digital Repository

2003

Investigations of the electronic properties and surface structures of aluminum-rich quasicrystalline alloys

Jason A. Barrow
Iowa State University

Follow this and additional works at: https://lib.dr.iastate.edu/rtd

Part of the <u>Analytical Chemistry Commons</u>, <u>Materials Science and Engineering Commons</u>, and the <u>Physical Chemistry Commons</u>

Investigations of the electronic properties and surface structures of aluminum-rich quasicrystalline alloys

by

Jason A. Barrow

A dissertation submitted to the graduate faculty

in partial fulfillment of the requirements for the degree of

DOCTOR OF PHILOSOPHY

Major: Analytical Chemistry

Program of Study Committee:
Patricia A. Thiel, Major Professor
Daniel J. Sordelet
Jacob W. Petrich
Mei Hong
Valerie V. Sheares-Ashby

Iowa State University

Ames, Iowa

2003

ii

Graduate College

Iowa State University

This is to certify that the doctoral dissertation of

Jason A. Barrow

has met the dissertation requirements of Iowa State University

Major Professor

For the Major Program

This work is dedicated to Christa, my loving and supportive wife.

You have always been, and will always be my true companion.

TABLE OF CONTENTS

GENERAL INTRODUCTION

In classical crystallography, any crystal structure may be described by a representative unit of the structure [1]. This unit cell must contain all of the symmetry elements of the crystal structure and must describe the entire crystal by periodic translation to produce an infinite lattice array. Thus, a crystal possesses a short-range order, described by the symmetry elements, and a long-range order imposed by the translational symmetry. The requirement of translational symmetry leads to certain rotational symmetries that are forbidden. Specifically, crystals cannot possess a five-fold or higher than a six-fold rotational axis of symmetry.

In 1982, Shechtman et al., discovered an Al_6Mn intermetallic with icosahedral symmetry [2]. Since an icosahedron contains 12 five-fold rotational axes, this discovery did not fit into the classical description of crystals, yet the intermetallic produced sharp diffraction patterns. Shechtman et al., claimed to have discovered a new form of matter, termed quasicrystals, that did not have translational order, yet possessed nearly perfect long-range orientational order which accounted for these sharp diffraction patterns. This discovery was initially viewed with much skepticism, and in the years that followed it was argued that the observed diffraction was due to icosahedral twinning of cubic structures [3-5]. By the early nineties it was generally accepted that quasicrystals were, in fact, aperiodic structures with long-range symmetry. In 1992, the International Union of Crystallography broadened the definition of "crystal" to include "any solid having essentially discrete diffraction patterns"[6]. Given this, quasicrystals could now simply be called "crystals";

however, the scientific community still refers to them as "quasicrystals" to distinguish them from traditional periodic crystals.

Since their initial discovery, several stable quasicrystals have been identified [7]. Quasicrystals are typically binary or ternary intermetallics and are often aluminum rich. Two common groups of quasicrystals are the icosahedral group and the decagonal group. Icosahedral quasicrystals are quasiperiodic in three dimensions. Decagonal quasicrystals are quasiperiodic in only two dimensions. They are a periodic stacking of quasicrystalline planes. Researchers have had the most success growing large single grain samples of icosahedral Al-Cu-Fe, icosahedral Al-Pd-Mn, and decagonal Al-Ni-Co. Consequently, these are among the most commonly studied systems.

As compared to crystalline intermetallics of similar composition, the physical and electronic properties of quasicrystals are very unusual. For example, all known quasicrystals are relatively hard and brittle. The Vickers' hardness is generally between 700-1000, which is in the same range as silica (750-1200) [8-12]. For comparison, the Vickers' hardness of aluminum, copper, and low-carbon steel is only 25-45, 40-105, and 70-200, respectively [8, 9].

Another unexpected property of quasicrystals is low thermal conductivity. The thermal conductivity of icosahedral Al-Cu-Fe is only 2 W m^{-1} K^{-1} [10]. This is nearly the same as the ceramic, yttria-doped zirconia [10]. Again, when compared to aluminum, copper, and low-carbon steel (170 W m^{-1} K^{-1}, 390 W m^{-1} K^{-1}, 50 W m^{-1} K^{-1}), we find that the quasicrystalline properties are anomalous [10, 13]. Other atypical properties include low electrical conductivity, low coefficients of friction, and low surface energy [14].

The nature of the relationship between the quasicrystalline atomic structure and their unique combination of properties has not been firmly established. Since there are many promising applications, there have been extensive fundamental research efforts aimed at understanding this relationship. A key point to understanding the properties of quasicrystals is the determination of their atomic structure. Although many bulk models have been proposed to describe the structure of quasicrystals, no one model has been universally accepted.

Since decagonal quasicrystals are only aperiodic in two dimensions, they have been described using tiling models. The quasi-unit-cell tiling model consists of a single repeating decagonal unit [15-18]. This unit cell differs from those in classical crystallography, in that it can overlap. To create a quasiperiodic surface, these tiles must overlap according to a specific set of matching rules. An alternative model is based on Penrose-like tilings [19-22]. This method does not require overlap, but two different types of tiles are necessary. These tiles also require a set of matching rules to create a quasiperiodic surface. Both of these types of models have successfully described two dimensional aperiodicity, but it should be noted that these are geometric descriptions only and do not describe the atomic bonding.

Aluminum-rich icosahedral quasicrystals have been described using cluster based models. Models have been proposed using pseudo-Mackay icosahedral or Bergman type clusters as a basic motif for the quasicrystalline structure [23-25]. The Bergman type cluster model requires one cluster with the composition $Al_{23}Pd_7Mn_3$ [25]. The pseudo-Mackay cluster model uses three different types of basic clusters: $Al_{38}Pd_7Mn_6$, $Al_{31}Pd_{20}$, and $Al_{30}Pd_{21}$ [23, 24]. It is argued that these clusters are energetically stable units which are related by inflation matching rules to generate three-dimensional quasiperiodicity.

There is experimental evidence to support the idea of cluster-based structures. Measurements of the electrical and thermal properties of quasicrystals suggest a hierarchical localization, which is consistent with the electron localization inherent to a cluster [24]. In addition, the cleavage properties and plasticity of quasicrystals have been interpreted in the context of stable clusters acting as structural sub-units [26, 27].

To date, it is still not clear whether the Bergman and the pseudo-Mackay clusters are inherently stable structures or if they are simply a geometric coincidence. While it is possible to describe the bulk structure of quasicrystalline materials with these cluster models, it requires complex rules for overlapping and interlacing the clusters [24]. If clusters are considered to be energetically stable units, it is difficult to explain how they would actually assemble during growth to form a quasicrystalline structure. Alternatively, the clusters may only be geometric structures with no special stability whatsoever. In this dissertation, we report a study of gas-phase metal clusters made from a quasicrystalline material in an attempt to address the issue of cluster stability.

Another important area of quasicrystal research is the study of the bulk transport properties. Decagonal quasicrystals are often used for these studies because it allows one to comparatively study the quasicrystalline and crystalline transport properties along different directions of the same sample. Most of the studies performed so far have been done at temperatures below 300 K. This has provided valuable information regarding the intrinsic transport properties of quasicrystals. The electronic and phonon conductivity contributions have been determined as well as the Debye temperature [28-31]. Low temperature studies have also provided information about phonon scattering mechanisms and the effects of impurities [29, 30, 32, 33]. While these are important results, it is equally important to

investigate the electronic and thermal properties at higher temperatures, as many of the potential applications of quasicrystals would be at or above room temperature. To address this, we present the first high-temperature thermal conductivity studies done on the decagonal Al-Ni-Co system.

Quasicrystals have also drawn considerable interest from the field of surface science. Surface techniques such as scanning tunneling microscopy, auger electron spectroscopy, x-ray photoemission spectroscopy, and electron diffraction have been employed to investigate the nature of the quasicrystalline surface. These types of studies typically require a clean, well prepared surface if valid results are to be obtained. Such experiments must be done under ultra-high vacuum (UHV) conditions if the surface is to remain free of contaminants for the duration of the experiment.

There are three common methods that have been employed for cleaning the quasicrystal surface in UHV. The first is to fracture the sample in-situ. Because quasicrystals are brittle, this works well and exposes a surface that has been protected from contamination by the bulk; however, the surface produced is a non-equilibrium surface and does not necessarily represent the favored surface termination. Another method for surface preparation is mechanical scraping. While this method can remove surface contaminants, it also produces structural disorder on the surface. The most reliable method for obtaining a reproducibly clean, bulk-terminated quasicrystalline surface is to use cycles of sputtering and annealing. When sputtering, the surface is bombarded with a high-energy beam of noble-gas ions. This removes contaminants from the surface, but also destroys the quasicrystalline structure. Additionally, it is well known that sputtering causes a change in the surface composition due to preferential removal of the lighter elements, i.e., aluminum

[34-37]. It has been shown that annealing at the proper temperature will restore the bulk surface composition and recover the quasicrystalline surface [38-48].

Surface studies of quasicrystals can be used to examine the important issue of electronic structure. The electronic structure affects the physical properties and is related to the fundamental issue of the stabilization of these unique atomic structures. Although quasicrystals are metallic, electronic structure calculations show that they have a low density of states at the Fermi energy. This is often referred to as a pseudo-gap. The initial calculations were done using a nearly free-electron approximation. From these, it was concluded that a pseudo-gap should exist in quasicrystals [49-55]. Later, modern electron structure calculations were used to bolster the prediction that quasicrystals contain a pseudo-gap [56-70]. It should be noted that these type of structure calculations are not done on quasicrystalline systems directly, because the aperiodic structure leads to open boundary conditions. Instead, the calculations are done on large unit-cell crystalline approximants. Conclusions regarding the quasicrystalline electronic structure are inferred from these results.

Experimental investigation of the band structure at the Fermi energy has been performed by various research groups. Recent evidence suggests that the icosahedral Zn-Mg-Ho and Zn-Mg-Y quasicrystals both have pseudo-gaps at their Fermi edges [71]. A pseudo-gap has also been reported for the decagonal Al-Ni-Co quasicrystal [72, 73]. Early experiments aimed at probing the density of states of the icosahedral Al-Pd-Mn quasicrystal showed conflicting results [74-76]. It was initially thought that the discrepancies were due to differences in sample temperature, but it was later determined that the observation of the pseudo-gap is dependent on the surface preparation technique employed [75]. Results

obtained after mechanical scraping did not show a pseudo-gap, presumably because the disruption of the quasicrystalline surface smeared out the fine structure of the photoemission spectra. On the other hand, when the surface is prepared by cycles of sputtering and annealing, experimental evidence clearly demonstrates that the icosahedral Al-Pd-Mn quasicrystal does indeed have a pseudo-gap [77-80]. Studies of the icosahedral Al-Cu-Fe surface have also demonstrated a pseudo-gap. However, these experiments were done on poly-grain samples, and surface preparation was done by mechanical scraping [75, 81]. No experiments have yet been reported for a single-grain surface prepared by sputtering and annealing. To provide insight into the electronic structure of a sample whose surface is prepared in a more controlled manner, we present a comprehensive study of the single-grain icosahedral Al-Cu-Fe five-fold surface. This study demonstrates that a reduced density of states at the Fermi edge is intrinsic to the quasicrystalline Al-Cu-Fe surface.

Dissertation Organization

Four papers are included in this dissertation. The first paper, "Analysis of Gas Phase Cluster Formation from Laser-Vaporized Icosahedral Al-Pd-Mn" appears in the Proceedings of the Material Research Society, Quasicrystals: Preparation, Properties and Applications, Volume 643, Symposium K5.4, 2001. The second paper, "Analysis of Gas-Phase Clusters Made from Laser-Vaporized Icosahedral Al-Pd-Mn" appears in Volume 106(40) of the Journal of Physical Chemistry A on pages 9204-9208, 2002. The third paper, "High-Temperature Thermal Transport Properties of a Single Grain Decagonal $Al_{74}Ni_{10}Co_{16}$ Quasicrystal" will be published in Physical Review B. The last paper, "Photoemission Studies of the Sputter-induced Phase Transformation on the Al-Cu-Fe Surface" will be

published in Surface Science. Following this paper are General Conclusions and the appendices. The first appendix reports the related paper "Palladium Clusters formed on the Complex Pseudo Ten-fold Surface of the ξ'-$Al_{77.5}Pd_{19}Mn_{3.5}$ Approximant Crystal" which has been submitted to Surface Science. The second appendix is an organized record of the data collected for each research project.

References

(1)   Azaroff, L. *Introduction to Solids*; McGraw-Hill Book Company, Inc.: New York, 1960.

(2)   Shechtman, D.; Blech, I.; Gratias, D.; Cahn, J. W. *Phys. Rev. Lett.* **1984**, *53*, 1951-1953.

(3)   Pauling, L. In *Phys. Rev. Lett.*, 1987; Vol. 58, pp 365-368.

(4)   Pauling, L. In *Proc. Natl. Acad. Sci. U. S. A.*, 1988; Vol. 85, pp 8376-8380.

(5)   Pauling, L. In *Phys. Rev. B: Condens. Matter*, 1989; Vol. 39, pp 1964-1965.

(6)   Crystallography, I. U. o. In *Acta Crystallographia*, 1992; Vol. A48, pp 922.

(7)   Janot, C. *Quasicrystals: A Primer, Second Edition*; Oxford University Press: Oxford, 1995.

(8)   Hutchings, I. M. *Tribology: Friction and wear of engineering materials*; CRC: Boca Raton, 1992.

(9)   *Chemical Engineers' Handbook*; McGraw-Hill Book: New York, 1973.

(10)   Dubois, J. M.; Weinland, P.: Eur. Patent 0356287 A1 and U.S. Patent 5,204,191, April 20, 1993.

(11)   Koster, U.; Liu, W.; Liebertz, H.; Michel, M. *Journal of Non-crystalline Solids* **1993**, *153-154*, 446-452.

(12)   Yokoyama, Y.; Inoue, A.; Masumoto, T. In *Mater. Trans., JIM*, 1993; Vol. 34, pp 135-145.

(13)   *Metals Handbook: Desk Edition*; Am. Soc. for Metals: Metals Park, OH, 1984.

(14)   Jenks, C. J.; Thiel, P. A. In *Langmuir*, 1998; Vol. 14, pp 1392-1397.

(15)   Steurer, W.; Haibach, T.; Zhang, B.; Kek, S.; Lueck, R. *Acta Crystallogr., Sect. B: Struct. Sci.* **1993**, *B49*, 661-675.

(16)   Steinhardt, P. J.; Jeong, H. C.; Saitoh, K.; Tanaka, M.; Abes, E.; Tsai, A. P. In *Nature (London)*, 1998; Vol. 396, pp 55-57.

(17)   Yan, Y.; Pennycook, S. J.; Tsai, A. P. In *Phys. Rev. Lett.*, 1998; Vol. 81, pp 5145-5148.

(18)   Cockayne, E. *Mat. Sci. Eng. A* **2000**, *294-296*, 224-227.

(19)   Gummelt, P. *Geometr. Decdic.* **1996**, *62*, 1.

(20)   Ritsch, S.; Beeli, C.; Nissen, H. U.; Godecke, T.; Scheffer, M.; Luck, R. In *Philos. Mag. Lett.*, 1996; Vol. 74, pp 99-106.

(21)   Jeong, H.-C.; Steinhardt, P. J. In *Phys. Rev. B: Condens. Matter*, 1997; Vol. 55, pp 3520-3532.

(22)   Henley, C. L.; Mihalkovic, M.; Widom, M. *Journal of Alloys and Compounds* **2002**, *342*, 221-227.

(23)   Janot, C.; de Boissieu, M. *Phys. Rev. Lett.* **1994**, *72*, 1674-1677.

(24)   Janot, C. *Phys. Rev. B: Condens. Matter* **1996**, *53*, 181-191.

(25)   Elser, V. *Philos. Mag. B* **1996**, *73*, 641-656.

(26)   Ebert, P.; Feuerbacher, M.; Tamura, N.; Wollgarten, M.; Urban, K. *Phys. Rev. Lett.* **1996**, *77*, 3827-3830.

(27)   Feuerbacher, M.; Metzmacher, C.; Wollgarten, M.; Urban, K.; Baufeld, B.; Bartsch, M.; Messerschmidt, U. *Mat. Sci. Eng. A.* **1997**, *233*, 103-110.

(28)   Dian-lin, Z.; Shao-chun, C.; Yun-ping, W.; Li, L.; Xue-mei, W. *Phys. Rev. Lett.* **1991**, *66*, 2778-2781.

(29)   Matsukawa, M.; Yoshizawa, M.; Noto, K.; Yokoyama, Y.; Inoue, A. In *Quasicryst., Proc. Int. Conf., 6th*, 1998, pp 479-482.

(30)   Martin, S.; Hebard, A. F.; Kortan, A. R.; Thiel, F. A. In *Phys. Rev. Lett.*, 1991; Vol. 67, pp 719-722.

(31)   Inaba, A.; Lortz, R.; Meingast, C.; Guo, J. Q.; Tsai, A.-P. *Journal of Alloys and Compounds* **2002**, *342*, 302-305.

(32)   Legault, S.; Ellman, B.; Strom-Olsen, J. O.; Taillefer, L.; Kycia, S.; Lograsso, T.; Delaney, D. In *New Horiz. Quasicrystals, [Conf.]*, 1997, pp 224-231.

(33)   Edagawa, K.; Chernikov, M. A.; Bianchi, A. D.; Felder, E.; Gubler, U.; Ott, H. R. In *Phys. Rev. Lett.*, 1996; Vol. 77, pp 1071-1074.

(34)   Schaub, T. M.; Burgler, D. E.; Guntherodt, H. J.; Suck, J. B. Z. *Phys. B* **1994**, *96*, 93.

(35)   Chang, S. L.; Chin, W. B.; Zhang, C. M.; Jenks, C. J.; Thiel, P. A. *Surf. Sci.* **1995**, *337*, 135-146.

(36)   Suzuki, S.; Waseda, Y.; Tamura, N.; Urban, K. In *Scr. Mater.*, 1996; Vol. 35, pp 891-895.

(37)   Rouxel, D.; Gavatz, M.; Pigeat, P.; Weber, B. In *New Horiz. Quasicrystals, [Conf.]*, 1997, pp 173-180.

(38)   Thiel, P. A.; Goldman, A. I.; Jenks, C. J. In *Physical Properties of Quasicrystals*, 1999; Vol. 126, pp 327-359 and references therein.

(39)   Capitan, M. J.; Alvarez, J.; Joulaud, J. L.; Calvayrac, Y. *Surface Science* **1999**, *423*, L251-L257.

(40)   Shen, Z.; Stoldt, C. R.; Jenks, C. J.; Lograsso, T. A.; Thiel, P. A. *Phys. Rev. B* **1999**, *60*, 14688-14694.

(41)   Cappello, G.; Schmithusen, F.; Chevrier, J.; Comin, F.; Stierle, A.; Formoso, V.; De Boissieu, M.; Boudard, M.; Lograsso, T.; Jenks, C.; Delaney, D. *Mat. Sci. Eng. A* **2000**, *294-296*, 822-825.

(42)   Ledieu, J.; McGrath, R.; Diehl, R. D.; Lograsso, T. A.; Delaney, D. W.; Papadopolos, Z.; Kasner, G. *Surface Science* **2001**, *492*, L729-L734.

(43)   Naumovic, D.; Aebi, P.; Schlapbach, L.; Beeli, C. *Mat. Sci. Eng. A* **2000**, *294-296*, 822-885.

(44) Schmithusen, F.; Boissieu, M. D.; Boudard, M.; Chevrier, J.; Comin, F. *Materials Science & Engineering, A: Structural Materials: Properties, Microstructure and Processing* **2000**, *A294-296*, 867-870.

(45) Shen, Z.; Raberg, W.; Heinzig, M.; Jenks, C. J.; Fournee, V.; Van Hove, M. A.; Lograsso, T. A.; Delaney, D.; Cai, T.; Canfield, P. C.; Fisher, I. R.; Goldman, A. I.; Kramer, M. J.; Thiel, P. A. *Surface Science* **2000**, *450*, 1-11.

(46) Cai, T.; Shi, F.; Shen, Z.; Gierer, M.; Goldman, A. I.; Kramer, M. J.; Jenks, C. J.; Lograsso, T. A.; Delaney, D. W.; Thiel, P. A.; Van Hove, M. A. *Surface Science* **2001**, *495*, 19-34.

(47) Barbier, L.; Le Floc'h, D.; Calvayrac, Y.; Gratias, D. *Physical Review Letters* **2002**, *88*, 085506/085501-085506/085504.

(48) Papadopolos, Z.; Kasner, G.; Ledieu, J.; Cox, E. J.; Richardson, N. V.; Chen, Q.; Diehl, R. D.; Lograsso, T. A.; Ross, A. R.; McGrath, R. *Phys. Rev. B* **2002**, *66*, 184207/184201-184207/184213.

(49) Smith, A. P.; Ashcroft, N. W. In *Phys. Rev. Lett.*, 1987; Vol. 59, pp 1365-1368.

(50) Friedel, J.; Denoyer, F. In *C. R. Acad. Sci., Ser. 2*, 1987; Vol. 305, pp 171-174.

(51) Friedel, J. In *Helv. Phys. Acta*, 1988; Vol. 61, pp 538-556.

(52) Vaks, V. G.; Kamyshenko, V. V.; Samolyuk, G. D. In *Phys. Lett. A*, 1988; Vol. 132, pp 131-136.

(53) Friedel, J. In *Philos. Mag. B*, 1992; Vol. 65, pp 1125-1129.

(54) Fradkin, M. A. In *J. Phys.: Condens. Matter*, 1992; Vol. 4, pp 10497-10502.

(55) Carlsson, A. E. In *Phys. Rev. B: Condens. Matter*, 1993; Vol. 47, pp 2515-2521.

(56) Fujiwara, T. In *Phys. Rev. B: Condens. Matter*, 1989; Vol. 40, pp 942-946.

(57) Fujiwara, T.; Yokokawa, T. In *Phys. Rev. Lett.*, 1991; Vol. 66, pp 333-336.

(58) Hafner, J.; Krajci, M. In *Europhys. Lett.*, 1992; Vol. 17, pp 145-150.

(59) Hafner, J.; Krajci, M. In *Phys. Rev. B: Condens. Matter*, 1993; Vol. 47, pp 11795-11809.

(60) Trambly de Laissardiere, G.; Fujiwara, T. In *Phys. Rev. B: Condens. Matter*, 1994; Vol. 50, pp 5999-6005.

(61) Windisch, M.; Krajci, M.; Hafner, J. In *J. Phys.: Condens. Matter*, 1994; Vol. 6, pp 6977-6995.

(62) Krajci, M.; Hafner, J. In *Europhys. Lett.*, 1994; Vol. 27, pp 147-152.

(63) Krajci, M.; Windisch, M.; Hafner, J.; Kresse, G. In *Phys. Rev. B: Condens. Matter*, 1995; Vol. 51, pp 17355-17378.

(64) Hennig, R. G.; Teichler, H. In *Philos. Mag. A*, 1997; Vol. 76, pp 1053-1064.

(65) Roche, S.; Fujiwara, T. In *Phys. Rev. B: Condens. Matter Mater. Phys.*, 1998; Vol. 58, pp 11338-11344.

(66) Krajci, M.; Hafner, J. In *Phys. Rev. B: Condens. Matter Mater. Phys.*, 1999; Vol. 59, pp 8347-8350.

(67) Fujiwara, T. In *Springer Ser. Solid-State Sci.*, 1999; Vol. 126, pp 169-207.

(68) Krajci, M.; Hafner, J. *J. Phys.: Condens. Matter* **2000**, *12*, 5831.

(69) Krajci, M.; Hafner, J. *J. Phys.: Condens. Matter* **2002**, *13*, 3817.

(70) Krajci, M.; Hafner, J. *Phys. Rev. B* **2003**, *67*, 052201/052201-052201/052204.

(71)   Suchodolskis, A.; Assmus, W.; Chechavicius, B.; Dalmas, J.; Giovanelli, L.; Gothelid, M.; Karlsson, U. O.; Karpus, V.; Le Lay, G.; Sterzel, R.; Uhrig, E. *App. Surf. Sci.* **2003**, *9811*, 1-6.

(72)   Soda, K.; Nozawa, K.; Yanagida, Y.; Morita, K.; Mizutani, U.; Yokoyama, Y.; Note, R.; Inoue, A.; Ishii, H.; Tezuka, Y.; Shin, S. In *J. Electron Spectrosc. Relat. Phenom.*, 1998; Vol. 88-91, pp 415-418.

(73)   Terauchi, M.; Ueda, H.; Tanaka, M.; Tsai, A.-P.; Inoue, A.; Masumoto, T. In *Philos. Mag. Lett.*, 1998; Vol. 77, pp 351-357.

(74)   Wu, X.; Kycia, S. W.; Olson, C. G.; Benning, P. J.; Goldman, A. I.; Lynch, D. W. *Phys. Rev. Lett.* **1995**, *75*, 4540-4543.

(75)   Stadnik, Z. M.; Purdie, D.; Garnier, M.; Baer, Y.; Tsai, A. P.; Inoue, A.; Edagawa, K.; Takeuchi, S. *Phys. Rev. Lett.* **1996**, *77*, 1777-1780.

(76)   Stadnik, Z. M.; Purdie, D.; Garnier, M.; Baer, Y.; Tsai, A. P.; Inoue, A.; Edagawa, K.; Takeuchi, S.; Buschow, K. H. J. *Phys. Rev. B: Condens. Matter* **1997**, *55*, 10938-10951.

(77)   Naumovic, D.; Aebi, P.; Schlapbach, L.; Beeli, C.; Lograsso, T. A.; Delaney, D. W. *Phys. Rev. B* **1999**, *60*, R16330-R16333.

(78)   Stadnik, Z. M. *Mat. Sci. Eng. A* **2000**, *294-296*, 470-474.

(79)   Stadnik, Z. M.; Purdie, D.; Baer, Y.; Lograsso, T. A. *Phys. Rev. B* **2001**, *64*, 214202.

(80)   Shaub, T.; Delahaye, J.; Berger, C.; Guyot, H.; Belkhou, R.; Taleb-Ibrahimi, A.; Calvayrac, Y. *Eur. Phys. J. B* **2001**, *20*, 183-188.

(81)   Mori, M.; Matsuo, S.; Ishimasa, T.; Matsuura, T.; Kamiya, K.; Inokuchi, H.; Matsukawa, T. *J. Phys.: Condens. Matter* **1991**, *3*, 767-771.

ANALYSIS OF GAS PHASE CLUSTER FORMATION FROM LASER-VAPORIZED ICOSAHEDRAL Al-Pd-Mn

A paper published in *Materials Research Society: Symposium K Proceedings*

J.A. Barrow, E.F. Rexer, D.J. Sordelet, M.F. Besser, C.J. Jenks, S.J. Riley, and P.A. Thiel

Abstract

Laser vaporization of an icosahedral Al-Pd-Mn sample with detection by time-of-flight mass spectrometry is used to probe metal clusters made from the alloy. After sample vaporization, clusters form by gas aggregation and may contain several to hundreds of atoms. Multi-photon ionization/fragmentation of these clusters yields mass spectra showing many cluster sizes with enhanced intensity. Clusters are identified at masses near those of pseudo-Mackay and Bergman clusters; however, these clusters do not appear special relative to neighboring clusters. Results of this study and its relationship to the proposed cluster structures in quasicrystalline materials are discussed.

Introduction

Both pseudo-Mackay icosahedral (PMI) and Bergman type cluster models have been proposed as a basic motif for the quasicrystalline structure [1,2]. Many experiments have been done which provide support for cluster models. Quasicrystals are known to have low thermal and electrical conductivity. Measurements of these properties suggest a hierarchical localization. This would be consistent with electron localization inherent to a cluster-based

structure [3]. Studies of cleavage properties and plasticity have been interpreted within the context of stable clusters as structural sub-units [4,5]. In addition, neutron scattering studies were performed on the liquid melt of quasicrystal-forming alloys during the solidification process [6]. In these studies short-range icosahedral order was identified.

The cluster models proposed do begin to describe the bulk quasicrystalline structure; however, such models require clusters to be overlapping and interlaced. It is difficult to explain how these clusters could assemble in an energetically favorable way. A cluster jellium model has been proposed to describe the structure growth [3]. In this model the inflation is driven by attempts to obtain a stabilizing closed-shell electronic configuration for the clusters.

It may be useful to investigate quasicrystal structure with experiments designed to probe isolated metal clusters. An understanding of the fundamental interactions between atomic species in the clusters may provide insight regarding electronic and geometric stability. Additionally, studying the chemical properties of the clusters may aid our understanding of the metal surface since the clusters have a high percentage of surface atoms.

The method of laser vaporization is used in our study. After vaporizing the sample, the atoms condense into clusters, which are subsequently ionized and detected by time-of-flight mass spectrometry (TOF-MS). This technique has proven to be very successful for the study of both electronic and geometric structure of gas phase metal clusters. This method has been used in the past to investigate the electronic properties of small alkali clusters. The experimental evidence from that study was described in detail using a cluster jellium model [7]. Studies have also been done which probe cluster geometry. They show

that some systems adopt icosahedral symmetry [8]. Studying quasicrystals by this method

has the potential to provide important information regarding local electronic and geometric

structure.

In this paper we present the initial results of our study. If Bergman or PMI clusters

are inherently stable they may exist outside of the bulk quasicrystalline structure. Attempts

were made to detect gas phase Bergman or PMI clusters from laser vaporized icosahedral

Al-Pd-Mn.

Experimental

Clusters are made by laser vaporization of a quasicrystalline target rod in the cluster

source. This is coupled with the flow tube reactor where the vaporization plume is cooled,

and clusters form from the condensing atoms. Figure 1 shows a schematic of the cluster

source and flow tube reactor. The target rod is vaporized using a pulsed 2.33 eV frequency-

doubled Nd-YAG laser, delivering ~10 mJ/pulse. The laser enters the cluster source through

a quartz window and is focused on the target rod. The target rod is rotated and translated to

prevent the laser from burning a hole in its surface. Most evidence suggests that the

vaporization plume consists principally of neutral atoms, although small amounts of ions

and larger species may be present [9]. The target rod is positioned perpendicular to the 0.32

cm i.d. flow tube through which a helium carrier gas continuously flows at ~20 Torr.

Following each laser pulse, the resulting vaporization plume is very hot. The plume is

rapidly cooled by the helium flow as it is carried through the flow tube reactor. Calculations

show that the heat is essentially dissipated to the channel walls in a time that corresponds to

a travel distance of 0.5 cm down the flow tube; therefore, a concentration of supersaturated

metal atoms is quickly established and clusters begin to form [9]. Experiments show that cluster growth terminates by the time the plume has traveled ~4 cm down the flow tube reactor [10].

Figure 2 shows a schematic diagram of the instrument. The clusters leave the flow tube reactor through a 1 mm diameter nozzle and expand into stage I, which is held at 10^{-3} Torr. The clusters are formed into a molecular beam as they pass through a 2.5 mm diameter conical skimmer and enter stage II which acts as a differential pumping chamber held at 10^{-4} Torr. Finally, the cluster beam enters stage III where it is ionized and detected by time-of-flight mass spectrometry (TOF-MS).

Multi-photon ionization is done using a 4.03 eV XeCl laser at high fluence. The firing of the laser is delayed with respect to the vaporization laser to allow time for the packet of clusters to travel to stage III. The TOF-MS is oriented perpendicular to the cluster beam above the ionization region. Due to this configuration, electrostatic deflector plates are required to extract the ions. They are accelerated at 3 kV down a 1 m flight tube. For a given deflector plate setting a cluster mass range corresponding to 20μs of flight time is detected; therefore, the entire spectrum is put together by joining mass range sections recorded at the appropriate deflector settings. The TOF-MS is also equipped with a reflectron. This is a series of retardation plates at the end of the flight tube that directs the ions back toward a detector at the front of the flight tube. This allows the ions to travel a total of 2 m, and provides a longer flight time, energy focussing, and better resolution. The ions are detected with a microchannel plate detector. Data are acquired and signal averaged over thousands of laser shots to improve signal-to-noise ratios.

An important consideration in this experiment is the isotopic abundance of species in the target rod. Although Al and Mn have single isotopes, Pd contains five significant isotopes. When dealing with multi-atom clusters, the mass distribution of a cluster will significantly broaden with the number of Pd atoms in the cluster. This is demonstrated in figure 3. The upper spectrum shows a distribution of clusters containing up to three Pd atoms. The lower spectrum shows the same mass region using a target rod with isotopically enriched Pd. By comparison, the upper spectrum is considerably complicated by isotopic substructure. This broadening and isotopic substructure decreases the resolvable mass limit. Using an isotopically enriched target rod reduces these effects and significantly increases the resolvable mass limit.

The sample was prepared using palladium enriched with the ^{106}Pd isotope. First the Al and Mn were pre-alloyed by arc melting at the ratios of Al 80.3 (v)% and Mn 19.7 (v)%. The resulting Al-Mn ingot was alloyed with the ^{106}Pd isotope at the proportions ^{106}Pd 51.46 (w)% and Al-Mn 48.54 (w)%. The ingot acquired by this final alloying process was quasicrystalline, as verified by x-ray diffraction. The laser ablation apparatus required the sample to be rod shaped with specific dimensions. To do this, the quasicrystalline ingot was ground into a powder and loaded into a custom made crucible. The crucible was spray formed using yttria-stabilized zirconia. This was sealed under argon in a tantalum can and sintered at 775°C for 24 hours. The final sample was a 2.83 cm rod that was 3.11 mm in diameter.

Results

In this experiment, clusters were mass analyzed after a multi-photon ionization event. Multi-photon ionization provides a cluster with so much energy that it fragments into stable daughter ions. Experiments have shown that these ions do not decay further from the time they enter the TOF tube until they hit the detector. Clusters were detected with mass values matching PMI and Bergman clusters. This is shown in figure 4. The baseline becomes very noisy at these high masses because we are approaching the detection limit of the instrument. The peak broadening is due to random velocity vectors produced during fragmentation. At present, the clusters have not been characterized further. It is likely that these clusters are only mass coincident with PMI and Bergman clusters. They may not match the geometry and could even be of different composition. Nonetheless, if a particular cluster, such as PMI or Bergman, were especially stable, we would expect to see a peak of much greater intensity relative to neighboring peaks. These spectra show no indication of exceptional stability. Instead, many stable clusters have been produced in relatively similar quantities. This may indicate a pattern of stability over a large range of cluster sizes.

Conclusions

We have presented the initial results of our investigation of gas phase clusters formed by laser vaporization of icosahedral Al-Pd-Mn. Although clusters appear at mass values coincident with PMI and Bergman clusters, they are not especially stable relative to the surrounding masses. Further studies are required to conclusively determine cluster geometries and compositions.

Acknowledgments

References

1. V. Elser, Philos. Mag. B **73** (4), 641-56 (1996).

2. C. Janot and M. de Boissieu, Phys. Rev. Lett. **72** (11), 1674-7 (1994).

3. C. Janot, Phys. Rev. B: Condens. Matter **53** (1), 181-91 (1996).

4. Ph. Ebert, M. Feuerbacher, N. Tamura et al., Phys. Rev. Lett. **77** (18), 3827-3830 (1996).

5. M. Feuerbacher, C. Metzmacher, M. Wollgarten et al., Mat. Sci. Eng. A. **233**, 103-110 (1997).

6. M. Maret, J. M. Dubois, and P. Chieux, J. Non-Cryst. Solids **156-158** (Pt. 2), 918-22 (1993).

7. W. de Heer and et al., Solid State Phys. **40** (93) (1987).

8. E.K. Parks and et al., J. Chem. Phys. **94** (12) (1991).

9. E.K. Parks and S.J. Riley, "Experimental Studies of the Chemistry of Metal Clusters," in *The Chemical Physics of Atomic and Molecular Clusters*, edited by G. Scoles (North-Holland, Amsterdam, 1990), pp. 761.

10. E.K. Parks, B.H. Weiller, P.S. Bechthold et al., J. Chem. Phys. **88**, 1622-1632 (1988).

Figure Captions

Figure 1. Schematic diagram of vaporization source and flow tube reactor.

Figure 2. Schematic diagram of instrument.

Figure 3. Time-of-flight mass spectra of clusters made from a natural Al-Pd-Mn target (upper), and an isotopically enriched Al-^{106}Pd-Mn target (lower).

Figure 4. Mass spectra of multi-photon ionized clusters. Labels indicate where we would expect to find PMI and Bergman clusters. Masses for PMI clusters were calculated based on compositions described by Janot [5].
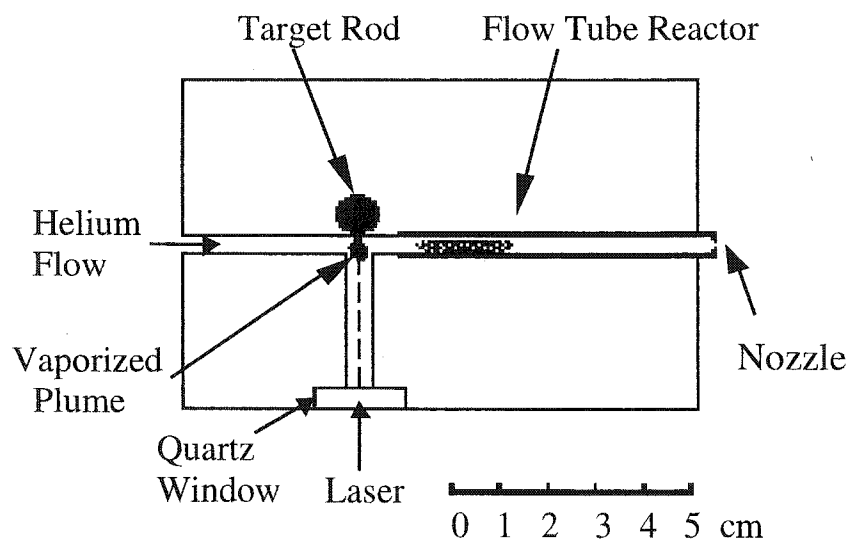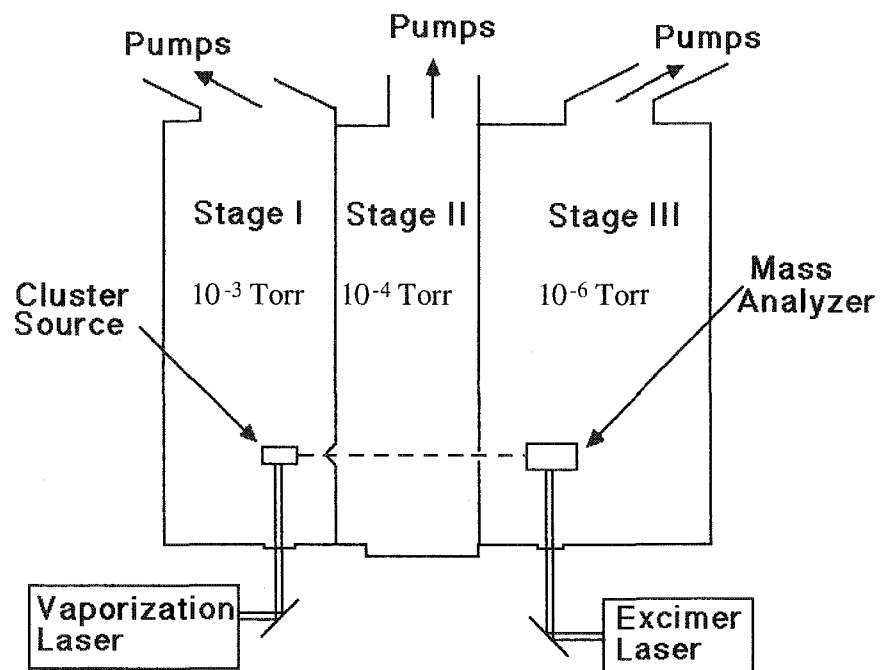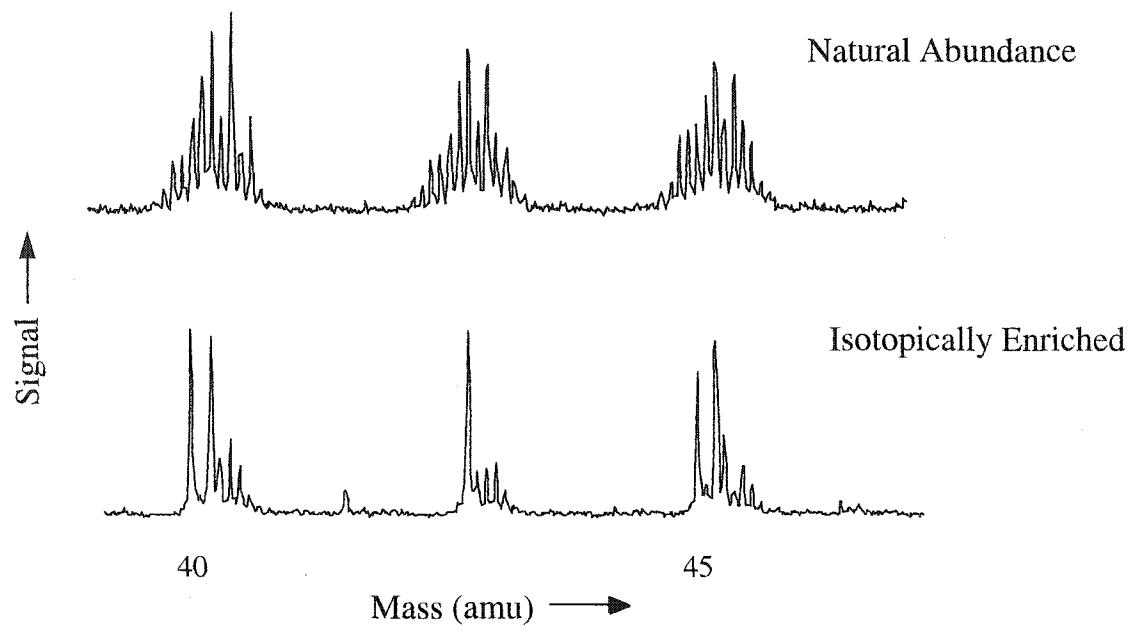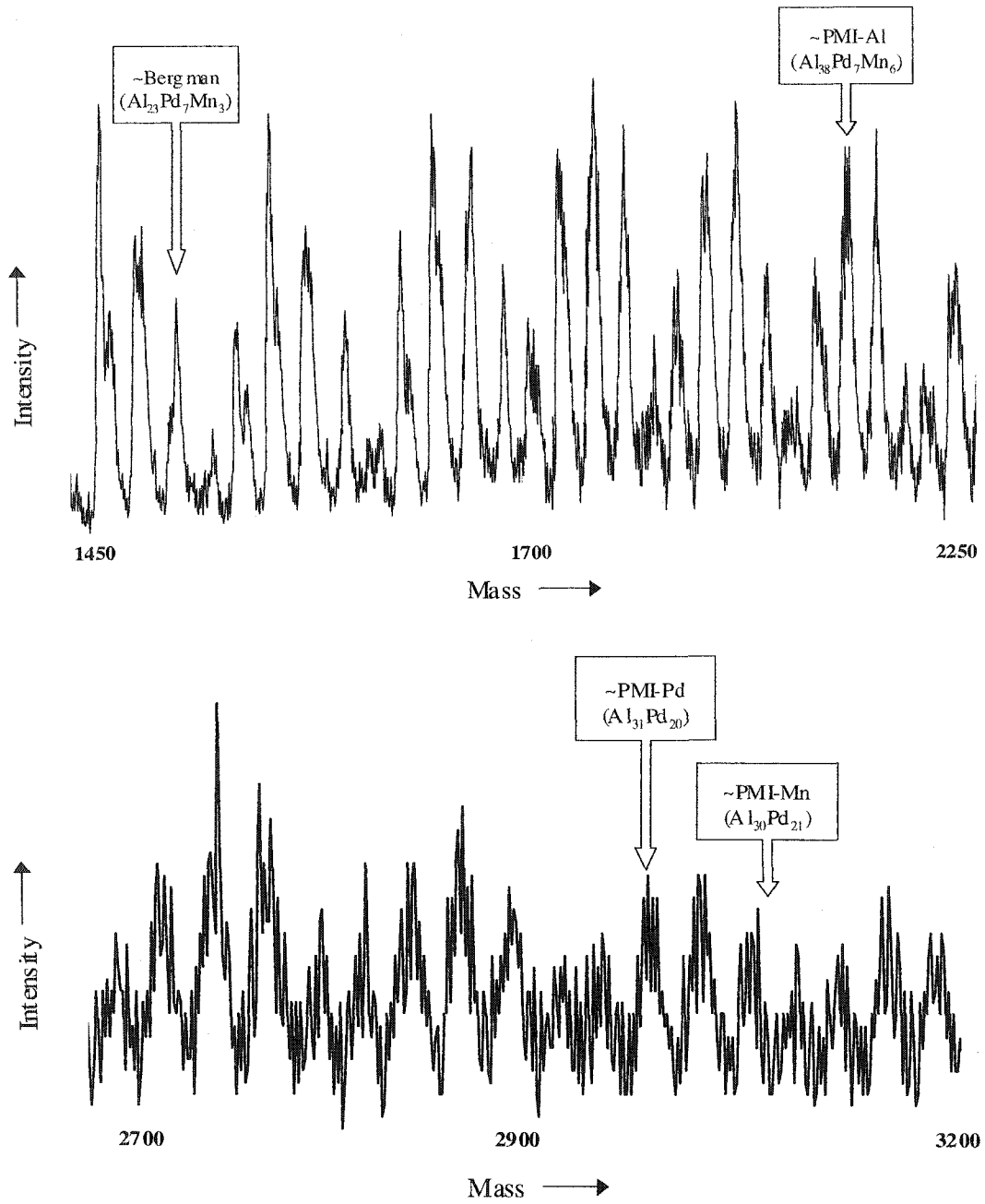
Figure 1

Figure 2

Natural Abundance

Isotopically Enriched

Signal →

40

45

Mass (amu) →

Figure 3

Figure 4

ANALYSIS OF GAS-PHASE CLUSTERS MADE FROM LASER-VAPORIZED ICOSAHEDRAL Al-Pd-Mn

J. A. Barrow, D. J. Sordelet, M. F. Besser, C. J. Jenks, P. A. Thiel,
E. F. Rexer and S. J. Riley

Abstract

An icosahedral Al-Pd-Mn quasicrystal sample is laser vaporized to form metal clusters by gas aggregation. The clusters are subsequently laser ionized and mass analyzed in a time-of-flight mass spectrometer. The mass spectra show cluster compositions which are qualitatively similar to that of the sample. This is consistent with a kinetically controlled cluster growth process. Cluster thermodynamic stability is probed by multi-photon ionization/fragmentation, which induces primarily Al and Mn loss. The resulting spectra are composed of a series of Pd-rich Al-Pd clusters. The average cluster composition is 60 (± 1)% Pd. This composition is close to a known eutectic in the Al-Pd system. When manganese is seen on these clusters, it is always in units of Mn_3. These results are discussed in terms of relative binding strengths in the Al-Pd-Mn alloy system.

Introduction

In 1982 Shechtman et al., characterized an aluminum-rich intermetallic compound with a rotational symmetry forbidden by classical crystallography (1). Since then, it has

been shown that such forbidden symmetries are the result of well-ordered but aperiodic atomic structures. This new form of matter is neither crystalline nor amorphous, but is quasiperiodic and has been termed quasicrystalline. In comparison with crystalline intermetallics, quasicrystals exhibit peculiar physical and electronic properties (2). For example, quasicrystals are very hard and brittle, and they have low surface energy and low electrical and thermal conductivities. The relationship between quasiperiodicity and these unique properties has not been firmly established, but there have been extensive research efforts aimed at understanding this relationship.

Theoretical models have been proposed using either pseudo-Mackay icosahedral or Bergman type clusters as a basic motif for the quasicrystalline structure (3, 4, 5). The Bergman type cluster model requires one cluster with the composition $Al_{23}Pd_7Mn_3$ (5). The pseudo-Mackay cluster model uses three different types of basic clusters: $Al_{38}Pd_7Mn_6$, $Al_{31}Pd_{20}$, and $Al_{30}Pd_{21}$ (3, 4). There is experimental evidence to support the idea of cluster-based structures. Measurements of the electrical and thermal properties of quasicrystals suggest a hierarchical localization. This is consistent with the electron localization inherent to a cluster (4). In addition, the cleavage properties and plasticity of quasicrystals have been interpreted in the context of stable clusters acting as structural sub-units (6, 7).

It is possible to describe the bulk structure of quasicrystalline materials with cluster models, but the models require complex rules for overlapping and interlacing the clusters (4), and it is difficult to explain how clusters would actually assemble during growth to form a quasicrystalline structure. With this in mind, we felt that a study of isolated clusters of quasicrystalline material might probe the fundamental interactions between the atomic

species in quasicrystals and improve our understanding of their local electronic properties and geometric structure. As a basis for such a study, we have applied a proven technique for investigating the properties of gas-phase metal clusters – laser vaporization coupled with time-of-flight mass spectrometry (TOF-MS) (8, 9). In the present study an icosahedral $Al_{70}Pd_{22}Mn_8$ quasicrystalline target is laser vaporized in a conventional cluster source and the composition and stability of the resulting clusters is probed via laser ionization TOF-MS. Although studies of pulsed-laser deposition of quasicrystalline materials have been reported (10), there have not been to our knowledge any cluster beam studies of the Al-Pd-Mn quasicrystal system or of any of the possible two-component systems Al-Pd, Al-Mn, or Mn-Pd.

Experimental

The experimental apparatus has been described in detail elsewhere (11, 12). To summarize briefly, gas-phase clusters are produced by laser vaporization in a source coupled to a flow tube reactor (FTR). The Al-Pd-Mn target rod is vaporized using a frequency doubled Nd-YAG laser. Helium gas continuously flows through the source and carries the vaporization plume through the FTR. This results in rapid cooling of the plume and the condensation of atoms into clusters. The clusters then pass out of a nozzle at the end of the FTR and through a conical skimmer to form a molecular beam. The beam then enters a separate chamber where the clusters are laser ionized and the ions extracted into the time-of-flight mass spectrometer. The mass spectrometer can be operated in two modes: direct (linear) and reflectron. In the linear mode, an ion's flight time is determined solely by its

velocity, i.e., its initial mass and the extraction energy. Any metastable cluster post-source

decay (PSD, the breakup of cluster ions in the drift region) will not be evident in the mass

spectrum, since the daughter ions will have the same velocity as their parents. In the

reflectron mode (which provides superior resolution), ion flight time also depends on

translational energy, so daughter ions resulting from metastable PSD, having energies

different from their parents, will appear as additional peaks in the mass spectrum.

Metastable cluster decay can thus be identified by comparing linear TOF-MS data to

reflectron TOF-MS data.

Clusters are ionized with an excimer laser under conditions of either single-photon or

multi-photon absorption. For single-photon ionization (SPI) experiments, a low fluence (1.3

x 10^{16} photons/cm^2) ArF excimer laser (193 nm, 6.42 eV photon energy) is used. Under

these conditions, it is assumed that the distribution of cluster ion species directly reflects the

distribution of neutral clusters that exit the source. The validity of this assumption has been

tested over many years of cluster research, and has been shown to be good, provided the

photon energy is not substantially larger than the cluster ionization potential (IP). In general,

SPI mass spectra have very good resolution, and they are used to make mass peak

assignments. But even with very high resolution, definitive mass assignments rapidly

become impossible with increasing cluster size because of the five significant Pd isotopes

(Al and Mn have only one isotope each). To help solve this problem, a target is made from

isotopically enriched ^{106}Pd, by sintering quasicrystalline Al-^{106}Pd-Mn powder. A detailed

description of the sample fabrication procedure has been reported (11). Figure 1 shows mass

spectra illustrating the simplification provided by the isotopic enrichment.

Even with the ^{106}Pd-enriched target, isobaric interferences occur. For example, ^{27}Al$_8$^{106}Pd and ^{106}Pd$_2$^{55}Mn$_2$ have the same nominal mass. Modeling the SPI spectra helps compensate for these interferences. First, "best guess" peak assignments are made for the spectrum obtained with the isotopically enriched target. Using these assignments and the known isotopic distribution of natural Pd, a natural abundance mass spectrum is simulated. The simulated spectrum is then compared with an experimental natural abundance mass spectrum. This process is iterated until the two spectra agree. The peak assignments that produce the best fit are taken as the correct ones.

In multi-photon ionization (MPI) experiments the clusters are ionized with a high-fluence (1.3 x 10^{17} photons/cm^2) excimer laser whose single-photon energy can be below the cluster IPs. In the present experiments both the ArF and a XeCl (308 nm, 4.03 eV photon energy) laser were used for MPI. The multi-photon absorption leads to extensive cluster fragmentation, so that the prominent peaks in an MPI spectrum are due to particularly stable fragment (daughter) species. This provides a means of identifying thermodynamically stable cluster species. This is essential for a detailed analysis of the binding patterns in the Al-Pd-Mn system. Some peak broadening is seen in MPI mass spectra due to the random velocity vectors imparted to the daughters during the fragmentation process.

Results and Interpretation

The SPI spectrum shows a broad, uniform distribution of mass peaks periodically grouped into envelopes separated by ~27 amu. This is representative of the similar mass multiples of Al, Mn, and Pd. A small portion of this distribution is shown in the top

spectrum of Fig. 2. There is no observable modulation of the envelope intensity in the

vicinity of the masses of Bergman or pseudo-Mackay icosahedral clusters that would

indicate any special stability of these species. This is not surprising, since clusters that are

made in a laser vaporization/inert gas condensation source grow via a process that is strongly

kinetically controlled. The amount of a given cluster produced does not depend on that

cluster's stability, but only on the statistical probability that sufficient (irreversible) cluster-

atom collisions occur to make that cluster (13). Traditional "magic numbers" do not appear

in mass spectra of clusters made in this manner. Instead, other probes of cluster

thermodynamic stability must be used (13-16). We applied three of these probes (17):

heating the clusters to 1000 °C, to look for thermal fragmentation, photo-ionizing them

nearer to their ionization thresholds to identify clusters with unusually high IPs, and reacting

them with oxygen, another probe of electronic stability. In no case was there any evidence

for special behavior in the vicinity of the Bergman or pseudo-Mackay icosahedral clusters.

In fact, the initial broad, uniform distribution of mass peak intensities was generally

unchanged when these probes were applied.

The situation is dramatically different when the clusters are multi-photon ionized. A

very strong modulation of the overall intensity distribution occurs, as can be seen in the

bottom spectrum of Fig. 2. As discussed above, this modulation is due to extensive cluster

fragmentation, and the prominent peaks represent stable daughter species. This signal

modulation pattern extends to the largest clusters studied, but once again there is no obvious

change in the pattern in the vicinity of Bergman and pseudo-Mackay clusters. It should be

noted that, even though the spectral peaks are too broad to be resolved, it is still possible to observe an increase in signal intensity near the mass of a particular species.

As mentioned above, MPI causes peak broadening in the spectra, complicating mass assignments. This is resolved by recording the spectrum at an intermediate fluence, as is shown in the middle spectrum of Fig. 2. Here the stable daughter peaks have begun to grow in intensity and have broadened somewhat, but not so much that unambiguous comparison with the top spectrum cannot be made. Also, since the laser fluence is not yet high enough to multi-photon ionize all of the clusters, SPI clusters are still present in the spectrum. By aligning the three spectra, it is possible to determine which SPI peaks are coincident with the MPI peaks. It is assumed that coincident peaks represent clusters of the same composition. In this manner, conclusive composition assignments can be made for peaks in the lower mass region of the MPI spectrum. This region, along with some of the assignments, is shown in Fig. 3.

This analysis shows that the principal peaks in the MPI spectrum are due to Pd-rich, Al_mPd_n clusters. For most values of n, there is a distribution of three m values. This is shown in Fig. 4, where the data are plotted as m vs. n, i.e., number of Al atoms in the cluster vs. number of Pd atoms in the cluster. Each data point represents a specific Al_mPd_n cluster. Average cluster composition is determined by linear regression, yielding a slope of 0.67 with an R^2 value of 0.91. This corresponds to an average Pd concentration of 60 ($\pm$1)%. This composition is coincident with a known Al-Pd eutectic at 61.3% (18).

Manganese begins to appear consistently on clusters sizes of Al_mPd_6 and greater, but only as Mn_3. Manganese addition is not observed with either more or less than three Mn atoms. This suggests that the stable Al_mPd_n clusters may be decorated with a Mn trimer.

It is difficult to determine relative $Al_mPd_nMn_3$ and Al_mPd_n peak intensities due to MPI broadening and mass overlap. By fitting the measured peaks with Lorentzian profiles, it is possible to deconvolute them and recover the relative peak intensity distributions. These are shown in Fig. 5. Each vertical pair of curves represents a single value of n, i.e., they represent clusters with the same number of Pd atoms. Each curve spans a series of m values, i.e., it spans clusters over a range of number of Al atoms. The top and bottom curves compare clusters with and without Mn, respectively. Comparing each vertical pair of curves, it can be seen that the intensity profiles derived from Al_mPd_n peaks match those derived from $Al_mPd_nMn_3$ peaks. This indicates that the Mn_3 acts as a chemical spectator that can attach or detach from the Al_mPd_n cluster without perturbing the Al-Pd stoichiometry.

This spectator role for manganese is reinforced by a comparison of MPI spectra of clusters made from the Al-Pd-Mn target with those of Al-Pd clusters made in a general purpose alloy cluster source (19). In the latter source, two YAG laser beams are used to vaporize metal from a target rod and a wire suspended near the rod. By adjusting the relative power and timing of the laser pulses, the relative amounts of the two metals in the vaporized plume can be varied. Figure 6 shows, in the upper panel, a portion of the MPI spectrum recorded with an Al rod and a Pd wire as the source. Further, these data are obtained under conditions that produce SPI spectra qualitatively similar to those from the quasicrystal target (i.e., the alloy clusters are Al rich and have comparable relative amounts of Al and Pd in

them). The lower panel in Fig. 6 shows an MPI spectrum recorded under similar conditions for the quasicrystal target. The virtually identical appearance of the two spectra supports the argument that the presence of Mn in the initial cluster has little if any effect on the compositions of the ultimately stable Al_mPd_n species.

A comparison of reflectron TOF MPI spectra with linear TOF MPI spectra shows no evidence for metastable decay of clusters from the quasicrystalline target rod. This is somewhat surprising, since the primary process occurring in the Al-Pd clusters under MPI conditions is Al loss, while multi-photon ionization of pure aluminum clusters also results in Al loss and shows substantial metastable PSD (20). The difference is in the range of fragment-cluster binding energies in the two systems. In order for metastable PSD to occur, there must be an evaporative event that occurs during the ion flight time in the reflectron. In pure Al clusters, binding energies are relatively independent of cluster size, and the time to decay will depend largely on the amount of excess energy in the activated cluster. Each time a decay event occurs, this energy is reduced by at least the amount of the binding energy, so there will be a nearly continuous distribution of excess energies and thus decay times. One of these times will fall within the window leading to metastable PSD. For the Al-Pd clusters, on the other hand, there is a sudden increase in cluster-Al binding energy when the cluster reaches the stable Al_mPd_n composition. Apparently, the aluminum (as well as the manganese) loss from the initial clusters is so rapid that these processes are finished before the ions are extracted. Subsequent Al loss, if any, does not occur within the flight time, so no metastable PSD peaks appear in the MPI mass spectra.

Discussion

The two types of laser ionization conditions used here, SPI and MPI, provide information about two processes: formation, and decay, of the clusters. It is reasonable, and consistent with previous work, to expect that the cluster formation is dominated by the kinetics of the cluster-atom collisions; whereas, decay (as probed with MPI) provides information about the relative thermodynamic stabilities of the decay products (21).

The kinetic formation of Al-rich clusters in the FTR is consistent with the Al-rich plume composition expected when vaporizing the quasicrystalline target. Beyond this, the SPI data do not provide fundamental insight into the cluster chemistry. They are, however, essential in identifying the MPI spectral peaks correctly, as illustrated in Fig. 2. During the multi-photon ionization process the clusters quickly lose the Mn and then begin to lose Al until a stable Pd core is formed. This idea is consistent with the relative vapor pressures of the three metals: Mn > Al > Pd.

The average composition of the Al-Pd clusters is 60 ($\pm$1)% Pd. This may be related to the existence of a eutectic in the Al-Pd phase diagram at 61.3% Pd (18). Although these are gas-phase clusters, it is not unreasonable to think of them as liquid droplets from which the aluminum species "boil off", allowing the cluster to approach the eutectic by following the bulk liquidus. While this idea is intriguing, it clearly requires further research before conclusions may be drawn.

It is unclear whether the Al plays a role in stabilizing the core, or simply decorates a stable Pd core. The similarity of the intensity profiles for Al_mPd_n clusters and $Al_mPd_nMn_3$ clusters (Fig. 5) suggests that Mn addition occurs after the Al_mPd_n has formed. Since the

Mn_3 does not affect the Al-Pd stoichiometry, it is probable that Mn acts only as a chemical spectator and has no role in core stabilization.

The fact that Mn is only observed in groups of 3 per cluster is interesting. It suggests that the Mn atoms may be linked together to form a trimer. Mn decoration does not occur regularly until the core has reached the critical size of Al_mPd_6. It may be that Mn_3 requires a specific binding site on the Al-Pd cluster. This site may not be consistently available until the core has reached the critical size. It is puzzling that we do not observe any Al-Pd clusters with multiples of three Mn. We would expect to find clusters with Mn_6 or Mn_9 decoration, but this is not observed.

Returning to the initial motivation for this study, the clusters observed in these experiments are different than those clusters expected from the cluster-based structure of the parent quasicrystal, in two ways. First, a more intense signal corresponding to the Bergman and MacKay-type clusters is not observed under these experimental conditions; hence, there is no evidence that they have special stability, at least not as isolated units. Second, the Mn atoms do not affect the stability of the Al-Pd clusters under MPI conditions, whereas in the bulk quasicrystalline material Mn atoms are integral components. It is possible that for different types of gas-phase cluster experiments, perhaps those more conducive to equilibration of large, multi-component structures, Bergman or MacKay-type clusters could be observed; however, the present data fails to indicate a special stability for isolated clusters of the type that exist in quasicrystals. It is also possible that such clusters only have special stability in the context of the bulk matrix, and may not exist as isolated units.

Acknowledgments

References

(1)   Shechtman, D.; Blech, I.; Gratias, D.; Cahn, J. W. *Phys. Rev. Lett.* **1984,** *53,* 1951-3.

(2)   Jenks, C. J.; Thiel, P. A. *Langmuir* **1998,** *14,* 1392-7.

(3)   Janot, C.; de Boissieu, M. *Phys. Rev. Lett.* **1994,** *72,* 1674-7.

(4)   Janot, C. *Phys. Rev. B: Condens. Matter* **1996,** *53,* 181-91.

(5)   Elser, V. *Philos. Mag. B* **1996,** *73,* 641-56.

(6)   Ebert, P.; Feuerbacher, M.; Tamura, N.; Wollgarten, M.; Urban, K. *Phys. Rev. Lett.* **1996,** *77,* 3827-30.

(7)   Feuerbacher, M.; Metzmacher, C.; Wollgarten, M.; Urban, K.; Baufeld, B.; Bartsch, M.; Messerschmidt, U. *Mat. Sci. Eng. A.* **1997,** *233,* 103-10.

(8)   De Heer, W. A.; Knight, W. D.; Chou, M. Y.; Cohen, M. L. *Solid State Phys.* **1987,** *40,* 93-181.

(9)   Klots, T. D.; Winter, B. J.; Parks, E. K.; Riley, S. J. *J. Chem. Phys.* **1991,** *94,* 8919-30.

(10)   Teghil, R.; D'Alessio, L.; Simone, M. A.; Zaccagnino, M.; Ferro, D.; Sordelet, D.J. *App. Surf. Sci.* **2000,** *168 (1-4),* 267-269.

(11)   Barrow, J. A.; Rexer, E. F.; Sordelet, D. J.; Besser, M. F.; Jenks, C. J.; Riley, S. J.;

Thiel, P. A., *Proceedings of the Materials Research Society (Symposium K),* edited

by E. Belin-Ferré, P.A. Thiel, A-P. Tsai, K. Urban (Material Research Society,

2000), pp. K5.4.1-K5.4.5.

(12)   Parks, E. K.; Riley, S. J. In *The Chemical Physics of Atomic and Molecular Clusters*;

Scoles, G., Ed.: North-Holland, Amsterdam, 1990, pp 761.

(13)   Riley, S. J. *J. Non-Cryst. Solids* **1996,** *205-207,* 781-7.

(14)   Parks, E. K.; Weiller, B. H.; Bechthold, P. S.; Hoffman, W. F.; Nieman, G. C.; Pobo,

L. G.; Riley, S. J. *J. Chem. Phys.* **1988,** *88,* 1622-32.

(15)   Zhu, L.; Ho, J.; Parks, E. K.; Riley, S. J. *J. Chem. Phys.* **1993,** *98,* 2798-2804.

(16)   Winter, B. J.; Parks, E. K.; Riley, S. J. *J. Chem. Phys* **1991,** *94,* 8618-21.

(17)   Riley, S. J.; Kerns, K. P.; Jenks, C. J.; Sordelet, D.J.; Thiel, P.A., "The Search for

Magic Number Clusters in Laser-Vaporized Al-Pd-Mn," Book of Abstracts, 7th

International Conference on Quasicrytals, Stuttgart, Germany, September 20-24,

1999.

(18)   *Bulletin of Alloy Phase Diagrams,* Metals Park, Ohio: American Society for Metals,

7(4), Aug. 1986.

(19)   Rexer, E. F.; Jellinek, J.; Krissinel, E. B.; Parks, E. K.; Riley, S. J. *J. Chem. Phys.*

2002, *117,* 82-94.

(20)   Rexer, E. F.; Parks, E. K.; Riley, S. J. *unpublished results.*

(21)   Martin, T. P.; Bjornholm, S.; Borggren, J.; Bréchignac, C.; Cahuzac, Ph.; Hansen,

K.; Pederson, J. Chem. Phys. Lett. **1991,** *186,* 53-7.

Figure Captions

Figure 1. Portions of time-of-flight mass spectra recorded for a natural Al-Pd-Mn target (upper), and an isotopically enriched Al-^{106}Pd-Mn target (lower).

Figure 2. Top panel: portion of the mass spectrum recorded with low ionizing laser fluence (1.3 x 10^{16} photons/cm^2) and the isotopically enriched target. Middle panel: same spectrum recorded with intermediate laser fluence (3.3 x 10^{16} photons/cm^2). Lower panel: the spectrum recorded with high laser fluence (1.3 x 10^{17} photons/cm^2).

Figure 3. Representative portion of the MPI mass spectrum from the isotopically enriched target. Ionization is with a focussed XeCl laser. Principal peaks showing the progression of Al$_m$Pd$_n$ species, as well as some of the Mn$_3$-containing peaks, are annotated.

Figure 4. Plot of the number of Al atoms, m, vs. the number of Pd atoms, n, in MPI-produced clusters. The straight line is a linear regression with a slope of 0.67 (R^2 = 0.91) corresponding to an average cluster composition of 60% Pd.

Figure 5. Intensity distributions of representative Al$_m$Pd$_n$ species derived from peaks without (upper panel) and with (lower panel) Mn$_3$ attached.

Figure 6. Upper panel: portion of the MPI spectrum recorded with an alloy cluster source using a (natural) Pd wire and an Al target rod. Lower panel: same spectrum recorded with the (natural) quasicrystal target. Ionization in both cases is with a focussed ArF laser. The slight differences in relative peak intensities reflects a slightly higher laser fluence for the lower spectrum.
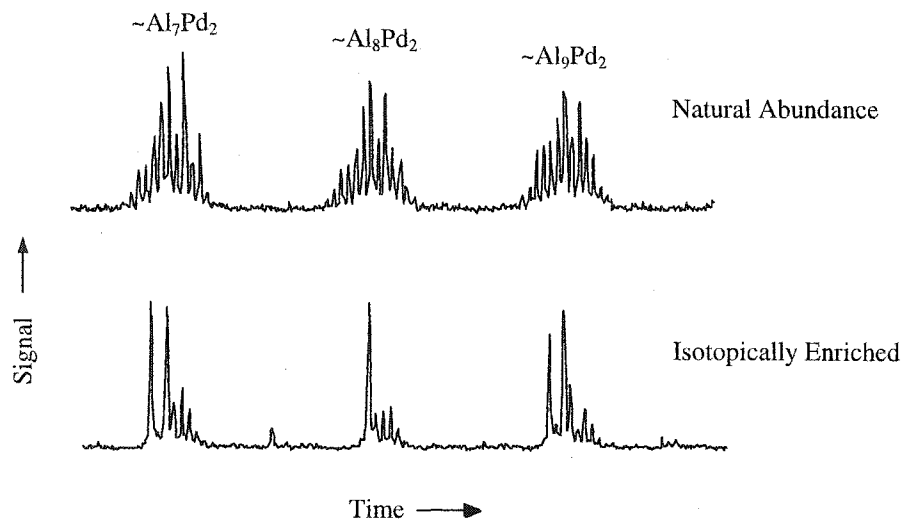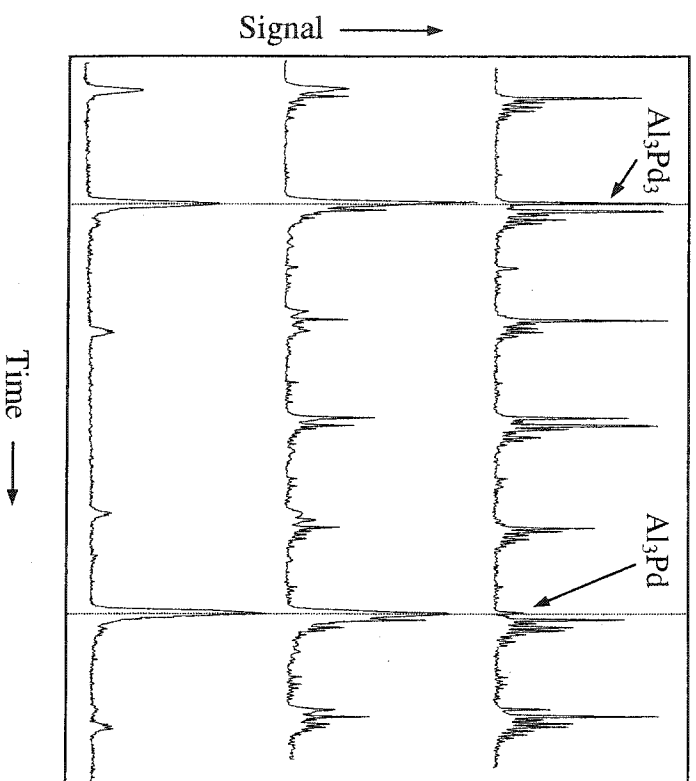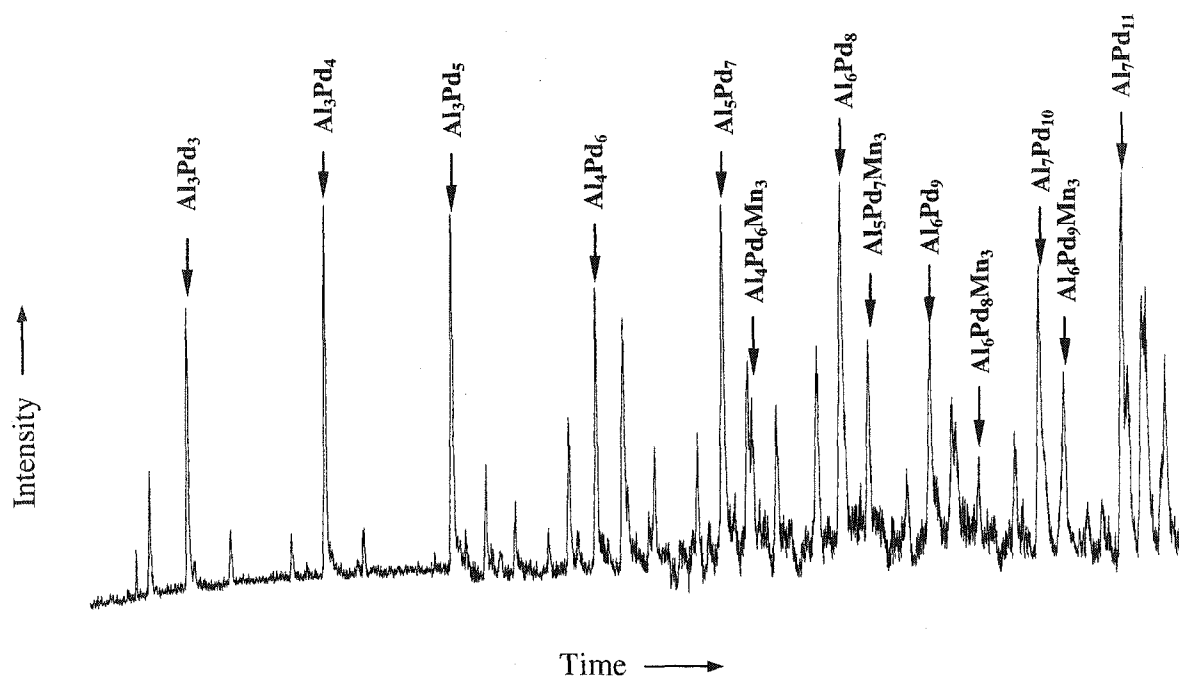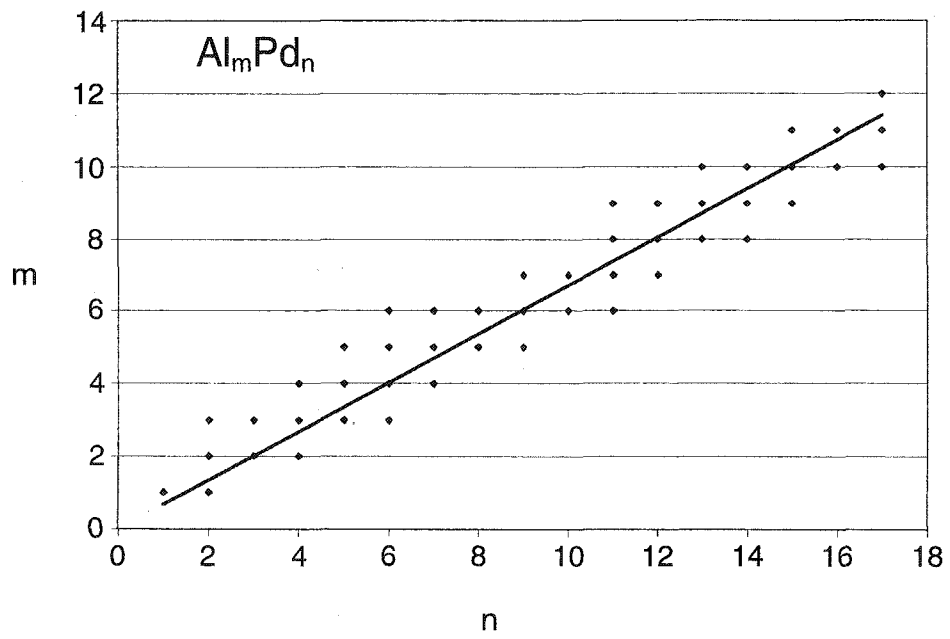
Figure 1

Figure 2

40

Figure 3

Figure 4
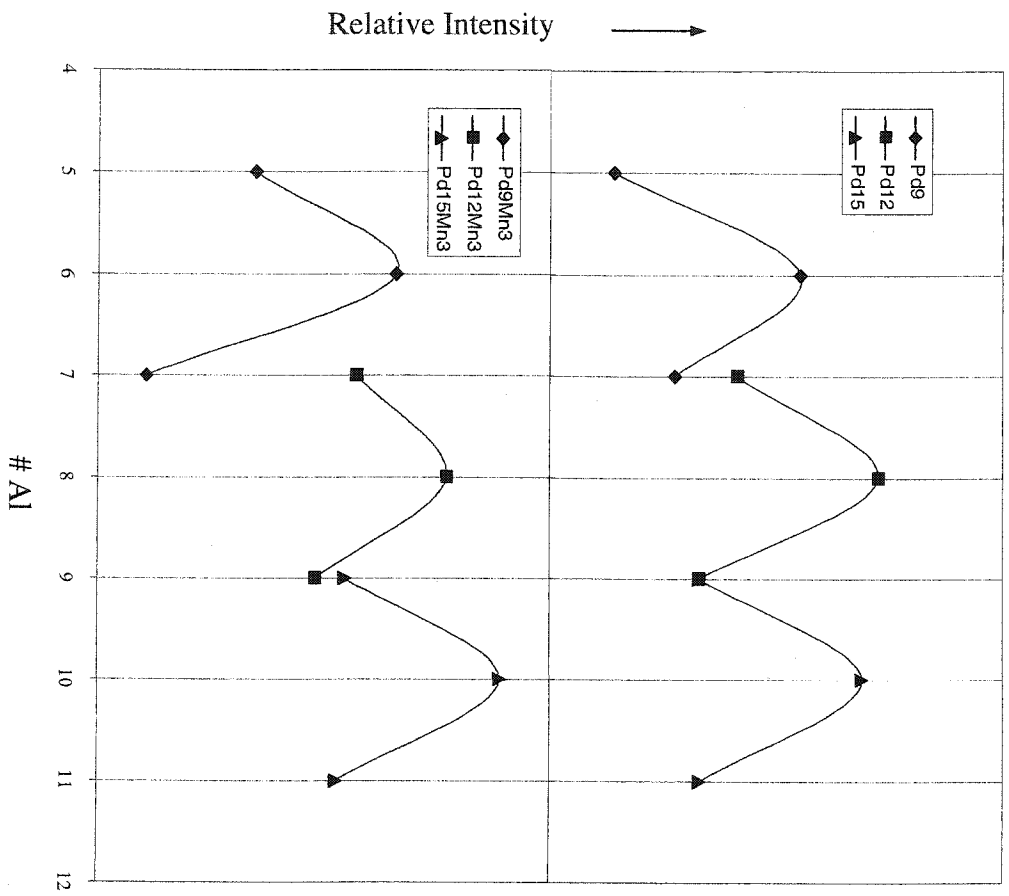
Figure 5

43

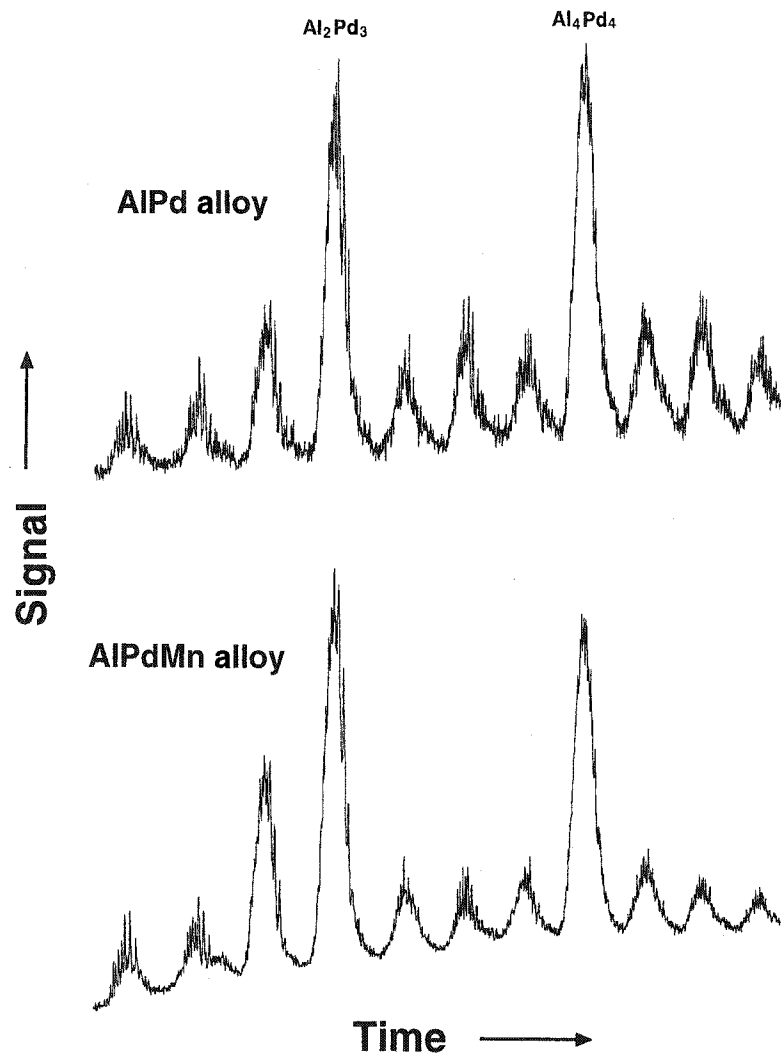Figure 6

HIGH-TEMPERATURE THERMAL TRANSPORT PROPERTIES OF A SINGLE GRAIN DECAGONAL Al$_{74}$Ni$_{10}$Co$_{16}$ QUASICRYSTAL

J. A. Barrow, B. A. Cook, P. C. Canfield, and D. J. Sordelet

Abstract

Thermal transport properties have been determined for a decagonal Al$_{74}$Ni$_{10}$Co$_{16}$ quasicrystal in the temperature range 373K-873K. Differential scanning calorimetry and a laser flash method were employed in the determination of heat capacity and thermal diffusivity, respectively. Thermal conductivity was determined from the product of diffusivity, heat capacity, and density. A high degree of anisotropy was observed between the aperiodic and periodic axes. The anisotropic heat flow is described using the thermal ellipsoid model. The model was applied to a surface oriented 45° to the major axes and substantiated from bulk measurements obtained from a sample cut along this orientation. Within this temperature range, the thermal transport of this 2 dimensional quasicrystal may be described in a manner similar to anisotropic metallic single crystals.

Introduction

Since the initial discovery of quasicrystals, several stable quasiperiodic intermetallics have been found [1, 2]. Of particular interest are the stable decagonal quasicrystals, which consist of a periodic stacking of ten-fold quasiperiodic planes. This unique structure allows one to comparatively study quasicrystalline and crystalline properties along different

directions within the same sample. Studies of this type may provide important clues toward understanding the unusual properties of quasiperiodic materials.

It is well known that thermal transport in quasicrystals is anomalously low compared with intermetallic crystalline phases. These properties are often attributed to electron localization and the existence of a pseudo-gap in the electronic density of states at the Fermi level [2, 3]. Since decagonal quasicrystals are only quasicrystalline in 2D, it is not surprising that significant anisotropic transport properties have been reported [4-7]; however, to date, studies of the Al-Ni-Co decagonal system have been limited to temperatures below 300K. A study of the high temperature thermal transport properties complements existing low-temperature results and provides useful information toward practical applications of quasicrystals. In this paper we report the first high-temperature thermal diffusivity and heat capacity data for decagonal (d)-$Al_{74}Ni_{10}Co_{16}$ over the temperature range of 373K-873K. Thermal conductivity was calculated as a function of temperature over this range.

Experimental

A large (0.8 cm^3) single-grain decagonal $Al_{74}Ni_{10}Co_{16}$ quasicrystal was grown using a flux growth technique [8]. The sample possessed a rod-like morphology, with the c-axis parallel to the length of the rod and 10-side growth facets oriented normal to the c-axis, reflecting the decagonal symmetry of the quasicrystal structure. Samples with parallel faces of approximately 10 mm in diameter and 1mm in thickness were cut by electro-discharge machining and used for diffusivity measurements. The aperiodic and periodic sample surfaces are perpendicular to the periodic c-axis and the aperiodic radial axes, respectively.

Experiments were also performed on a sample surface oriented 45° from the c-axis, i.e. the

sample's normal axis is half way between the periodic axis and the aperiodic plane. Figure

1 illustrates how the samples were cut from the single grain ingot. The samples will

hereafter be referred to as periodic, aperiodic, and 45°, as indicated in Figure 1. Pieces of

the remaining single-grain adjacent to the harvested samples were cut and ground into

powder for X-ray analysis and heat capacity measurements. The structural quality of the

sample used in this study is comparable, based on powder X-ray diffraction data, to the

sample having the same nominal composition described by Fisher *et al.* [8]

Diffusivity measurements on these samples were made using the laser flash method.

Samples were coated with a thin layer of graphite (10 to 30 μm) to reduce the reflection of

background radiation. A monochromatic laser (λ=628 nm) is used to irradiate the front

surface of the sample with a 1 ms pulse. The temperature profile of the opposite surface is

monitored using a liquid nitrogen-cooled InSb infrared detector. The detector output is

transferred to a digital storage oscilloscope. Calibration of the scope enables quantitative

determination of the sample's temperature as a function of time. Irradiation of the aperiodic

sample and periodic sample provides bulk thermal diffusivity data along an aperiodic radial

axis and the periodic c-axis, respectively. Thermal diffusivity, α, can be calculated from the

temperature rise profile using:

$$\alpha = 1.38 \, L^2 / \pi^2 \, t_{1/2} \qquad (1)$$

where L is the thickness of the sample and $t_{1/2}$ is the time required for the heat pulse to reach

one-half the maximum value.

The thermal conductivity, κ, is related to diffusivity, α, by the following equation:

$$\kappa = \alpha\rho C_p \qquad (2)$$

where, C_p is the molar heat capacity (J mol^{-1} K^{-1}), and ρ is density (g cm^{-3}).

Density measurements were made at room temperature using Archimedes' technique. Measurements of heat capacity were made using a Perkin Elmer Pyris 7 Differential Scanning Calorimetry (DSC). The sample was ground into a powder and placed in a platinum crucible. An empty platinum crucible was used as a reference. Heating and cooling rates were 5K / min.

Results and discussion

Results of the diffusivity characterization for the three orientations are shown in Figure 2. Thermal diffusivity through the aperiodic sample is comparable to data previously reported for icosahedral quasicrystals [3, 9]. A clear anisotropy is seen between the samples. Measurements on the periodic sample show thermal diffusivities nearly an order of magnitude larger than the corresponding aperiodic specimen over the observed temperature range.

Figure 3 shows the molar heat capacity as determined by DSC. At lower temperatures this data appears to be a continuation of the heat capacity data recently reported for d-Al-Ni-Co [10]. At higher temperatures, the heat capacity continually increases up to about 800K. This trend is consistent with that reported by Edagawa and Kajiyama for both decagonal Al-Cu-Co and icosahedral Al-Pd-Mn quasicrystals [11].

Sample density, ρ, was measured at room temperature as 4.01 g/mL. Thermal conductivity was calculated for each sample using the density, heat capacity, and diffusivity

values; the results are shown in Fig. 4. Again, at low temperatures, our data appear

consistent with previously reported low temperature measurements on d-Al-Ni-Co [4, 7].

Additionally, the trend in the aperiodic data set is comparable to results reported for

icosahedral Al-Cu-Fe over the same temperature range; however, the values are about 2.4

times higher [3]. The values for thermal conductivity are much lower than one would

expect for a typical metal. For comparison, at 373 K the thermal conductivity through the

periodic axis is approximately an order of magnitude lower than that of pure aluminum

(~237 W/m-K), while the thermal conduction through the aperiodic plane is nearly two

orders of magnitude less.

Thermal conductivity was also determined for the 45° sample. These data are

compared to a theoretical thermal transport model. For an isotropic crystal, we would

expect isotropic spherical thermal diffusion under the assumption of a free-electron gas;

however, since diffusion through our material is clearly anisotropic, the thermal ellipsoid

model was employed. From this model, thermal conductivity at a given temperature is

calculated using:

$$\frac{1}{\kappa_\theta} = \frac{1}{\kappa_a} + \left(\frac{1}{\kappa_p} - \frac{1}{\kappa_a} \right) \cos^2 \theta \qquad (3)$$

where κ_p is the measured conductivity through the periodic axis, κ_a is the measured

conductivity though an aperiodic axis, and κ_θ is the predicted conductivity through a sample

having a normal axis at an angle, θ, relative to the periodic axis. For this work $\theta = 45°$. This

model was first developed by Voigt and was successfully used by Bridgman to describe

anisotropic conductivity in metallic single crystals [12, 13]. A more detailed description of

this model has been given elsewhere [14, 15].

As seen in Fig. 4, the thermal ellipsoid model shows very good agreement with the experimental data collected for the 45° sample. The model assumes a linear relationship between temperature and thermal conductivity, in which scattering is proportional to the square of the amplitude of the atomic vibrations about their equilibrium lattice sites. The fact that the model describes the quasicrystal so well suggests that a free-electron gas may be a valid assumption at higher temperatures. A Debye temperature, θ_D, for d-Al-Ni-Co of about 400K has been independently reported by Martin and Inaba [5, 10]. As our measurements were obtained above θ_D, Drude-like behavior is not an unreasonable assumption; however, when considering the clear anisotropy in the thermal transport behavior, it appears that the periodic axis is greatly favored. These trends in the thermal conductivity may be explained in terms of charge carriers and the mean free time of carrier collisions.

Electrical conductivity, σ, may be written as

$$\sigma = \frac{ne^2\tau}{m^*} \qquad (4)$$

where n is the carrier density, m^* is the effective mass, e is the charge on an electron, and τ is the mean free time between collisions. Theoretical analyses by Macia concluded that quasicrystals reasonably follow the Wiedemann-Franz law at high temperatures [16]. This allows us to use the following relationship for thermal conductivity:

$$\kappa_{el} = L_o \frac{ne^2\tau T}{m^*} \qquad (5)$$

where κ_{el} is the electronic contribution to thermal conductivity and L_o is the Lorentz number. While our measured data represent the total thermal conductivity, we have

assumed that over our temperature range the phonon contribution is negligible, therefore, $\kappa_{el} \approx \kappa_{total}$.

Equation (5) implies that for a given temperature, $\kappa_{el} \propto \tau$. If mean free time were independent of the sample axis direction, one would expect the thermal conductivities of the periodic and aperiodic samples to increase with temperature at the same rate; however, when comparing the two samples, we notice that the periodic sample has a much higher rate of increase than does the aperiodic sample. We have ascribed this difference to anisotropy of the carrier mean free time. While the number density of the charge carriers increases independent of direction, the carrier mean free time is substantially shorter along the aperiodic axes. This leads to the observed anisotropy in the rate of increase in thermal conductivity and also accounts for the overall anisotropy seen between the periodic and aperiodic samples.

The agreement of the thermal ellipsoid model with the data obtained from the 45° sample demonstrates that the high-temperature anisotropic transport properties of the 2D quasicrystal may be described in the same manner as those in an anisotropic metallic crystal. Additionally, the successful prediction of transport properties across the 45° sample using a vector-based model suggests that the transport mechanisms of the quasicrystalline plane are not coupled with those of the periodic c-axis.

Conclusions

In this work we present the first high-temperature thermal transport data for the decagonal Al-Ni-Co system. Heat capacity, density, and thermal diffusivity are experimentally measured and employed in the calculation of thermal conductivity. A high

degree of anisotropy in thermal transport between the periodic and aperiodic directions was observed. The thermal ellipsoid model was employed to predict thermal transport behavior through a sample cut with a normal axis 45° from the periodic c-axis. Experimental data collected on such a sample shows excellent agreement with predicted values. This suggests the validity of a Drude free-electron model at high temperatures.

The observed rate of change in thermal conductivity with temperature is much higher along the periodic axis, possibly due to a longer carrier mean free time along the periodic direction.

Acknowledgements

References

(1)   Shechtman, D.; Blech, I.; Gratias, D.; Cahn, J. W. *Phys. Rev. Lett.* **1984**, *53*, 1951-1953.

(2)   Janot, C. *Quasicrystals: A Primer, Second Edition*; Oxford University Press: Oxford, 1995.

(3)   Perrot, A.; Dubois, J. M. In *Ann. Chim. (Paris)*, 1993; Vol. 18, pp 501-511.

(4)   Dian-lin, Z.; Shao-chun, C.; Yun-ping, W.; Li, L.; Xue-mei, W. *Phys. Rev. Lett.* **1991**, *66*, 2778-2781.

(5)   Martin, S.; Hebard, A. F.; Kortan, A. R.; Thiel, F. A. In *Phys. Rev. Lett.*, 1991; Vol. 67, pp 719-722.

(6)   Edagawa, K.; Chernikov, M. A.; Bianchi, A. D.; Felder, E.; Gubler, U.; Ott, H. R. In *Phys. Rev. Lett.*, 1996; Vol. 77, pp 1071-1074.

(7)   Matsukawa, M.; Yoshizawa, M.; Noto, K.; Yokoyama, Y.; Inoue, A. In *Quasicryst., Proc. Int. Conf., 6th*, 1998, pp 479-482.

(8)   Fisher, I. R.; Kramer, M. J.; Islam, Z.; Ross, A. R.; Kracher, A.; Wiener, T.; Sailer, M. J.; Goldman, A. I.; Canfield, P. C. In *Philos. Mag. B*, 1999; Vol. 79, pp 425-434.

(9)   Noguchi, H.; Suzuki, S.; Shibata, H.; Waesda, Y.; Tamura, N.; Urban, K. In *Quasicryst., Proc. Int. Conf., 6th*, 1998, pp 337-340.

(10)   Inaba, A.; Lortz, R.; Meingast, C.; Guo, J. Q.; Tsai, A.-P. *Journal of Alloys and Compounds* **2002**, *342*, 302-305.

(11)   Edagawa, K.; Kajiyama, K. *Mat. Sci. Eng. A* **2000**, *294-296*, 646-649.

(12)   Voigt, W. In *Lehrbuch der Kristallphysik.*

(13)   Bridgman, P. W. *Proc. Amer. Acad. Arts Sci.* **1925**, *61*, 101.

(14)   Carslaw, H. S.; Jaeger, J. C. In *Conduction of Heat in Solids*, 2 ed.; Clarendon Press: Oxford, 1959, pp 1-49.

(15)   Barrow, J. A.; Lemieux, M. C.; Cook, B. A.; Ross, A. R.; Tsukruk, V. V.; Canfield, P. C.; Sordelet, D. J. *Journal of Non-crystalline Solids, In Press.*

(16)   Macia, E. *Applied Phys. Lett.* **2002**, *81(1)*, 88-90.

Figure Captions

Figure 1. Schematic representation of how samples were cut from the single grain d-Al-Ni-Co quasicrystal. **A** is the periodic sample, **B** is the aperiodic sample, and **C** is the 45° sample.

Figure 2. Bulk thermal diffusivity for the d-Al-Ni-Co quasicrystal through different directional axes.

Figure 3. DSC heat capacity measurement for the d-Al-Ni-Co quasicrystal.

Figure 4. Thermal conductivity for the d-Al-Ni-Co quasicrystal. Values calculated using the thermal ellipsoid model (θ=45°) show very good agreement with experimental data from the 45° sample.
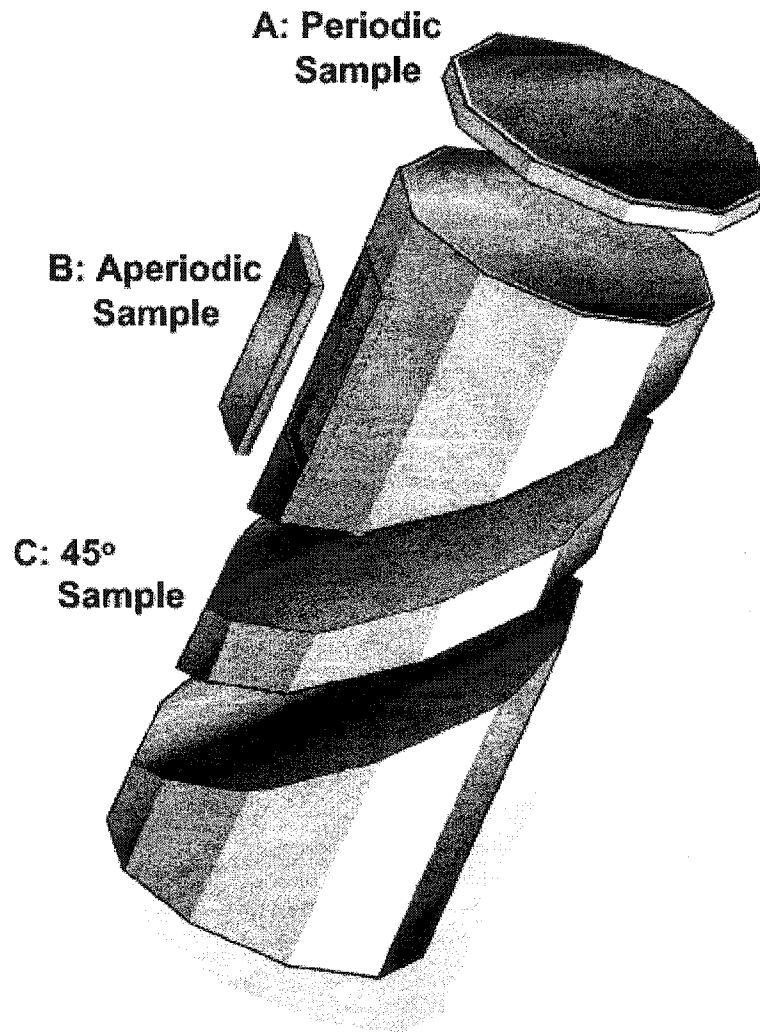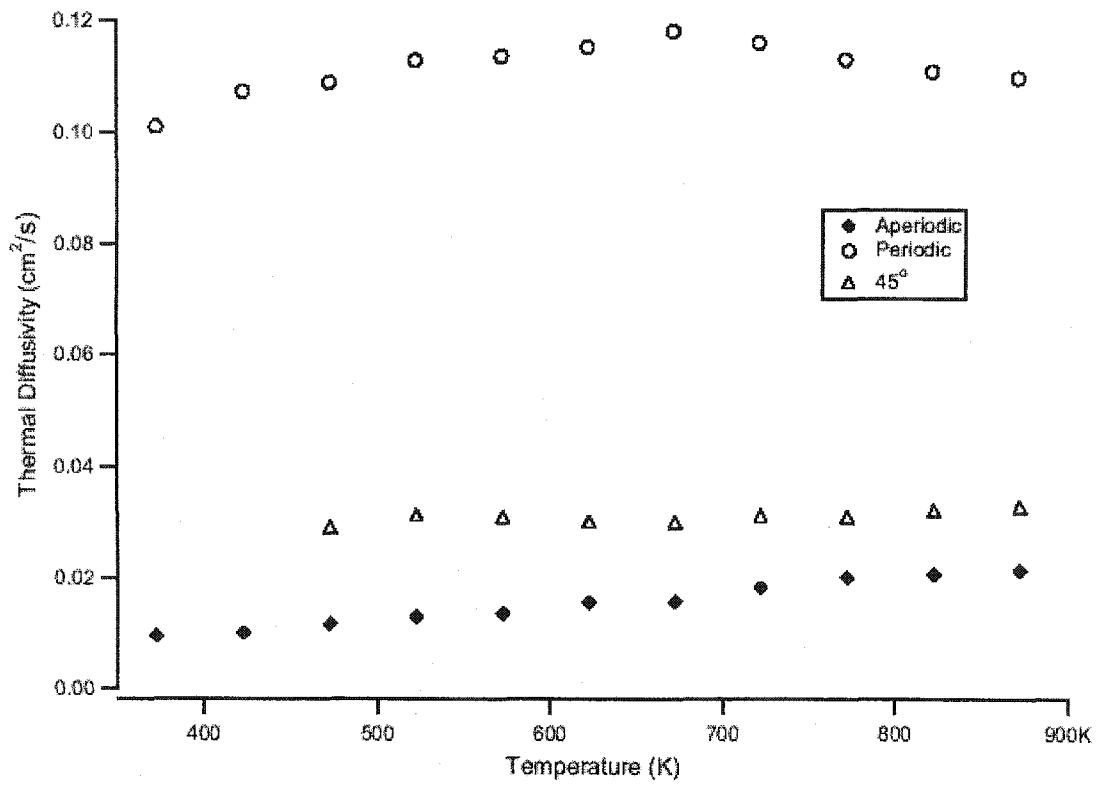
Figure 1

Figure 2
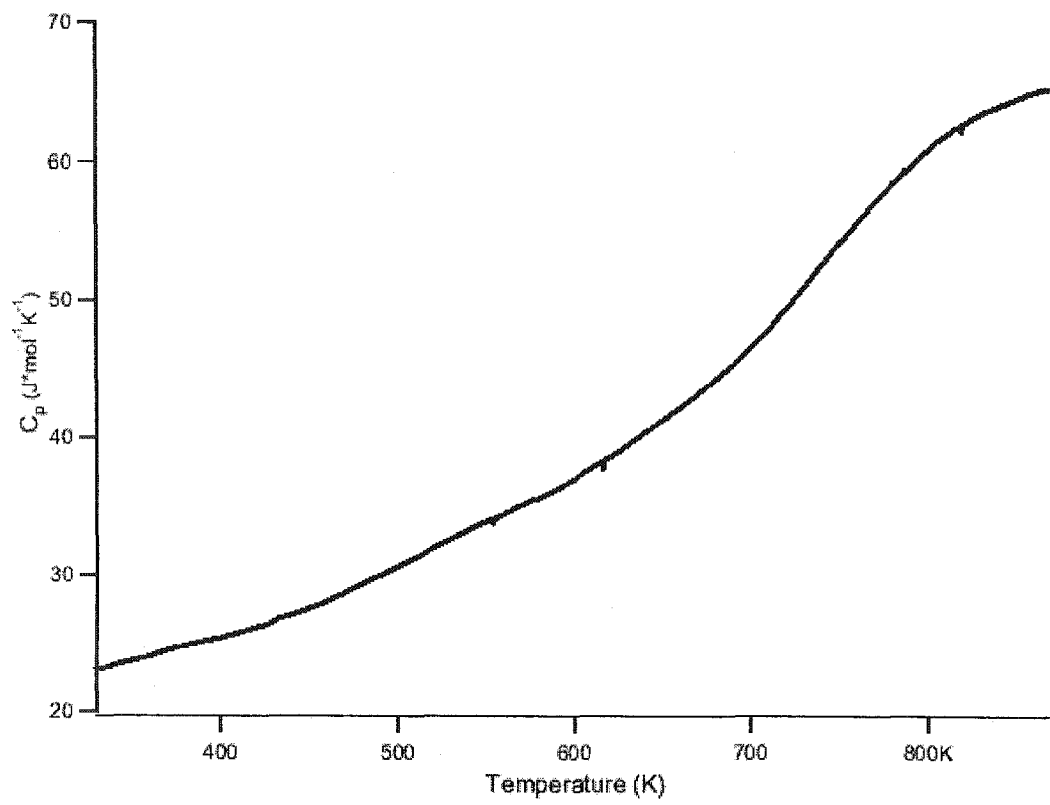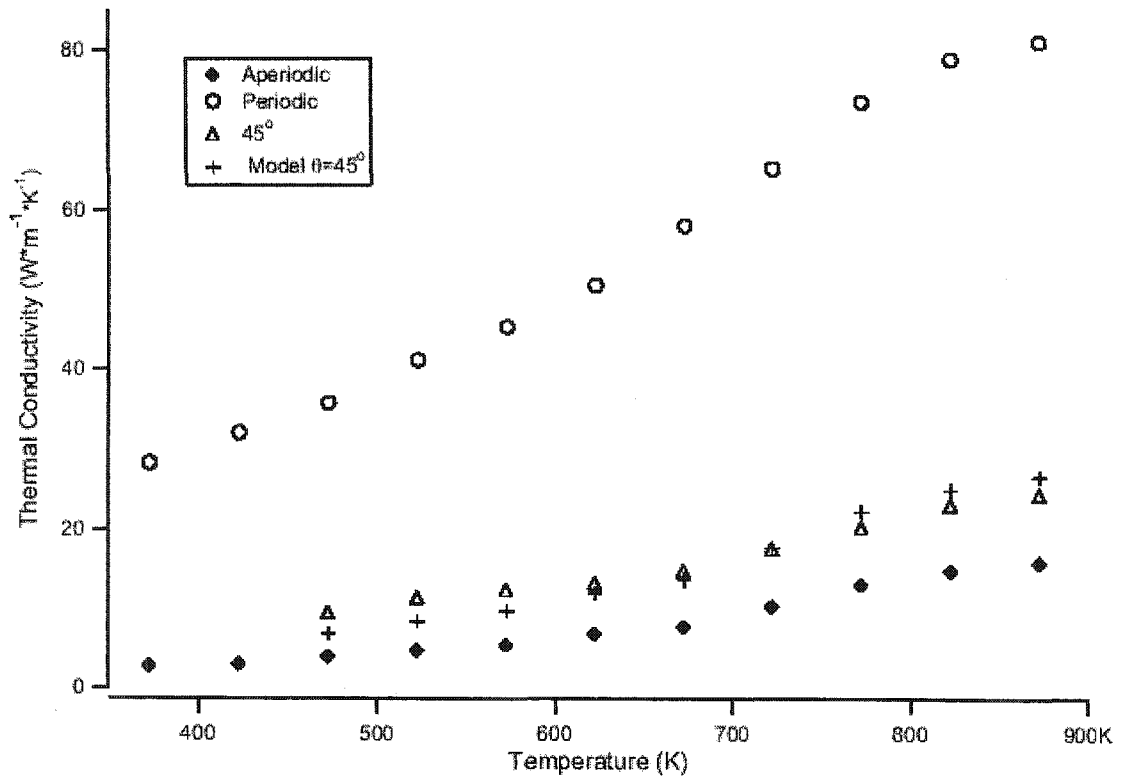
Figure 3

Figure 4

PHOTOEMISSION STUDIES OF THE SPUTTER-INDUCED PHASE TRANSFORMATION ON THE Al-Cu-Fe SURFACE.

J.A. Barrow, V. Fournée, A.R. Ross, P.A. Thiel,
M. Shimoda, and A.P. Tsai

Abstract

The surface of a single grain icosahedral (*i*) Al-Cu-Fe quasicrystalline sample is studied as a function of annealing temperature using Ultra-violet Photoemission Spectroscopy (UPS). Reflection High Energy Electron Diffraction (RHEED) and X-ray Photoelectron Spectroscopy (XPS) are also performed to verify surface structure and composition. The sputtered surface shows structure and chemical composition consistent with that of β-Al-Cu-Fe cubic phase together with a sharp Fermi cut-off. With increasing annealing temperature, the surface structure and composition reverts to that of the quasicrystal. This transformation is correlated with a decrease of the spectral intensity at the Fermi level (E_F). Analysis of the UPS spectra in the region near E_F is performed by fitting the data with a pseudogap function.

Introduction

Quasicrystals are a unique form of matter that exhibit long-range order without periodicity. These aperiodic solids typically have forbidden symmetries, such as five-fold or ten-fold, and unexpected electronic and thermal properties. Since their initial discovery in 1982, several stable and metastable quasicrystalline systems have been identified [1, 2]. These materials are typically binary or ternary metal alloys, yet they exhibit a combination of electronic, physical, and mechanical properties not typically associated with metallic systems. These anomalous properties include low adhesion, good oxidation resistance, and reduced thermal and electrical transport [3].

The electronic structure of quasicrystals, both in the bulk and at the surface, is an important issue both because it affects the physical properties, and because it relates to the fundamental issue of the stabilization of these unique atomic structures. It is proposed that the interaction between the Fermi surface and Bragg planes (as in Hume-Rothery alloys), combined with *sp-d* hybridization effects, result in the formation of a dip in the density of states located at the Fermi level (so-called pseudogap) and provide enhanced stability by reducing the electronic contribution to the total energy of the system.

Electronic structure has primarily been probed using photoemission techniques. Wu *et al.* first reported a pseudogap in photoemission, for a *i*-Al-Pd-Mn surface prepared by sputtering and annealing cycles [4]. On the other hand, results by Stadnik *et al.* showed a clear "metallic" Fermi edge for a surface of similar composition, but prepared by repeated scraping [5, 6]. Although the conflicting results were attributed originally to differences in sample temperatures during measurement [5], it later appeared that the significant

differences in the surface preparation techniques may have influenced the results. Mechanical scraping is intended to remove the native oxide overlayer but can also produce structural disorder in the near surface region, and this can smear out fine structure in the photoemission spectra. Sputter-annealing, on the other hand, has been shown to be capable of producing a surface that is a bulk-termination of the quasicrystal [7-17]. Indeed, a pseudogap was later observed on quasicrystal surfaces prepared by sputtering and annealing [18-21], even when measured at low temperature [21]. Hence, the previous discrepancy was probably due to the disruption of the quasicrystalline structure in the near-surface region by mechanical scraping.

Ultra-violet photoemission spectroscopy (UPS) results have also been published for i-Al-Cu-Fe multi-grain surfaces; however, in both cases the surface was prepared by scraping [5, 22]. In this paper we report the first UPS studies done on a well-characterized, single-grain i-Al-Cu-Fe surface prepared by repeated cycles of sputtering and annealing.

It is well known that sputtering quasicrystalline surfaces at room temperature induces a transformation to a B2 (bcc-type) structure, also known as the β-phase [18, 23-27]. The quasicrystalline surface is restored by annealing the sample at the appropriate temperature. In this work, the transition of the sputtered surface from crystalline to quasicrystalline is investigated as a function of annealing temperature. X-ray photoemission spectroscopy (XPS) and reflection high-energy electron diffraction (RHEED) are performed to fully characterize the composition and structure of the surface before performing UPS measurements. A clear dip in the density of states (DOS) at the Fermi edge appears as annealing temperature increases. Similar to i-Al-Pd-Mn, the opening of the pseudogap is

correlated with a change in surface structure from crystalline to quasicrystalline and a change in composition from a β-Al-Cu-Fe to i-Al-Cu-Fe.

Experimental

The sample was extracted from a single grain i-Al-Cu-Fe ingot. A detailed description of the sample growth method has been given elsewhere [28]. Bulk composition was determined as $Al_{63}Cu_{23}Fe_{13}$ using Secondary Electron Microscopy with Energy Dispersive Spectrometry (SEM-EDS). It was oriented by back-Laue scattering, with its five-fold axis parallel to within $\pm 0.25°$ of the surface normal. The sample was then mechanically polished using diamond paste down to $0.25\mu m$.

All experiments were performed under ultrahigh vacuum (UHV) conditions at a pressure better than 1×10^{-10} Torr. After introduction in the chamber, the sample surface was cleaned by cycles of room temperature Ar^+ sputtering followed by annealing. The surface was sputtered for 15 minutes intervals at 5 keV. Annealing cycles began at 570K and the temperature was increased by 50K per cycle up to 770K. Sputter and annealing cycles were repeated until no oxygen could be detected by XPS.

Experiments were done after annealing the sample at the indicated temperature for 5 min. Typically, an additional 5-10 minutes was required to reach the desired temperature. An optical pyrometer (emissivity $\varepsilon = 0.35$ [29]) was used to measure sample temperature. After data collection, the surface was sputtered again before annealing to the next temperature step. In this manner, each annealing step began with the same surface conditions and the surface contamination due to background gases was kept at a minimum.

Photoemission spectra were collected using a VG ESCALAB MkII. XPS

measurements were done using Mg Kα radiation (1254 eV) from a VG twin anode x-ray

source. UPS was done using He I radiation (21.2 eV) generated with a VG UVL-HI helium

lamp. The energy resolution for XPS and UPS was 1.2 eV and 0.1eV, respectively. All

photoemission spectra were collected at room temperature.

RHEED data were typically collected using a beam energy of 24-25 keV. RHEED

was done during the sputtering to verify consistent starting surface conditions for each

annealing step. Post-annealing RHEED was done after UPS and XPS measurements since

the high energy electron beam could have altered the surface structure.

Results

RHEED Data

Figure 1 shows RHEED patterns of the sputtered surface taken at different angles.

The triangular pattern seen in Fig. 1a suggests that the incident beam is parallel to the [111]

axis of a cubic lattice. The orientation of the [111] lattice pattern suggests that the surface

plane is parallel to a (1,-1,0) type plane. Rotation of the sample about the z-axis produces

the square lattice seen in Figure 1b. The measured angle of this rotation is 34°, which is

consistent with the 35.3° angle between the [111] and [001] axes of the cubic lattice.

Further rotations produce the patterns seen in Fig. 1c and 1d. These were measured at a

rotation of 90° and 270°, respectively, and are consistent with the expected angle between

the [001] and [110] axes.

The indexing of the patterns is consistent with a bcc structure. The observed spots

satisfy the bcc selection rule h+k+l = even, while lattice spots where h,k,l are all odd (fcc

selection rule) are faint or not present. The apparent mixture of spot patterns seen in Fig. 1c

and 1d would not be present if the surface was a perfect bcc structure. These spots are most

likely the result of an overlap between the [110] and [111] axes, as illustrated in Fig. 1c.

Since the angle between these axes is almost $36°$, this type of overlap would occur if the

surface contained twin-related domains with five different orientations corresponding to the

five-fold symmetry of the quasicrystalline substrate. Such twinning has been reported

previously [12, 23, 30].

It should be noted that the β-phase of Al-Cu-Fe is not strictly bcc, because Cu and Fe

are distributed randomly on the body-center sites; however, the electron scattering factors of

Cu and Fe are very close [23, 24]. This leads to the expectation that it will appear bcc in

RHEED, and we have analyzed it as such here. Assuming a bcc lattice, the lattice constant,

a, is calculated as 0.29nm-0.30nm. This is consistent with the analysis of the β-phase

reported by Shen *et al.* [23].

RHEED data are also collected as a function of annealing temperature. Figure 2

shows RHEED patterns collected after annealing at the specified temperature for 5 minutes,

plus the time to reach the desired temperature (10-15 minutes total). A relatively low

temperature anneal, to 570K, has very little effect on the RHEED pattern. After annealing

to 670K, most bcc spots begin to fade from the RHEED pattern, and a streaked pattern

begins to appear. The bcc pattern has nearly disappeared after annealing to 770K, leaving

only the streaked pattern.

Figure 3 shows a RHEED pattern collected after a 1 hour anneal at 770K followed

by an 800K flash. Analysis of the spacing between the RHEED pattern streaks reveals long,

L, and short, S, spacings of constant widths. The width of these spacings is measured over

several images and averaged, yielding an L/S ratio of 1.61 ± 0.04. This value is close to the Golden Mean, τ, where τ = 1.618... The Golden Mean is both an ideal and a frequently-observed characteristic in systems that exhibit five-fold symmetry [2].

XPS Data

The Al 2s, Cu 2$p_{3/2}$, and Fe 2$p_{3/2}$ core-level lines are used to calculate surface composition. Chemical concentrations given below are based on sensitivity factors deduced from elemental standards. More sophisticated calibration would have required the use of specific standard alloys of known composition and having comparable physical characteristics. With Auger electron spectroscopy, it is known that the lack of such proper calibration can lead to errors as large as 15% for Al, 11% for Cu, and 61% for Fe [31]; however, one expects these relative errors to be lower for XPS due to the smaller degree of electron backscattering. The compositions deduced from XPS are: $Al_{50}Cu_{34}Fe_{16}$ (sputtered surface at room temperature), $Al_{64}Cu_{22}Fe_{14}$ (570 K anneal), $Al_{62}Cu_{27}Fe_{11}$ (670 K anneal), $Al_{64}Cu_{26}Fe_{10}$ (770 K anneal). As expected, the Al content is reduced at room temperature due to the preferential sputtering of this lighter element [30, 32]. The composition of the sputtered surface is close to that of the β-Al-Cu-Fe cubic phase. Upon annealing, the composition quickly reverts to one consistent with the icosahedral phase.

UPS Data

Room temperature valence-band spectra are shown in Fig. 4 for the sputtered and annealed surfaces. Two main peaks are apparent in these spectra. These are attributed to

the Cu 3d band (~4eV) and the Fe 3d band (near E_f), based soft x-ray emission spectroscopy and resonant photoemission experiments [33, 34].

With increasing annealing temperature, the Cu 3d band shifts to higher binding energies by a total of ~0.6 eV. We also notice that the intensity of the Cu 3d band increases significantly with respect to the Fe 3d band. The position of the Cu 3d band is strongly dependent on the local environments around Cu atoms. Band shifts and changes in intensities reflect the structural and chemical rearrangements that occur during the annealing. The energy shift corresponds to an apparent filling of the Cu 3d band by hybridization with extended *sp* states [35]. In the region near E_F, the peak corresponding to the center of gravity of the Fe 3d band slightly shifts towards higher binding energies. There is a marked reduction in the slope of the Fermi edge, usually interpreted as evidence of a dip in the DOS(E_f), the so-called "pseudo-gap" [3, 4, 18, 22, 36].

We attempt to quantify the pseudo-gap by using a fitting procedure similar to that first proposed by Mori *et al.* [22]. This model provides a means to simulate the spectral region near the Fermi edge and provides quantitative parameters to characterize the pseudogap. While the reduction in the DOS due to the pseudo-gap has previously been assumed to be of Lorentzian line-shape [6, 22], we found that better results could be obtained across our data set by fitting the dip in the DOS using a pseudo-Voight :

$$V(E) = \eta \left[\frac{\Gamma^2}{\left(E - E_F\right)^2 + \Gamma^2} \right] + (1 - \eta) \exp\left[\frac{-\left(E - E_F\right)^2}{2\sigma^2} \right] \qquad (1)$$

This linear combination of a Lorentzian function and a Gaussian function share the same FWHM, Γ, which is related to σ by $\Gamma = 2\sigma\sqrt{2\ln 2}$. The term η is a weighting factor which ranges from $\eta=0$ (full Gaussian) to $\eta=1$ (full Lorentzian).

We assume that the normal DOS at E_f may be approximated as a linear function multiplied by the Fermi distribution function at room temperature. To account for experimental broadening, this product is convoluted with a Gaussian distribution:

$$I(E) = \int N(ax+b)[1-CV(x)]f(x,T)\exp\left[\frac{-(x-E)^2}{(\Delta E)^2}\right]dx \qquad (2)$$

The coefficients a and b are determined by a linear fit of the region just before the dip in the DOS before the Fermi edge, typically in the E_B range from -0.1eV to -0.7eV. N is the Gaussian normalization constant, and ΔE is the energy width of the experimental resolution Gaussian function. The value C is the dip constant. It ranges from C=0, where no pseudogap is present, to C=1, where the DOS is zero at E_F.

The results of these fits are shown in Figure 5. Residuals presented are multiplied by a factor of 10. Values for C, Γ, and η are reported in Table 1. For the spectra shown in figures 5a and 5b good fits are obtained with η values of almost 1. This signifies that the line-shape of the reduction in DOS is nearly Lorentzian. For figures 5c and 5d good fits are obtained using line-shapes that are nearly Gaussian, with η values closer to zero.

Discussion

These high-resolution UPS experiments reveal a sharp metallic like Fermi edge for the sputtered surface. Based also on the RHEED patterns, and the composition established from XPS, we associate this with the B2 (β-phase) structure. The metallic character of this crystalline overlayer is confirmed quantitatively by the low value of the C parameter returned by the fitting procedure. The shape of the Fermi edge begins to change upon annealing and the dip at E_F becomes more pronounced with higher annealing temperatures. After annealing to 570K we observe only a small change in the RHEED pattern, yet the dip in DOS (E_F) has become apparent. Additionally, XPS yields a surface composition consistent with the icosahedral phase.

Annealing to 670K induces much larger depression in the DOS correlated with the appearance of a quasicrystalline RHEED pattern. Between the 670K anneal and the 770K anneal the dip shows very little change. The values for C and Γ are comparable with those previously reported for polycrystalline i-Al-Cu-Fe [6, 22].

When comparing the results of the different techniques, the depth sensitivity of each technique must be considered. This is important because, after sputtering, there is undoubtedly a compositional and structural gradient normal to the surface. As we anneal the sample we are observing the relaxation to the stable state. With increasing annealing temperatures the thickness of the β-phase overlayer decreases, until the surface has fully reverted to quasicrystalline. The reversion will be sensed first by the techniques that are most bulk-sensitive and least surface-sensitive.

It appears from XPS that the surface returns to a quasicrystalline composition after only a brief anneal at 570K. Similarly, UPS data indicates that the structure is reverting to

quasicrystalline, marked by the appearance of the pseudo-gap. In contrast, the RHEED data is still clearly dominated by the β-phase for this annealing temperature (Fig 2b), due to the lower penetration depth of RHEED [37]. Additionally, RHEED may show little change because it has a much greater sensitivity to the bcc structure than the icosahedral structure. This difference is apparent when comparing the intensity of features in Figure 2a with those in Figure 3. Even after annealing to 770K the RHEED image still shows some evidence of a bcc structure (Fig 2d). Scanning tunneling microscopy studies have shown that annealing temperatures of 870K for 3 hours are required to fully return the surface structure to quasicrystalline [17, 38].

Conclusion

This study reports the first UPS investigation of a single grain i-Al-Cu-Fe sample with a well defined 5-fold surface. Preparation and characterization of the surface is an important step toward obtaining meaningful results for experiments of this type. Sample quality has been proven using XPS (composition) and RHEED (long-range order) data collected in conjunction with UPS data. This combined investigation of geometrical, compositional, and electronic surface structure has clearly demonstrated that the depressed DOS at E_f is intrinsic to the i-Al-Cu-Fe surface. This dip is attributed to the development of the pseudogap as the surface reverts from the β-phase to the quasicrystalline.

Acknowledgements

References

(1)   Shechtman, D.; Blech, I.; Gratias, D.; Cahn, J. W. *Phys. Rev. Lett.* **1984**, *53*, 1951-1953.

(2)   Janot, C. *Quasicrystals: A Primer, Second Edition*; Oxford University Press: Oxford, 1995.

(3)   Stadnik, Z. M. *Physical Properties of Quasicrystals. [In: Springer Ser. Solid-State Sci., 1999; 126]*, 1999.

(4)   Wu, X.; Kycia, S. W.; Olson, C. G.; Benning, P. J.; Goldman, A. I.; Lynch, D. W. *Phys. Rev. Lett.* **1995**, *75*, 4540-4543.

(5)   Stadnik, Z. M.; Purdie, D.; Garnier, M.; Baer, Y.; Tsai, A. P.; Inoue, A.; Edagawa, K.; Takeuchi, S. *Phys. Rev. Lett.* **1996**, *77*, 1777-1780.

(6)   Stadnik, Z. M.; Purdie, D.; Garnier, M.; Baer, Y.; Tsai, A. P.; Inoue, A.; Edagawa, K.; Takeuchi, S.; Buschow, K. H. J. *Phys. Rev. B: Condens. Matter* **1997**, *55*, 10938-10951.

(7)   Thiel, P. A.; Goldman, A. I.; Jenks, C. J. In *Physical Properties of Quasicrystals*, 1999; Vol. 126, pp 327-359 and references therein.

(8)   Capitan, M. J.; Alvarez, J.; Joulaud, J. L.; Calvayrac, Y. *Surface Science* **1999**, *423*, L251-L257.

(9)   Shen, Z.; Stoldt, C. R.; Jenks, C. J.; Lograsso, T. A.; Thiel, P. A. *Phys. Rev. B* **1999**, *60*, 14688-14694.

(10)   Cappello, G.; Schmithusen, F.; Chevrier, J.; Comin, F.; Stierle, A.; Formoso, V.; De Boissieu, M.; Boudard, M.; Lograsso, T.; Jenks, C.; Delaney, D. *Mat. Sci. Eng. A* **2000**, *294-296*, 822-825.

(11)   Ledieu, J.; McGrath, R.; Diehl, R. D.; Lograsso, T. A.; Delaney, D. W.; Papadopolos, Z.; Kasner, G. *Surface Science* **2001**, *492*, L729-L734.

(12)   Naumovic, D.; Aebi, P.; Schlapbach, L.; Beeli, C. *Mat. Sci. Eng. A* **2000**, *294-296*, 822-885.

(13)   Schmithusen, F.; Boissieu, M. D.; Boudard, M.; Chevrier, J.; Comin, F. *Materials Science & Engineering, A: Structural Materials: Properties, Microstructure and Processing* **2000**, *A294-296*, 867-870.

(14)   Shen, Z.; Raberg, W.; Heinzig, M.; Jenks, C. J.; Fournee, V.; Van Hove, M. A.; Lograsso, T. A.; Delaney, D.; Cai, T.; Canfield, P. C.; Fisher, I. R.; Goldman, A. I.; Kramer, M. J.; Thiel, P. A. *Surface Science* **2000**, *450*, 1-11.

(15)   Cai, T.; Shi, F.; Shen, Z.; Gierer, M.; Goldman, A. I.; Kramer, M. J.; Jenks, C. J.; Lograsso, T. A.; Delaney, D. W.; Thiel, P. A.; Van Hove, M. A. *Surface Science* **2001**, *495*, 19-34.

(16)   Barbier, L.; Le Floc'h, D.; Calvayrac, Y.; Gratias, D. *Physical Review Letters* **2002**, *88*, 085506/085501-085506/085504.

(17)   Papadopolos, Z.; Kasner, G.; Ledieu, J.; Cox, E. J.; Richardson, N. V.; Chen, Q.; Diehl, R. D.; Lograsso, T. A.; Ross, A. R.; McGrath, R. *Phys. Rev. B* **2002**, *66*, 184207/184201-184207/184213.

(18)   Naumovic, D.; Aebi, P.; Schlapbach, L.; Beeli, C.; Lograsso, T. A.; Delaney, D. W. *Phys. Rev. B* **1999**, *60*, R16330-R16333.

(19)   Stadnik, Z. M. *Mat. Sci. Eng. A* **2000**, *294-296*, 470-474.

(20)   Stadnik, Z. M.; Purdie, D.; Baer, Y.; Lograsso, T. A. *Phys. Rev. B* **2001**, *64*, 214202.

(21)   Shaub, T.; Delahaye, J.; Berger, C.; Guyot, H.; Belkhou, R.; Taleb-Ibrahimi, A.; Calvayrac, Y. *Eur. Phys. J. B* **2001**, *20*, 183-188.

(22)   Mori, M.; Matsuo, S.; Ishimasa, T.; Matsuura, T.; Kamiya, K.; Inokuchi, H.; Matsukawa, T. *J. Phys.: Condens. Matter* **1991**, *3*, 767-771.

(23)   Shen, Z.; Kramer, M. J.; Jenks, C. J.; Goldman, A. I.; Lograsso, T.; Delaney, D.; Heinzig, M.; Raberg, W.; Thiel, P. A. *Phys. Rev. B: Condens. Matter* **1998**, *58*, 9961-9971.

(24)   Shi, F.; Shen, Z.; Delaney, D. W.; Goldman, A. I.; Jenks, C. J.; Kramer, M. J.; Lograsso, T.; Thiel, P. A.; van Hove, M. A. *Surf. Sci.* **1998**, *411*, 86-98.

(25)   Zurkirch, M.; Erbudak, M.; Kortan, A. R. In *Quasicryst., Proc. Int. Conf., 6th*, 1998, pp 67-70.

(26)   Naumovic, D.; Aebi, P.; Schlapbach, L.; Beeli, C.; Lograsso, T. A.; Delaney, D. W. In *Quasicryst., Proc. Int. Conf., 6th*, 1998, pp 749-756.

(27)   Shimoda, M.; Guo, J. Q.; Sato, T. J.; Tsai, A. P. *Surf. Sci.* **2000**, *454-456*, 11-15.

(28)   Jenks, C. J.; Pinhero, P. J.; Shen, Z.; Lograsso, T. A.; Delaney, D. W.; Bloomer, T. E.; Chang, S. L.; Zhang, C. M.; Anderegg, J. W.; Islam, A. H. M. Z.; Goldman, A. I.; Thiel, P. A. In *Quasicryst., Proc. Int. Conf., 6th*, 1998, pp 741-748.

(29)   Unpublished Results.

(30)   Shen, Z.; Pinhero, P. J.; Lograsso, T. A.; Delaney, D. W.; Jenks, C. J.; Thiel, P. A. *Surf. Sci.* **1997**, *385*, L923-L929.

(31)   Jenks, C. J.; Bloomer, T. E.; Kramer, M. J.; Lograsso, T. A.; Delaney, D. W.; Ross, A. R.; Sordelet, D. J.; Besser, M. F.; Thiel, P. A. *Applied Surface Science* **2001**, *180*, 57-64.

(32)   Rouxel, D.; Gavatz, M.; Pigeat, P.; Weber, B. In *New Horiz. Quasicrystals, [Conf.]*, 1997, pp 173-180.

(33)   Stadnik, Z. M.; Stroink, G. In *Phys. Rev. B: Condens. Matter*, 1993; Vol. 47, pp 100-106.

(34)   Belin-Ferre, E.; Fournee, V.; Dubois, J.-M. *J. Phys.: Condens. Matter* **2000**, *12*, 8159-8177.

(35)   Fournee, V.; Belin-Ferre, E.; Dubois, J.-M. In *J. Phys.: Condens. Matter*, 1998; Vol. 10, pp 4231-4244.

(36)   Belin, E.; Dankhazi, Z.; Sadoc, A.; Flank, A. M.; Poon, J. S.; Mueller, H.; Kirchmayr, H. In *Quasicryst., Proc. Int. Conf., 5th*, 1995, pp 435-438.

(37)   Woodruff, D. P.; Delchar, T. A.; Cambridge University Press: Cambridge, 1986, pp 76-81.

(38)   Cai, T.; Ledieu, J.; McGrath, R.; Fournee, V.; Lograsso, T.; Ross, A.; Thiel, P. *Surface Science* **2003**, *526(1-2)*, 115-120.

Table and Figure Captions

Table 1. Pseudogap parameters generated using Eqn. 2 to fit the UPS spectra in the region

near the Fermi edge.

Figure 1. RHEED patterns of the sputtered Al-Cu-Fe surface. The patterns are shown with

the incident beam parallel to the a) [111] axis, b) [001] axis, and c) [110] axis.

Pattern d is the also of the [110] axis, rotated $180°$ relative to pattern c.

Figure 2. RHEED patterns of Al-Cu-Fe for the a) sputtered, b) annealed at 570 K, c)

annealed at 670 K, d) annealed at 770 K surfaces.

Figure 3. RHEED pattern for the Al-Cu-Fe surface after annealing to 770 K for 1 hour and

an 800 K flash. The spacing of the streaks are of constant widths, L, and S. The

ratio L:S is 1.61, close to the Golden Mean.

Figure 4. Room temperature valance-band spectra of Al-Cu-Fe surfaces, taken using He I

($h\upsilon$=21.2 eV) radiation. Surface treatments are labeled.

Figure 5. High resolution UPS spectra of the region close to the Fermi edge. Surface

treatments are labeled. Spectra are fit using Eqn. 2. Residuals of the fit are shown.

The intensity scale of the residuals are expanded by 10 relative to the

experimental spectra.

Table 1

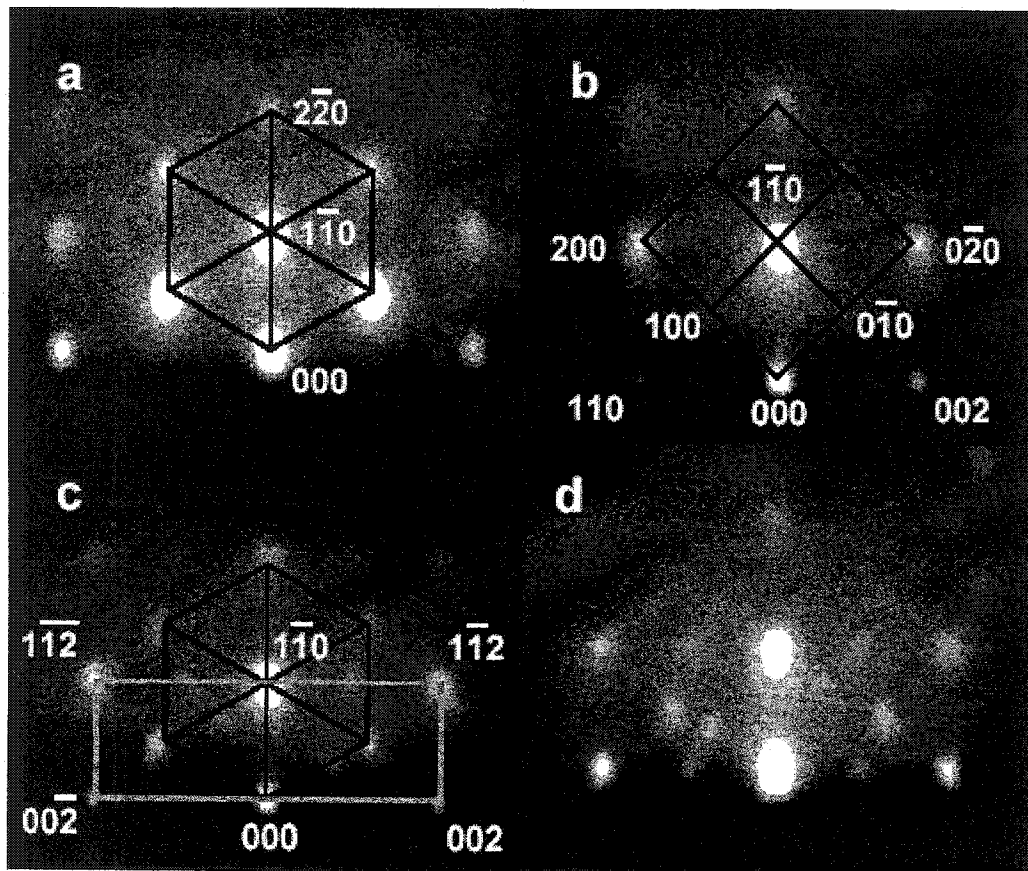| Anneal Temperature	C	Γ (eV)	η
770K	0.640(2)	0.345(2)	0.988(5)
670K	0.637(1)	0.332(5)	0.982(2)
570K	0.497(2)	0.571(3)	0.169(1)
298K	0.191(1)	0.396(3)	0.0083(1)

Figure 1

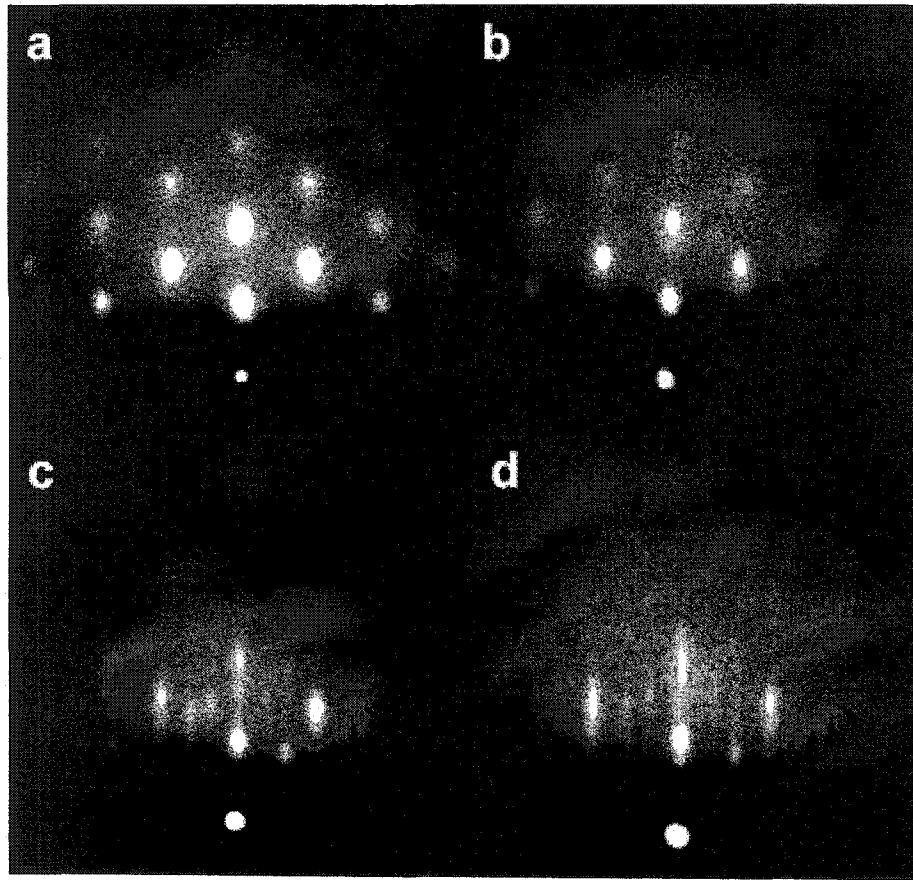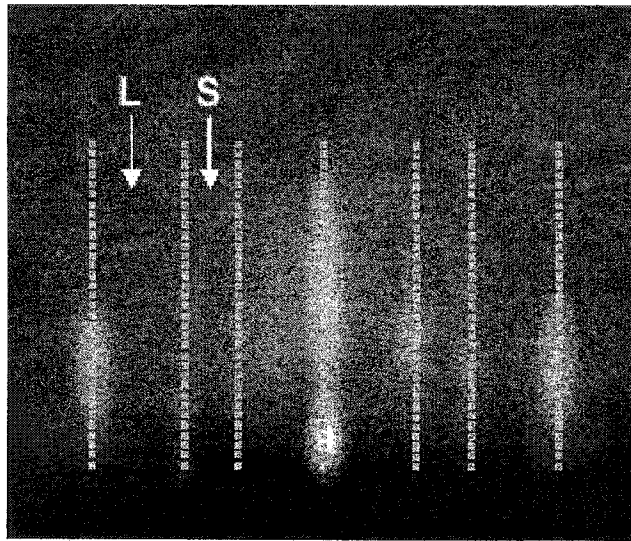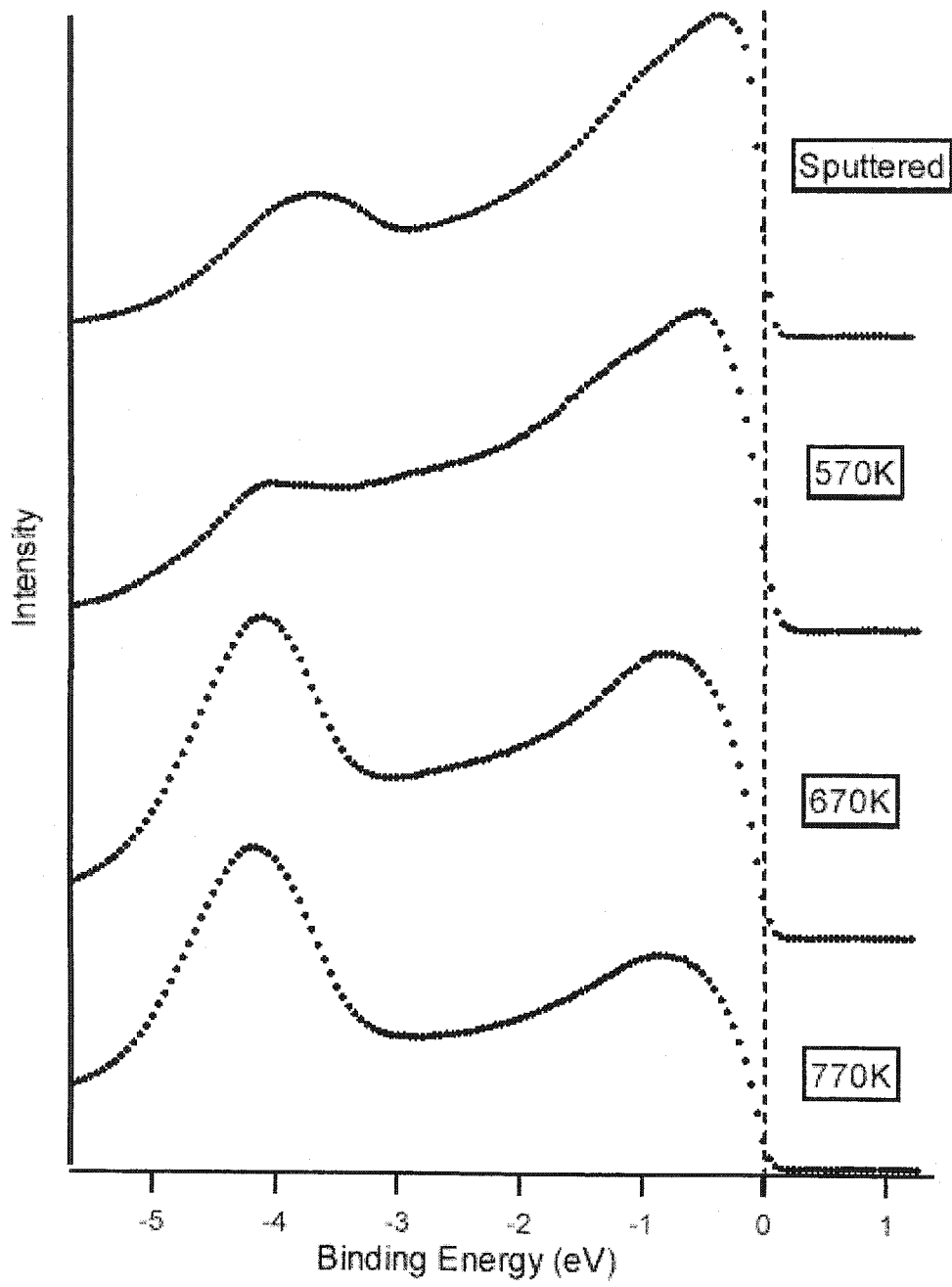Figure 2

Figure 3

Figure 4

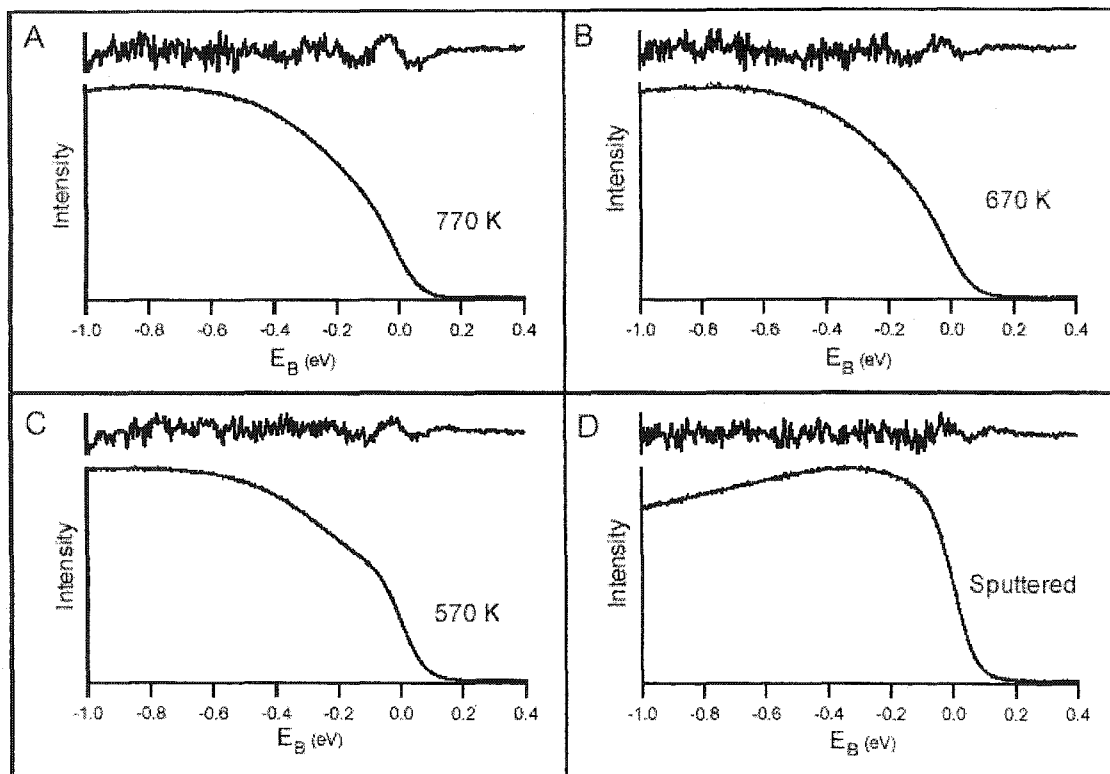Figure 5

GENERAL CONCLUSIONS

The work presented in this dissertation has investigated three distinct areas of interest in the field of quasicrystals: bulk structure, transport properties, and electronic structure. First, we have described the results of a study which explored the fundamental interactions between the atomic species of the icosahedral Al-Pd-Mn quasicrystal. The goal of this work was to determine whether the pseudo-MacKay or Bergman type clusters have a special stability or are merely a geometric coincidence. This was carried out by using laser vaporization to produce gas-phase metal clusters, which were analyzed using time-of-flight mass spectrometry. Both the kinetic and thermodynamic stabilities of the clusters were probed. The data indicated no special stability for either pseudo-MacKay or Bergman type clusters as isolated units. This, however, is not proof that these clusters are simply a geometric coincidence. It is possible that such clusters only have stability in the framework of the bulk matrix and do not exist as isolated units.

Next, we have reported our investigations of the bulk thermal transport properties of a decagonal Al-Ni-Co two dimensional quasicrystal in the temperature range 373K-873K. The properties of a sample oriented along the periodic axis and another oriented along the aperiodic axis were measured. A high degree of anisotropy was observed between the aperiodic and periodic directions. Additionally, the properties were measured for a sample miscut to an orientation 45° off-axis. The properties of the miscut sample were shown to have good agreement with a theoretical model used to describe thermal transport in metallic single crystals. This model only considers thermal transport by a free-electron gas; therefore, agreement with experimental data suggests the validity of the Drude free-electron

model for the decagonal Al-Ni-Co at these temperatures. Consequently, the observed anisotropy may be adequately described using classical transport equations. Transport behavior is described in terms of charge carriers and the mean-free time between carrier collisions. It is concluded that the mean-free time is much longer in the periodic direction than in the aperiodic direction. This difference produces the observed anisotropy in thermal transport.

The third study presented a detailed analysis of the reversible, sputter-induced phase transformation which occurs on the 5-fold surface of an icosahedral Al-Cu-Fe quasicrystal. Reflection high-energy electron diffraction (RHEED), x-ray photoemission spectroscopy (XPS), and ultra-violet photoemission spectroscopy (UPS) data were collected as a function of annealing temperature and were used to probe surface structure, surface composition, and electronic structure, respectively. The composition and structure of the sputtered surface are consistent with a transformation to the β-Al-Cu-Fe cubic structure, and shows a sharp metallic cut-off in the spectral intensity of the electronic structure at the Fermi edge. Upon annealing the surface reverts to a quasicrystalline composition and structure. This transformation has been correlated with a reduction in the spectral intensity of the electronic structure at the Fermi level. These data clearly demonstrate that the observed reduction is intrinsic to a quasicrystalline surface. It is concluded that this is due to the opening of a pseudo-gap in the electronic density of states as the surface reverts from β-Al-Cu-Fe to quasicrystalline.

APPENDIX A. PALLADIUM CLUSTERS FORMED ON THE COMPLEX PSEUDO TEN-FOLD SURFACE OF THE ξ'-Al$_{77.5}$Pd$_{19}$Mn$_{3.5}$ APPROXIMANT CRYSTAL

A paper submitted to *Surface Science*

V. Fournée, J.A. Barrow, M. Shimoda, A.R. Ross, T.A. Lograsso,
P.A. Thiel, and A.P. Tsai

Abstract

The growth and properties of a Pd thin film deposited on a structurally complex surface are studied by scanning tunnelling microscopy/spectroscopy (STM/STS) and photoemission spectroscopy. The substrate is the pseudo ten-fold surface of the ξ'-Al$_{77.5}$Pd$_{19}$Mn$_{3.5}$ crystal, an approximant of the AlPdMn quasicrystalline phase. Spectroscopic data are consistent with a low density of electronic states around the Fermi level for the clean surface, in agreement with the poorly conducting nature of this intermetallic alloy. Deposited Pd atoms readily form small metal particles with relatively homogeneous size on the substrate, for coverages ranging from the submonolayer regime up to 7 ML. The Pd particles do not coalesce with time and are relatively stable upon annealing up to 920 K. Their average size increases slightly with film thickness. The local electronic structure of the Pd thin film has been studied by STS and appears to be particle-size dependent, with a transition from non-metal to metal, deduced from I(V) characteristics with increasing particle size. A shift of the Pd-$3d$ core level is also measured by photoemission, and it can be correlated with a shift of the Pd-d band toward the Fermi level. The growth mode of the Pd

film on the ξ' approximant surface and its electronic structure are discussed in relation to Pd

thin films grown on metal-oxides that are used as model catalysts.

Introduction

Quasicrystals (QCs) are well-ordered materials without periodicity, and typically

exhibit non-crystallographic (such as 5-fold or 10-fold) rotational symmetries. Since their

discovery in 1984 by Shechtman *et al.* [1], many ternary as well as binary stable

quasicrystalline phases have been discovered [2,3]. Unusual physical properties have been

observed in these intermetallic alloys [4]. For example, Al-based QCs are usually poor

electronic and thermal conductors, and behave more like semiconductors than like classical

intermetallics. At room temperature, they are brittle and hard. When exposed to air, their

surface is covered by a thin protective alumina overlayer that shows reduced adhesion and

low friction [5]. Because of these properties, quasicrystals could find use in technological

applications. However, their brittleness is a disadvantage because it has, and will,

restrict(ed) them to the form of coatings or composite materials.

Quasicrystals have also excited interest for a different type of physical property--

catalytic activity. Indeed, many Al-based quasicrystals contain approximately 20 at.% of a

known catalyst like Pd or Cu. Already in 1994, there was an indication that quasicrystals

exhibited good, or even superior, activity for methanol decomposition, relative to other Al-

Pd crystalline compounds or pure Pd or Cu metals [6]. More recently, the Al-Cu-Fe system

was tested as a catalyst for the steam reforming of methanol, using different alloy compositions [7-9]. Among them, the icosahedral phase $Al_{63}Cu_{25}Fe_{12}$ exhibited the highest level of activity, comparable to existing catalysts currently used in industry [8,9]. Here the brittleness of quasicrystals is clearly an advantage as they can easily be crushed into high surface area powder. Therefore these materials, which are stable phases up to high temperatures, have serious potential to be used as an industrial catalysts in the near future.

Usual practical catalysts are composed of active metal particles dispersed on a porous oxide powder [10]. Due to the complexity of the catalytic phenomenon, surface science studies often use "model catalysts" to simulate the key features of practical industrial catalysts [11-13]. The idea is to try to understand the structure-reactivity relations to improve existing solutions [11]. Model catalysts are made of metal clusters (like Pd, Pt, Au, Cu, Rh) deposited in UHV conditions on oxides or oxide thin films (SiO_2, Al_2O_3, TiO_2, MgO). In the latter case, the oxide films are grown *in-situ* and must be sufficiently conductive for typical surface science techniques (such as electron spectroscopies) to be used. Metal clusters on oxide surfaces are then obtained either by cluster deposition or from the vapour after nucleation and growth of 3D metal islands [12]. Formation of 3D clusters, rather than flat atomic layers, results from the high surface free energy of most metals compared to oxide surfaces. Once this model system has been synthesized, it is possible to study the influence of various parameters on the reactivity toward a given chemical reaction, such as the effects of size and structure of the metal particles, nature of the oxide substrate, and the influence of electronic properties [13,14].

Here we want to adopt a similar approach to understand the superior catalytic activity of quasicrystalline powders. Therefore, we need to construct a model system simulating the

key features of the "real world" QC powder catalyst. In the experiments cited previously [8,9], the powders were first leached in a NaOH aqueous solution for several hours and then rinsed thoroughly in distilled water to remove completely the alkaline solution. After leaching, Cu and copper oxide in addition to bulk quasicrystal were observed in the X-ray powder diffraction pattern [9]. The authors suggested that the catalytic powder prepared in this manner actually consist of Cu and copper oxide particles sitting on top of the quasicrystalline surface. How these particles are formed is unknown yet; but an enrichment in transition metal at the surface is induced by the Al dissolution during the leaching treatment. Then crystallization into particles must involve atomic diffusion processes. These observations support the idea that a "quasicrystal-supported model catalyst" might be constructed by forming metallic clusters on the surface of a monograin quasicrystal.

In a first attempt to construct this model system, we use the surface of an approximant single crystal as the substrate. Approximant crystals and quasicrystals are intimately related [4,15]. They are periodic crystals with large unit cells, found in nearby regions of the phase diagram, with a local order that closely matches the local order found in QCs. Their physical and chemical properties are also very similar. Once a clean surface of this approximant has been prepared in UHV, we observe *in-situ* the formation of Pd clusters on this surface by using several surface science techniques. We follow the film morphology with increasing Pd coverage by scanning tunneling microscopy (STM). The electronic structure of the substrate and of the film is also studied by photoemission (XPS and UPS) and tunneling spectroscopies (STS). Experimental details are provided in section II, then the results are presented and discussed in section III. Conclusions and future possible directions of this work are given in section IV.

Experimental

The experiments described in the following were performed on the pseudo 10-fold

surface of the ξ'-Al$_{77.5}$Pd$_{19}$Mn$_{3.5}$ approximant. The ξ' phase is an orthorhombic crystal with

Pnma space group and lattice parameter a$_{\xi'}$=23.4 Å, b$_{\xi'}$=16.5 Å and c$_{\xi'}$=12.4 Å [16]. A large

single grain was grown by the Bridgman method. A sample was extracted from this grain,

with its surface perpendicular to the **b** axis which shows the pseudo 10-fold symmetry. The

surface orientation was determined by back-Laue scattering to within ±0.25°. The sample

was then mechanically polished down to a final roughness of 0.25 μm using diamond paste,

and mounted on a Mo holder for investigation in the ultra-high vacuum (UHV) environment.

The UHV system was composed of several chambers connected together. One chamber was

equipped with an Omicron room temperature STM. A preparation chamber was equipped

with an electron beam evaporator and a reflection high-energy electron diffraction (RHEED)

system, in addition to standard sputtering and annealing tools. A third chamber contained a

hemispherical electron energy analyser with X-ray and ultra-violet photon sources, allowing

photoemission (XPS and UPS) and photodiffraction (XPD) to be performed. A clean surface

was achieved by cycles of Ar$^+$ sputtering at room temperature followed by annealing. The

Ar$^+$ beam energy was decreased from 3 to 1.5 kV, and the etching time was about 30

minutes for each cycle. The annealing temperature was 820 K, except for the last two cycles

where the temperature was increased to 870 K prior to the STM experiment. The

temperature given here is that of the Mo holder measured by an optical pyrometer. The

temperature of the ξ'-approximant surface might thus be lower. Assuming that the

emissivity of the ξ'-$Al_{77.5}Pd_{19}Mn_{3.5}$ approximant is not very different from that of the $Al_{72}Pd_{19.5}Mn_{8.5}$ icosahedral QC, then the difference between sample surface and sample holder temperatures is smaller than 20°. Palladium was deposited at room temperature using an electron beam evaporator with a flux F=1.6 x 10^{-3} ML/s. The evaporator was fully outgassed for several hours before dosing. The flux was estimated from STM data on Pd(111) and this estimation was crossed-checked by measuring the intensity of the XPS core-level spectra. This was achieved by measuring the Al $2p$ core levels at various emission angles (ϕ, with respect to the surface normal) after the surface had been covered by a Pd film of thickness d. If I_0 is the intensity of the Al $2p$ signal at the substrate-film interface, the measured signal I is to a first approximation given by $I=I_0 e^{-d/\lambda.\cos(\phi)}$, where λ is the inelastic mean-free path of Al $2p$ photoelectrons in the Pd film [17]. The film thickness estimated in this way is only slightly smaller than that estimated from STM images. The reason for this small discrepancy is that the above approximation is only valid for perfect layer-by-layer growth, whereas we will see that the Pd film deposited on the ξ' surface is rough. The base pressure in the preparation chamber was in the range of 10^{-10} mbar whereas the pressure in the STM chamber was in the low 10^{-11} mbar. The pressure rose into the low 10^{-9} mbar range during Pd deposition, producing some contamination on the surface. Oxygen, but no carbon, could be detected by photoemission on the ξ' surface after dosing with 3.5 ML. We therefore have to consider that this contamination might affect Pd thin film growth.

For the sake of comparison, we also dosed Pd under the same conditions of temperature and flux on two other surfaces : that of an HOPG sample (highly oriented pyrolytic graphite) and the Pd(111) surface. The HOPG sample was cleaved in air and immediately loaded into the UHV chamber without further treatment. The Pd(111) surface

was cleaned by repeated cycles of Ar^+ sputtering (1kV for 20 min) and annealing at 870K, except for the last few cycles where the sample was flash annealed to about 1070K to obtain large terraces. In this case, neither oxygen nor carbon contamination could be detected by XPS after dosing Pd on this surface. In this paper, we also compare the morphology of the Pd film formed on the surface of the ξ' approximant to that of a Ag film grown on the same substrate. The STM image of the Ag film used below has been acquired in the Ames Laboratory. The surface and the Ag film were prepared using similar experimental conditions and details can be found in reference [18]. In particular, silver was deposited at room temperature with a flux $F=10^{-3}$ ML/s.

Results and discussion.

The substrate surface structure.

The pseudo 10-fold (p-10f) surface of the ξ'-$Al_{77.5}Pd_{19}Mn_{3.5}$ approximant has already been described in [19]. We summarize the main results in the following.

Very large terraces are observed by STM (Fig. 1a), sometimes larger than $1\mu m^2$, bounded by steps with a step height of about 0.8 nm. The terraces are intrinsically rough, with a peak-to-peak corrugation larger than 0.2 nm. The large roughness is due to the fact that the STM tip probes several layers. The top layer is incomplete and appears as a set of bright dots in the STM images (Fig. 1b and 1c), all of the same size, approximately 0.2 nm in height and 1 nm in width. It is not possible to resolve completely the structure of the various layers probed by the STM tip (Fig.1c). However, all characteristics observed in the

images can be interpreted directly in terms of the bulk structure model proposed by Boudard [16].

The bulk structure of this large unit cell orthorhombic approximant can be described as a set of atomic planes exhibiting local arrangements with either 5-fold or 10-fold symmetry stacked along the p-10f axis. The layer stacking generates cluster units with nearly icosahedral symmetry that closely resemble the cluster units found in the AlPdMn quasicrystal. The long range order with p-10f symmetry is evidenced by the sharp low-energy electron diffraction pattern obtained on this surface (Fig. 1d). The short range order with local 10-fold symmetry is clearly demonstrated by the XPD pattern shown in Fig. 2. The STM data indicate that the surface terminates at a specific set of layers. The incomplete top layer corresponds to the preferential re-growth of decagonal rings of atoms that are part of the 3D cluster units found in the bulk structure of the ξ' phase. Each bright dot in the STM image thus corresponds to a ring of ten Al atoms, this decagonal ring being part of a 3D cluster of the bulk structure [19]. We now describe the morphology of the Pd film formed on this complex surface.

Pd thin film growth.

Figure 3 shows a sequence of 50x50 nm^2 STM images of the surface exposed to 0.7, 3.5 and 7 monolayers (ML) of Pd. The film appears to be rough at all coverage as no flat islands develop on the surface. The film roughness can be quantified by using the root-mean square (RMS) values of the Z-height deduced from the STM images. It increases continuously, from 0.04 nm for the clean surface, to 0.08 nm at 0.7 ML, 0.12 nm at 3.5 ML and 0.26 nm at 7 ML.

Up to 3.5 ML (Fig. 3a-c), the deposited Pd atoms form small particles distributed homogeneously on the terraces. The peak-to-peak height of line profiles taken across these particles is on average equivalent to one to two atoms high at 0.7 ML and two to three atoms high at 3.5 ML. The height of the particles can be larger than the average values given above, up to 1 nm at 3.5 ML. The lateral size of the clusters increases with increasing film thickness, from about 1.5 nm at 0.7 ML to 2 nm at 3.5 ML.

To get a better idea of the morphology of the Pd film at low coverage, we compare in Fig. 4 three STM images of the p-10f surface of the ξ' approximant, either clean (Fig. 4a) or dosed with 0.7 ML of Pd (Fig. 4b) and 0.6 ML of Ag (Fig. 4c). The height histograms deduced from these images are shown in Fig. 4d. The contrast has been set to enhance the part of the surface which is above the bottom layer of the substrate. This corresponds to $Z \geq 0$ in the height histograms of Fig. 4d. For the clean surface (Fig.4a), only the dots corresponding to the decagonal ring of atoms mentioned above can be seen. Because these dots all have the same height, they give rise to a well defined peak in the film height distribution, 0.1 nm above the main substrate peak. In the case of Ag dosed on the same surface (Fig. 4c), a relatively smooth film develops with well defined flat islands that give rise to a well defined peak in the film height distribution, located at approximately 0.2 nm above the substrate. In the case of Pd, we do not observe any flat islands but rather tiny particles covering the substrate layer. The density of these Pd particles in Fig. 4b is rather high compared to the Ag island density in Fig. 4c. The width of the height distribution is not larger for the Pd film than for the Ag film at this coverage, but height distribution profiles are different. The Pd particles do not spread laterally into flat islands contrary to Ag and consequently their film height distribution do not present a well defined peak but rather a

broad featureless distribution. The film morphology keeps the same characteristics at 3.5 ML, although the Pd particles are now slightly larger (Fig. 3c). At 7 ML, it may be more appropriate to describe the Pd particles as mounds. Their shape is now better defined (Fig. 3d). The average peak-to-peak height is about 1 nm and their lateral size is approximately 3 nm. The island size increases with increasing coverage and the island density decreases, indicating growth-induced coalescence of the Pd islands. However, no significant change in the cluster shape is observed with time for a fixed coverage, at least over a period of several hours (see Fig. 3b and 3c), suggesting that no diffusion-induced coalescence (ripening) of the Pd islands takes place. We need to caution that the dimensions and shape of the metal particles or mounds, as well as roughness values given above, can be distorted by the probing tip itself. The exact size and shape of the particles is always smeared out due to the finite size of the tip apex and this effect increases with the tip radius [20]. The diameter of the Pd particles given above can therefore be considered as upper limits of their real diameter.

For the sake of comparison, we perform deposition experiments under the same conditions as for the ξ' approximant on two other substrates : the air-cleaved surface of an HOPG sample and the (111) surface of a Pd single crystal. STM images of these surfaces dosed with 0.7 ML of Pd are shown in Fig. 5. Palladium atoms form clusters on the graphite surface and flat triangular islands on Pd(111), consistent with previous studies of these systems [21-23]. The graphite surface is decorated with 3D clusters having a lateral size of 4 to 5 nm. Their height is between 1 and 2 nm. The linear array of Pd clusters in Fig. 5a suggests that metal particles preferentially nucleate at defect sites on the HOPG surface (lattice point defects, step edges or subsurface defects). Growth of 3D clusters at defect sites

is indeed frequently observed on HOPG substrate [24] but also for metal particles deposited on oxide surfaces [11,12]. Heterogeneous nucleation at defect sites dominates the nucleation process if the density of defects is high enough, such that a diffusing adatom will be trapped by a defect before it can aggregate with other diffusing adatoms to form a stable nucleus.

The nucleation process is different on the Pd(111) surface. The Pd on Pd(111) epitaxial system has been studied in detail by Steltenpohl *et al.* [23]. Analysis of island size distributions and of the temperature dependence of the island density N_{av} provided evidence for the dominant nucleation mechanism. The nucleation event consists of the aggregation of only two diffusing adatoms forming a stable nucleus, so-called homogeneous nucleation with critical island size i=1. In the case of homogeneous nucleation, for complete condensation regime and 2D cluster growth, the island density depends on the flux F according to $N_{av} \sim F^{i/(i+2)} \sim F^{1/3}$ [25,26]. The nuclei will grow further into triangular islands by aggregation of further diffusing adatoms, as observed in Fig. 5c. Multilayer islands are formed already at 0.7 ML coverage, and this is not due to thermodynamic factors but to kinetic limitations. Specifically, multilayer growth arises from an additional energy cost for an adatom to diffuse down a step (the so-called step-edge barrier) limiting interlayer transport and thus promoting island nucleation on top of pre-existing islands [27].

A more detailed study would be necessary to get some insight into the nucleation mechanism of the Pd particles on the ξ' approximant surface. This would require an analysis of the flux dependence of the island density and of the island size distribution at lower coverage than the one used in the present study [28]. This has never been done on quasicrystalline and related substrates, except for Ag deposited on the 5-fold surface of $Al_{72}Pd_{19.5}Mn_{8.5}$ icosahedral QC [29]. In this latter case, the island density was relatively high

and did not depend on the flux. Together with monomodal island size distribution, these observations pointed to heterogeneous nucleation involving the irreversible capture of diffusing adatoms at specific quasilattice "trap" sites. In the absence of comparable data, we cannot conclude that a similar nucleation mechanism occurs here. We simply note that local surface structure and chemistry of the ξ' approximant closely resembles the 5-fold AlPdMn QC surface. The density of Pd particles is also high on the ξ' approximant surface, and much higher than on the graphite or the Pd(111) surfaces.

We mentioned earlier that some oxygen contamination occurred during the Pd deposition. In other metal film growth systems, oxygen is generally observed to act as a surfactant—an agent that smoothens film morphology. This is true, for instance, in Pt/Pt(111) [30]; in Ag/Ag(100) [31,32]; in Pd/Pd(111) [22]; and in Fe/Cu [33]. Hence, we expect that the oxygen contamination in our experiments did not give rise to the 3D growth of the Pd, but may have dampened it somewhat. Additional experiments are needed to see if more drastic 3D growth would have occurred on the p-10f surface of the ξ' approximant in the absence of oxygen.

We now discuss the origin of the different growth modes observed for the various substrates. Traditional macroscopic explanation of the growth modes in the thermodynamic regime relies on a balance involving the surface and adsorbate free energies (γ_s and γ_a) and the interfacial energy γ^* [34]. Specifically, smooth layer by layer growth (Frank–van der Merwe type) is favored if $\gamma_a + \gamma^* \leq \gamma_s$, whereas rough 3D growth (Volmer–Weber type) occurs if $\gamma_a + \gamma^* > \gamma_s$. An alternative formulation in terms of local bond energies (which determine all three energetic quantities) and interfacial strain (which can increase γ^*) maybe

more appropriate given the small (nanoscale) lateral size of 3D islands, but we keep using

the usual thermodynamic language in the following. The surface energy of transition metals

is usually high and the most recent calculation gives γ_{Pd} between 1.9 and 2.2 J/m^2 depending

on the surface orientation [35]. The surface energy of graphite is very low ($\gamma_{HOPG} < 0.1$ J/m^2)

[36] and thus $\gamma_{Pd} + \gamma^* > \gamma_{HOPG}$, in agreement with observation of 3D clusters formation. Based

on a previous study of Ag thin film growth on the ξ' approximant [18], $\gamma_{\xi'}$ should be higher

than γ_{Ag} (1.2 J/m^2) but presumably lower than γ_{Pd}. The rough structure of the Pd film then

results from $\gamma_{Pd} + \gamma^* > \gamma_{\xi'}$, i.e. from thermodynamic effects. Here we assume that the

interfacial energy does not play a significant role in the case of the ξ' substrate. This

assumption is motivated by the comparison of the different growth modes that have been

observed for Sb, Bi and Ag thin films deposited on similar substrate and under similar

experimental conditions[18]. The interfacial energy naturally depends on the misfit between

the adsorbate and the substrate. The misfit is not very important in these cases because the

interatomic distances of the various substrates and adsorbates are all close to about 0.3 nm.

No correlation between the observed growth modes and misfit was observed. Instead, the

growth mode, either smooth or 3D, appeared to be mainly influence by surface energy terms

suggesting that the interfacial energy term is of second order. In the case of Pd on graphite,

the lattice mismatch is more important and the interfacial energy can probably not be

considered as of second order. Interfacial energy indeed increases significantly with misfit

[37]. However the difference between surface energies of Pd and graphite is so large that

even a large interfacial energy should not change the balance $\gamma_{Pd} + \gamma^* > \gamma_{HOPG}$.

Finally, in conditions close to equilibrium, one should expect smooth layer-by-layer growth for Pd on Pd(111), if only thermodynamic effects were considered. However, metal film growth is often dominated by kinetic effects at room temperature and below [27,28]. The observed multilayer growth is a non-equilibrium structure resulting from the growth kinetics – controlled by the step edge barrier.

For a 7 ML thick film deposited on the pseudo 10-fold ξ' surface, we tried to record the reflection high-energy electron diffraction (RHEED) pattern without success. The sample was heated progressively up to 920 K while monitoring the RHEED, but again no diffraction spots could be observed. This suggests that the film has an amorphous structure or that the coherent crystalline domains are too small to produce a diffraction pattern. The sample was cooled down to room temperature after the desired annealing temperature had been reached for further STM analysis. Figure 6 shows 100x100 nm^2 STM images of the 7 ML thick film obtained before (Fig. 6a) and after annealing at 720 K (Fig. 6b) and 920 K (Fig. 6c). The height histograms deduced from these images (Fig. 7) indicates that some diffusion-induced ripening of the Pd islands takes place upon annealing. For example, the full-width at half-maximum (FWHM) of the height histograms can be used to derive a trend in the film smoothening upon annealing. It decreases from 0.48 nm at room temperature to 0.36 nm after annealing at 720 K and 0.29 nm after annealing at 920 K. However it is clear from Fig. 6 that the clusters still exist even after heating up to 920 K and do not smoothen completely into an atomically flat film with terraces and steps.

Electronic structure.

STS spectra were recorded during the constant current topographic image acquisition by stopping the scan at specific points, interrupting the feedback loop, and measuring the tunnelling current (I) as a function of the bias voltage (V). Three signal-average I(V) curves measured at various coverages are shown in Fig. 8. In the case of the 0.7 ML thick Pd film, the STS spectra were recorded on the Pd islands. The plateau observed in the spectra at 0 and 0.7 ML disappears at 3.5 ML coverage. The plateau is actually not completely flat but the slope of the I(V) curve in the region around the zero bias voltage ($\pm$ 0.4 eV around the Fermi level E_F) is significantly lower than further away from E_F. This feature persists at 0.7 ML but disappears at higher coverage. This flat region on the I(V) curves could be reminiscent of the minimum of the electronic density of states (pseudogap) which has been observed in the ξ' approximant as well as in the corresponding icosahedral phase [38-40].

The UPS valence band of the Pd(111) surface is shown in Fig. 9, together with the XPS valence band of the ξ' approximant. The main peak in the valence band of the ξ' approximant is due to the Pd *4d* states [41]. It is shifted toward higher binding energies with respect to pure Pd by more than 2 eV. In the metal, the *4d* states are located much closer to the Fermi level, producing a high density of states at E_F and a good metallic character. The shift of the Pd *4d* states is correlated with a similar shift of the Pd *3d* core levels toward higher binding energies. These observations can be explained by hybridization between Al *sp* states and the Pd *d* states, leading to an apparent *d* band filling [42]. This is well known in Al-transition metal alloys and has been observed previously in the icosahedral AlPdMn QC phase as well as in several Al-Pd binary alloys [41]. Figure 10 shows Pd *3d* core levels recorded at various emission angles after the surface had been covered by 3.5 ML of Pd. It is obvious from these spectra that the Pd *3d* levels are shifted toward lower binding energies

(BEs) as the emission angle increases. The BE of the Pd $3d_{5/2}$ is plotted as a function of the emission angle in the inset of Fig. 10. It decreases from 336.4 eV at normal emission to 336.0 eV for an emission angle of 70°. Its value in the pure metal is 335 eV, whereas it is 337.5 eV in the pure ξ' phase. This means that the BEs of the Pd $3d$ core levels are approaching the value of the pure metal when the surface sensitivity of the signal is increased. We can hypothesize that a similar shift of the Pd $4d$ band occurs in the valence band, i.e. that the Pd $4d$ states are progressively shifted toward the Fermi level. Valence and core level shifts in Al-Pd alloys are indeed correlated [43]. If it occurs, the Pd $4d$ states should progressively smear out the pseudogap feature in the density of states at E_F. For a thick enough film, it should eventually recover the position of the pure Pd metal. Therefore with increasing film thickness, the surface electronic structure should change from that of a poor metal (with a pseudogap at E_F) characteristic of the ξ' approximant, to that of a good metal like Pd. The STS and XPS data presented above suggest that this transition already occurred by a coverage of about 3.5 ML.

Conclusion

In summary, we have shown that Pd thin films grown on the p-10f of the ξ' approximant are rough. Deposited Pd atoms form small particles rather than flat islands like on the Pd(111) surface. The size of the Pd particles increases with increasing film thickness, up to 3 nm at 7 ML coverage. These metal particles are rather stable and the rough aspect of the film persists even after a short annealing to 920 K. Spectroscopy data are consistent with a reduced density of states at E_F on the clean surface of the ξ' approximant. With increasing film thickness, the surface electronic structure changes from that of a poor metal(with a

pseudogap at E_F) to that of a good metal like Pd, and this transition already occurs by 3.5 ML.

We mentioned in the Introduction the high catalytic activity of the leached AlPdMn QC powder. In this study, we used a substrate that is very close, both structurally and chemically, to this QC phase. We observed that Pd deposited on this substrate forms small particles rather than a smooth continuous film. The 3D growth most likely results from the low surface energy of the substrate as compared to γ_{Pd}. The density of Pd particles on the ξ' surface is rather high. It follows that the surface area of the active catalyst is large, consistent with a high catalytic activity.

In the AlCuFe quasicrystalline system, the activity of the leached QC powders was shown to increase with temperature up to the experimental limit of 570 K [8]. Extrapolating to the AlPdMn system, this result seems consistent with our observation that the Pd particles are quite stable upon annealing. Indeed, if the film were to smoothen upon annealing, the surface area and thus the catalytic activity would decrease drastically.

We note that rough 3D growth on this substrate may also be expected for other transition metal thin films (like Pt, Cu, Ru, Co, V, Rh...) as the surface energies of these elements are at least as high as γ_{Pd} (≥ 2 J/m^2) [35]. Also, rough 3D growth of Ag thin film on the 5-fold surface of the $Al_{72}Pd_{19.5}Mn_{8.5}$ icosahedral QC was reported previously, suggesting that the surface energy of the 5-fold QC surface is lower than γ_{Ag} (1.2 J/m^2) [29]. It is therefore reasonable to expect 3D growth as well for transition metals thin films grown on the quasicrystalline surface. This substrate may actually be more suitable for further studies, especially because the clean surface exhibits atomically flat terraces (contrary to the ξ'

surface) [44-46]. This would facilitate a detailed analysis of the nucleation mechanism, which requires an analysis of the island size distribution and island density at low coverage.

These conclusions assume that the particles formed by metal deposition on the clean substrate can be compared to the metal particles formed by leaching treatment of the quasicrystalline powders. This is not straightforward at all and this first attempt to better understand the catalytic properties of quasicrystals clearly deserves further experimental work. From an analysis of the x-ray diffraction peaks of AlCuFe QC powders, the size of Cu and Cu oxide particles formed upon leaching in NaOH solution was estimated to be ~15 nm. The same powder leached in HCl solution presented much larger Cu particles with μm scale and had a much lower activity. The size of the metal particles produced by the leaching treatment has therefore a strong influence on the catalytic activity, either because larger particles will present a lower surface area of the active metal or because the reaction rate depends on the particle size. Clearly, the Pd particles formed on the ξ' surface in UHV experiments are in the nanometer range, which is the correct order of magnitude relevant for catalysis. More detailed information is needed, however, on the exact shape of the metal particles formed during the leaching treatment. For example, atomic force microscopy (AFM) experiments on polygrained QC sintered samples after leaching might be helpful to bridge the gap between the model systems prepared in UHV environment and the "real world" catalyst.

Acknowledgment

References

[1]   D. Shechtman, I. Blech, D. Gratias, J.W. Cahn, Phys. Rev. Lett. 53 (1984) 1951.

[2]   A.P. Tsai, MRS Bull. 22 (1997) 43.

[3]   A.P. Tsai, in Z.M. Stadnik (Editor), Physical Properties of Quasicrystals, Springer, Berlin, 1999, p. 5.

[4]   Z.M. Stadnik, Physical Properties of Quasicrystals., Springer, 1999.

[5]   J.-M. Dubois, J. Phys.: Condens. Matter 13 (2001) 7753.

[6]   T. Masumoto, A. Inoue, YKK Corporation, Honda Giken Kogyo Kabushiki Kaisha, in, European Patent No. 94115137.5, 1994.

[7]   M. Yoshimura, A.-p. Tsai, Y. Takahashi, in Eur. Pat. Appl., (Japan as Represented by Director General of Ministry of Education, Culture, Sports, Science and Technology N.R.I. for Metals, Japan)., Ep, 2001, p. 8 pp.

[8]   A.P. Tsai, M. Yoshimura, Appl. Catal., A 214 (2001) 237.

[9]   M. Yoshimura, A.P. Tsai, J. Alloys Compd. 342 (2002) 451.

[10]   G.A. Somorjai, Introduction to Surface Chemistry and Catalysis, Wiley, New York, 1994.

[11]   C.T. Campbell, Surf. Sci. Rep. 27 (1997) 1.

[12]   C.R. Henry, Surf. Sci. Rep. 31 (1998) 235.

[13]   M. Bäumer, H.-J. Freund, Prog. Surf. Science 61 (1999) 127.

[14] M. Valden, X. Lai, D.W. Goodman, Science 281 (1998) 1647.

[15] C. Janot, Quasicrystals: A Primer, Second Edition, Oxford Science Publications,

Oxford, 1995.

[16] M. Boudard, H. Klein, M. de Boissieu, M. Audier, Philos. Mag. A 74 (1996) 939.

[17] A. Jablonski, C.J. Powell, Surf. Sci. Rep. 47 (2002) 33.

[18] V. Fournee, A.R. Ross, T.A. Lograsso, J.W. Evans, P.A. Thiel, Surf. Science (2003)

submitted.

[19] V. Fournee, T. Cai, A.R. Ross, T.A. Lograsso, J.W. Anderegg, C. Dong, M. Kramer,

I.R. Fisher, P.C. Canfield, P.A. Thiel, Phys. Rev. B 66 (2002) 165423.

[20] S. Stempel, M. Bäumer, H.-J. Freund, Surf. Science 402-404 (1998) 424.

[21] A. Piednoir, E. Perrot, S. Granjeaud, A. Humbert, C. Chapon, C.R. Henry, Surf.

Science 391 (1997) 19.

[22] A. Steltenpohl, N. Memmel, Surf. Science 402-404 (1998) 277.

[23] A. Steltenpohl, N. Memmel, Surf. Science 454-456 (2000) 558.

[24] C. Bréchignac, P. Cahuzac, F. Carlier, C. Colliex, M. de Frutos, M. Kebaïli, J. Le

Roux, A. Masson, B. Yoon, Eur. Phys. J. D 16 (2001) 265.

[25] N.C. Bartelt, J.W. Evans, Phys. Rev. B 54 (1996) R17359.

[26] J.A. Venables, Physica A 239 (1997) 35.

[27] P.A. Thiel, J.W. Evans, J. Physical Chemistry 104 (2000) 1663.

[28] J.A. Venables, Introduction to Surface and Thin Film Processes, Cambridge

University Press, 2001.

[29] V. Fournee, T. Cai, A.R. Ross, T.A. Lograsso, J.W. Evans, P.A. Thiel, Phys. Rev. B:

Brief Reports. 67 (2003) 033406.

[30]   S. Esch, M. Hohage, T. Michely, G. Comsa, Phys. Rev. Lett. 72 (1994) 518.

[31]   A.R. Layson, P.A. Thiel, Surf. Science 472 (2001) L151.

[32]   A.R. Layson, J.W. Evans, V. Fournée, P.A. Thiel, J. Chem. Phys. accepted (2003).

[33]   D.A. Steigerwald, I. Jacobs, J.W.F. Egelhoff, Surf. Science 202 (1988) 472.

[34]   E. Bauer, J.H. van der Merwe, Phys. Rev. B 33 (1986) 3657.

[35]   L. Vitos, A.V. Ruban, H.L. Skriver, J. Kollar, Surf. Science 411 (1998) 186.

[36]   G. Kern, J. Hafner, Phys. Rev. B 58 (1998) 13167.

[37]   J.H.v.d. Merwe, Prog. Surf. Science 67 (2001) 365 .

[38]   D. Naumovic, P. Aebi, M. Bovet, F. Clerc, C. Koitzsch, L. Schlapbach, C. Beeli, K. Kunze, T.A. Lograsso, A.R. Ross, D.W. Delaney, in Eighth International Conference on Quasicrystals, Journal of Non-crystalline Solids, Bangalore, India, 2002, p. to be published.

[39]   D. Naumovic, P. Aebi, L. Schlapbach, C. Beeli, T.A. Lograsso, D.W. Delaney, Phys. Rev. B 60 (1999) R16330.

[40]   G. Neuhold, S.R. Barman, K. Horn, W. Theis, P. Ebert, K. Urban, Phys. Rev. B 58 (1998) 734.

[41]   V. Fournée, E. Belin-Ferré, P. Pêcheur, J. Tobola, Z. Dankhazi, A. Sadoc, H. Müller, J. Phys.: Condens. Matter 14 (2002) 87.

[42]   J.C. Fuggle, E. Kaellne, L.M. Watson, D.J. Fabian, Phys. Rev. B 16 (1977) 750.

[43]   J.A. Rodriguez, Surf. Sci. Rep. 24 (1996) 223.

[44]   Z. Shen, C.R. Stoldt, C.J. Jenks, T.A. Lograsso, P.A. Thiel, Phys. Rev. B 60 (1999) 14688.

[45]   J. Ledieu, R. McGrath, R.D. Diehl, T.A. Lograsso, D.W. Delaney, Z. Papadopolos,

G. Kasner, Surf. Sci. Lett. 492 (2001) L729.

[46]   Z. Papadopolos, G. Kasner, J. Ledieu, E.J. Cox, N.V. Richardson, Q. Chen, R.D.

Diehl, T.A. Lograsso, A.R. Ross, R. McGrath, Phys. Rev. B 66 (2002) 184207.

Figure Captions

Figure 1. STM images (a): 700x700 nm^2, (b): 100x100 nm^2, (b): 33x33 nm^2 of the clean p-10f surface of the ξ' approximant. (d) LEED pattern at 105 eV, obtained from a similar sample extracted from the same ingot in the Ames Laboratory.

Figure 2. Stereographic projection of the XPD image of the Pd 3d emission from the clean p-10f surface of the ξ' approximant. The image has been modified so as to enhance both peak position and the pseudo 10-fold symmetry. The region of 0-360° azimuthal angle and 0-70° in polar angle is shown in a liner gray scale. The outer circle represents the directions corresponding to the 90° polar angle.

Figure 3. (a)-(d) 50x50 nm^2 STM images of Pd deposited on the p-10f surface of the ξ' approximant at 0.7 (a), 3.5 (b, c) and 7 ML (d). The image in (c) was recorded 8 hours after the image in (b).

Figure 4. (a)-(c) 100x100 nm^2 STM images of the p-10f surface of the ξ' approximant, before deposition (a) and after deposition of 0.7 ML of Pd (b) and 0.6 ML of Ag (c). Height histograms of the STM images a (plain line), b (dashed-dotted line) and c (dotted line). The contrast of the STM images (a)-(c) has been set to enhance the part of the surface which is above the bottom layer of the substrate (Z>0).

Figure 5. STM images (a): 300x300 nm^2, (b): 100x100 nm^2 of the HOPG surface dosed

with 0.7 ML of Pd. (c) 100x100 nm^2 STM images of the Pd(111) dosed with 0.7

ML of Pd.

Figure 6. 3D view of 100x100 nm2 STM images of the p-10f surface of the ξ' approximant

dosed with 7 ML of Pd, at room temperature (a) and after heating up to 720 K (b)

and 920 K (c).

Figure 7. Height histograms deduced from the STM images of Fig. 6.

Figure 8. Tunneling spectra obtained on the ξ' surface at various coverage.

Figure 9. XPS valence band of the ξ' surface (full line) and UPS valence band of the

Pd(111) surface (dotted line).

Figure 10. Polar scan of the Pd $3d$ XPS core level lines measured on the p-10f surface of the

ξ' approximant dosed with 3.5 ML of Pd. The emission angles are mentioned in

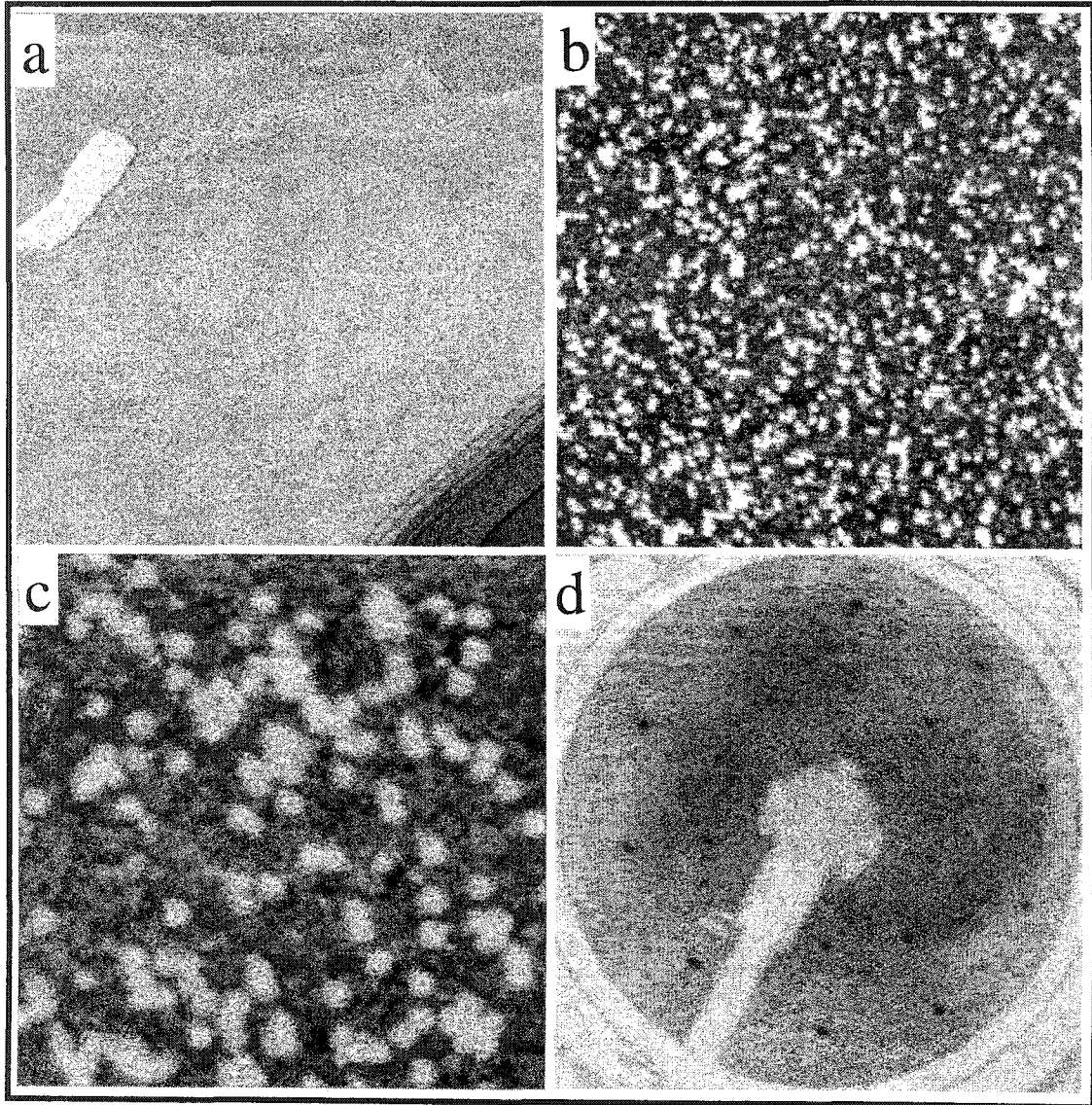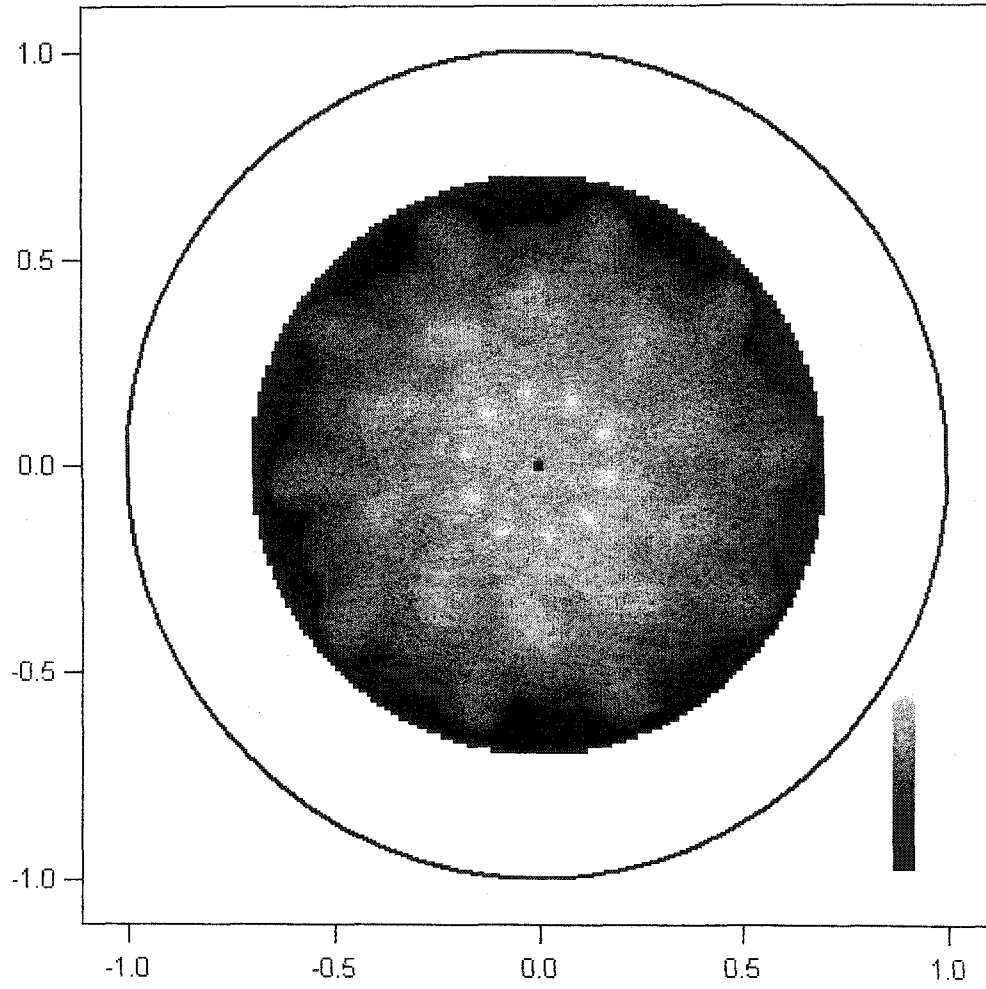the graph. The insert shows the variations of the Pd $3d_{5/2}$ binding energy as a

function of the emission angle.

Figure 1

Figure 2

Figure 3

Figure 4

Figure 5
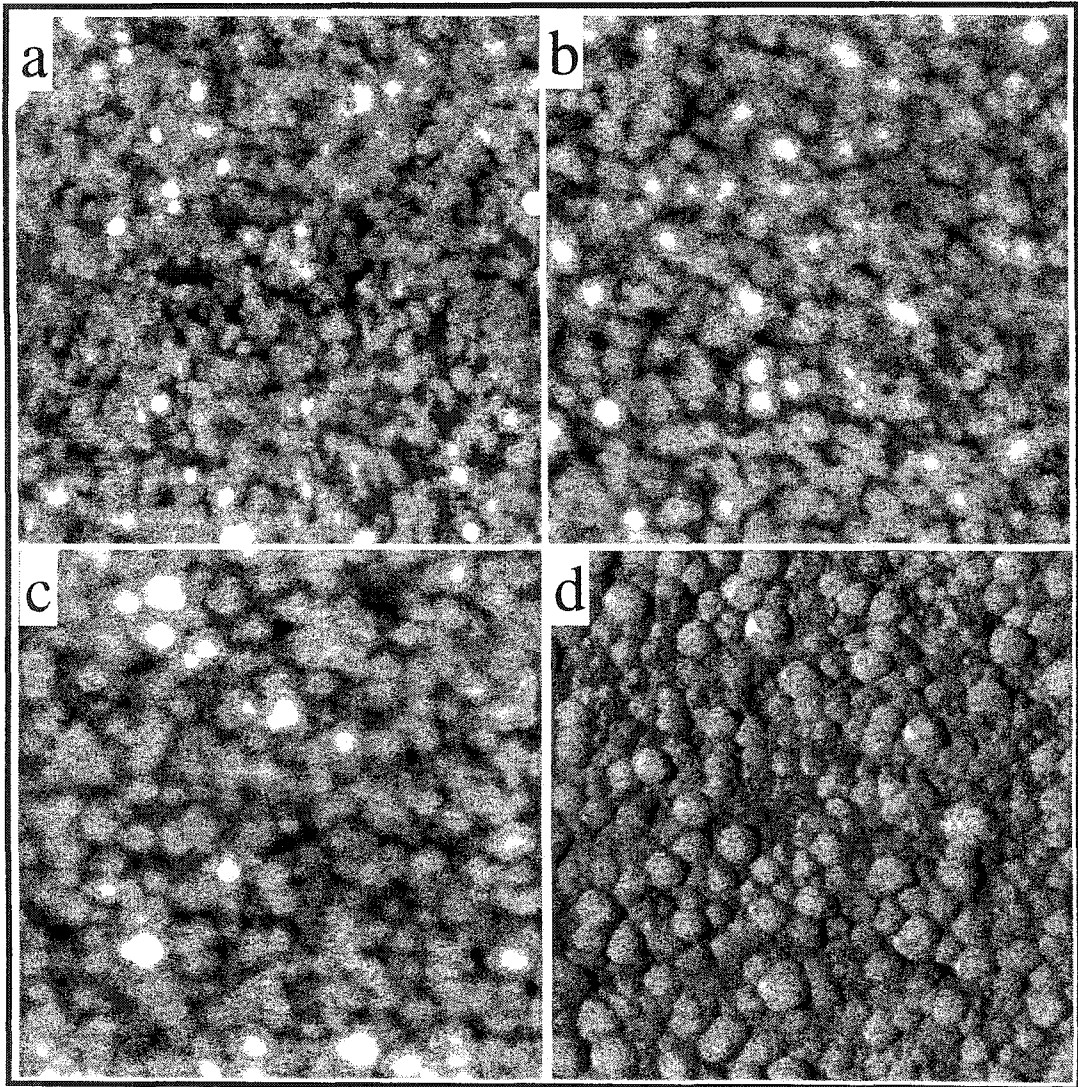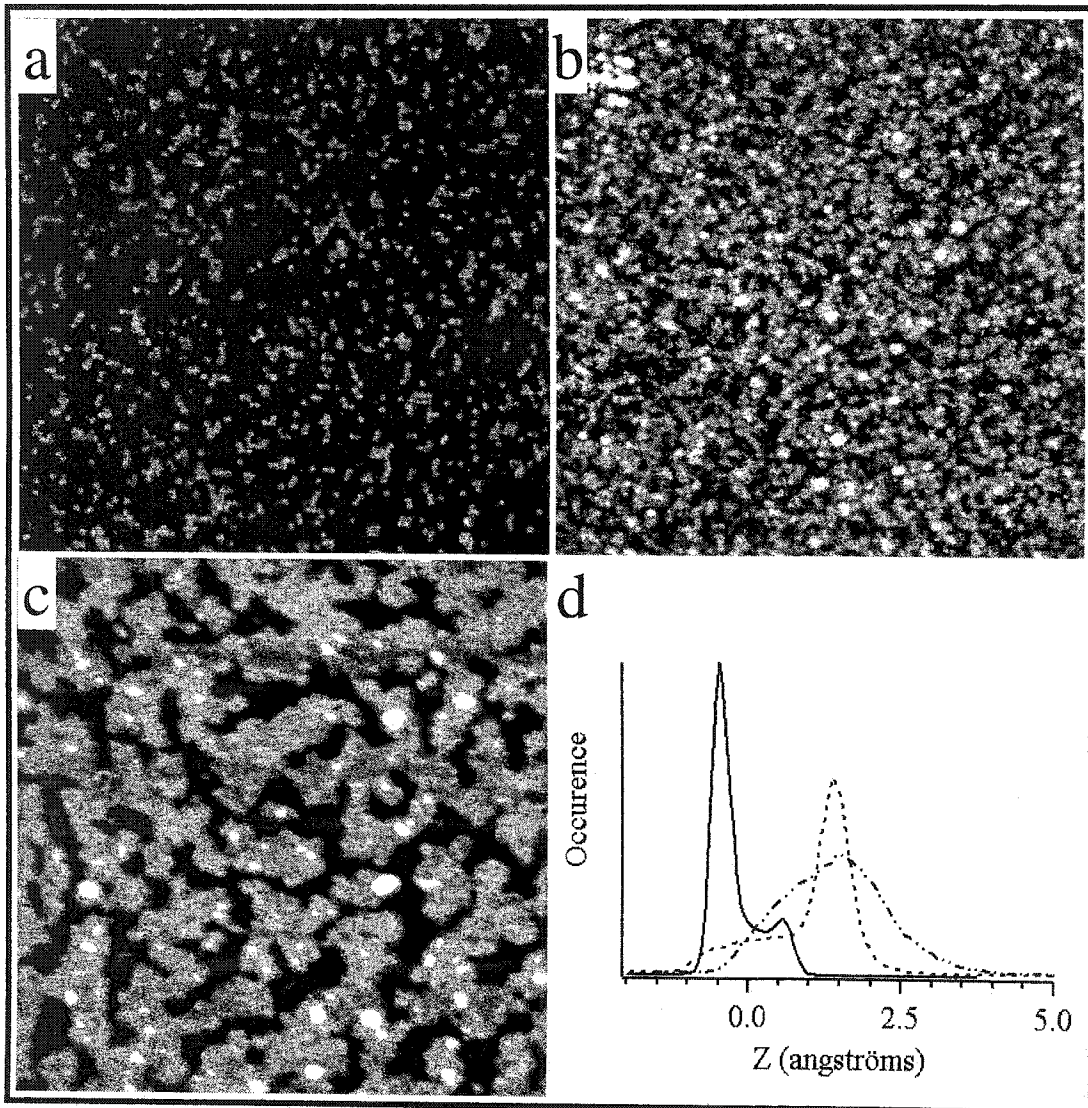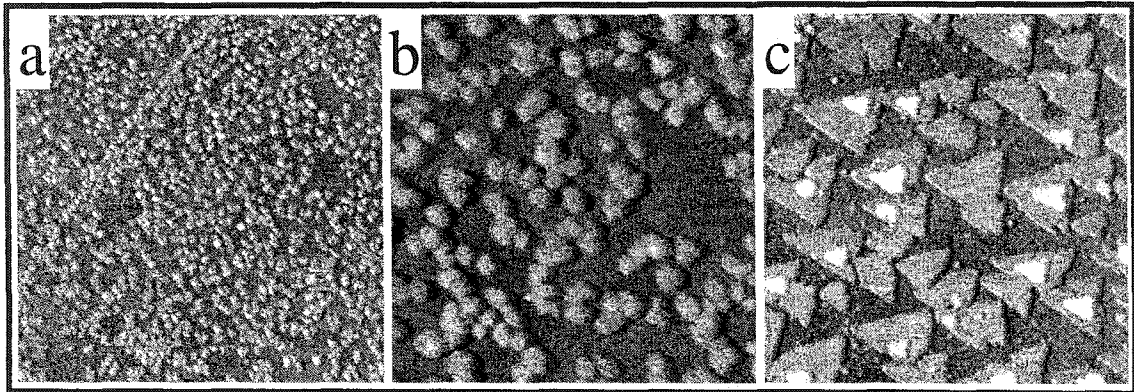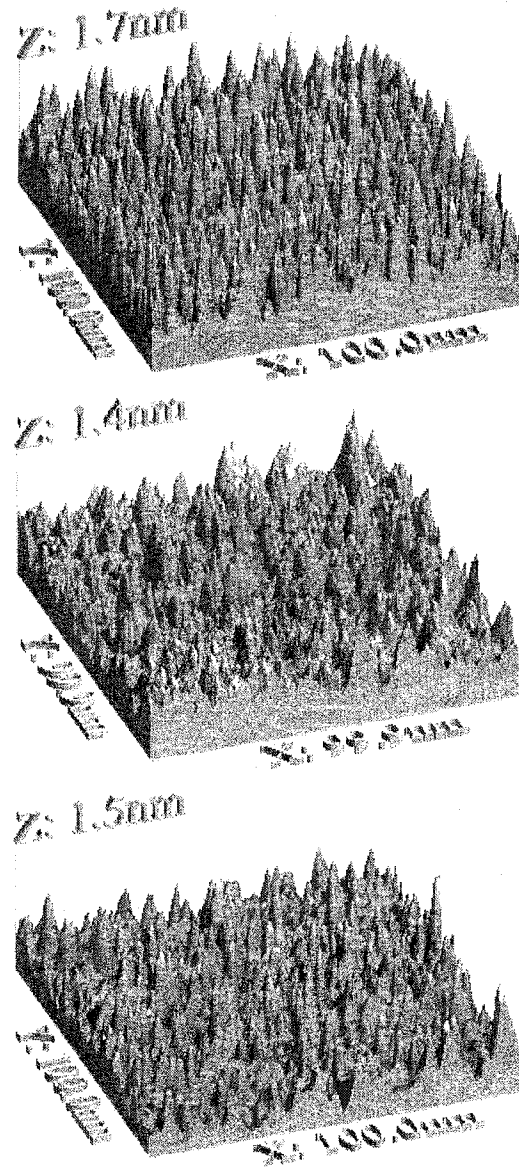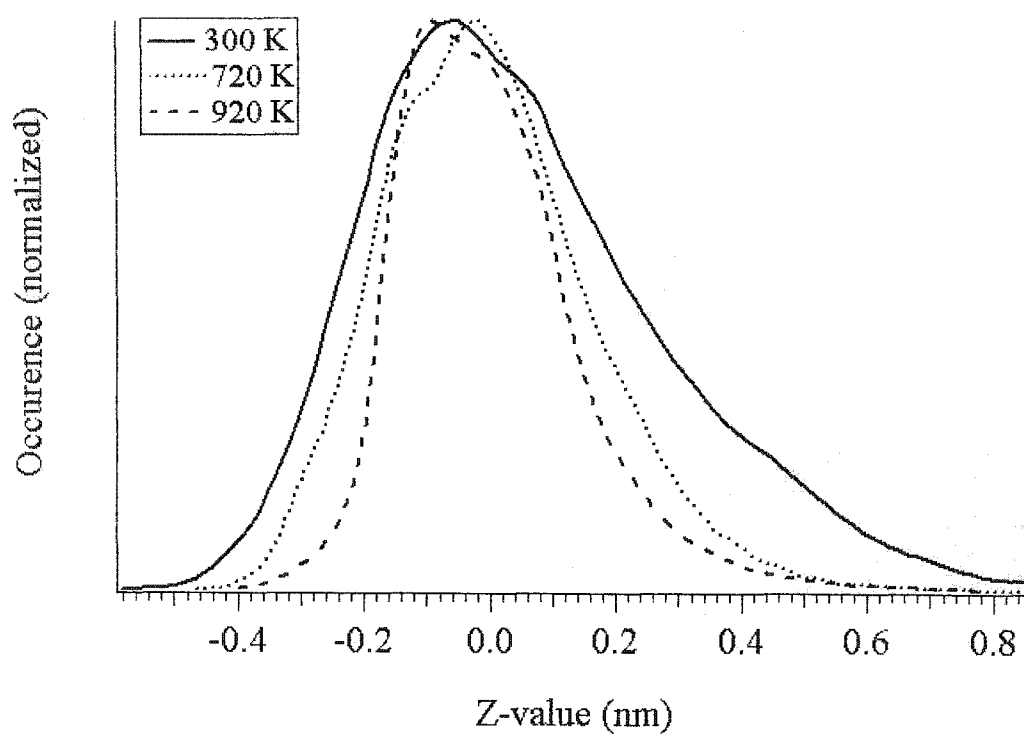
Figure 6

Figure 7
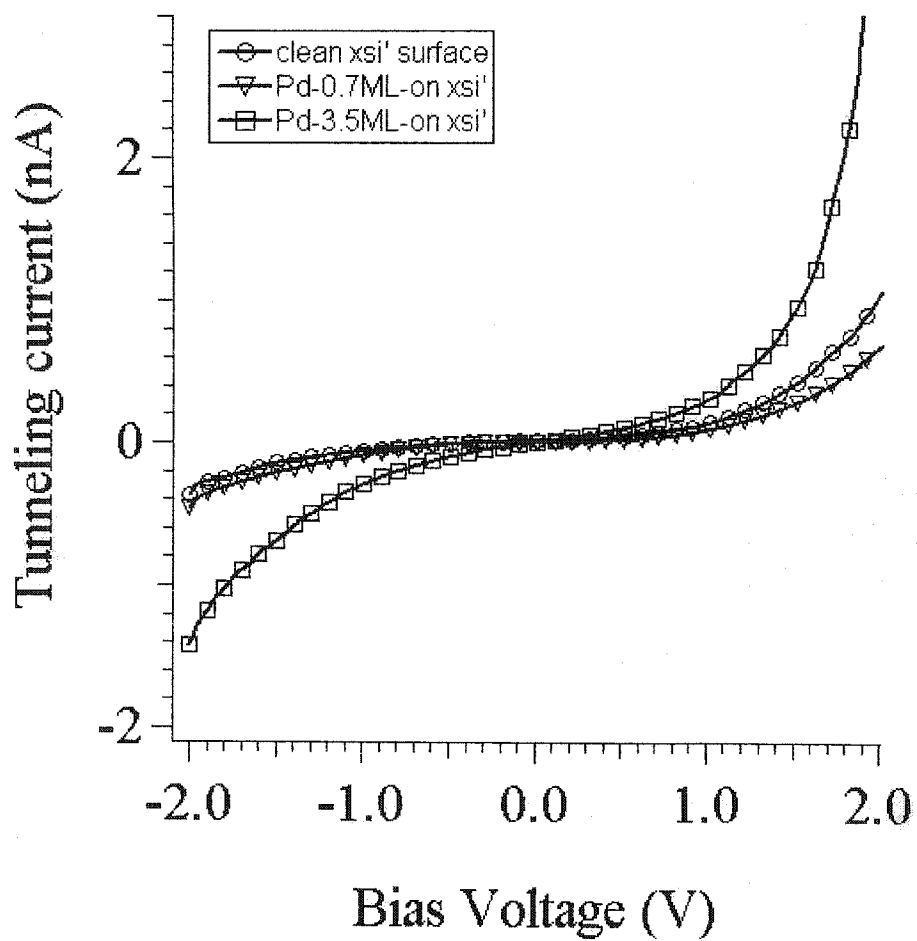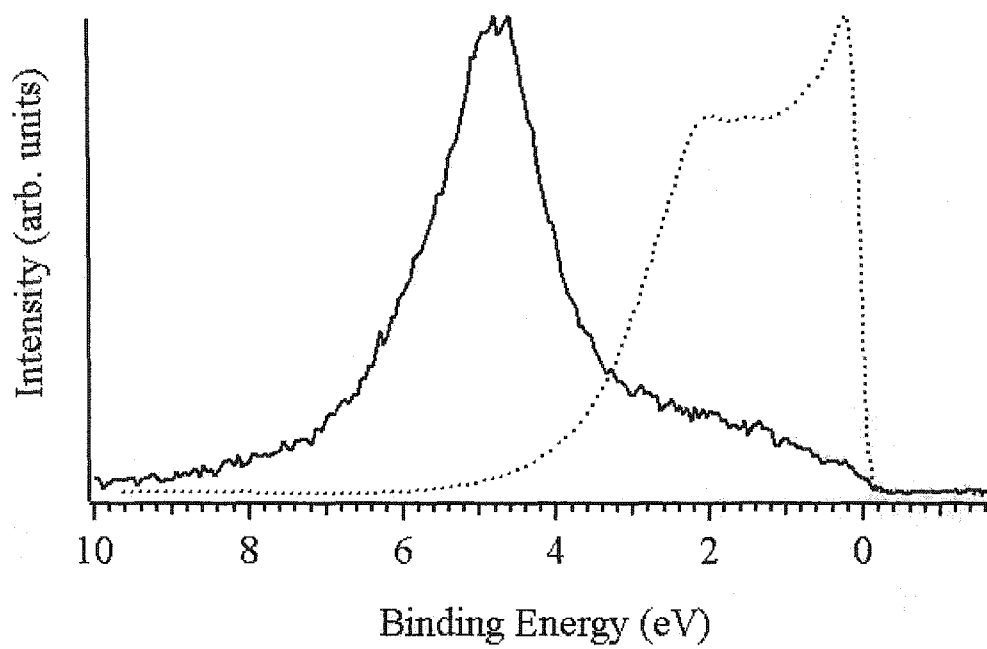
Figure 8

Figure 9
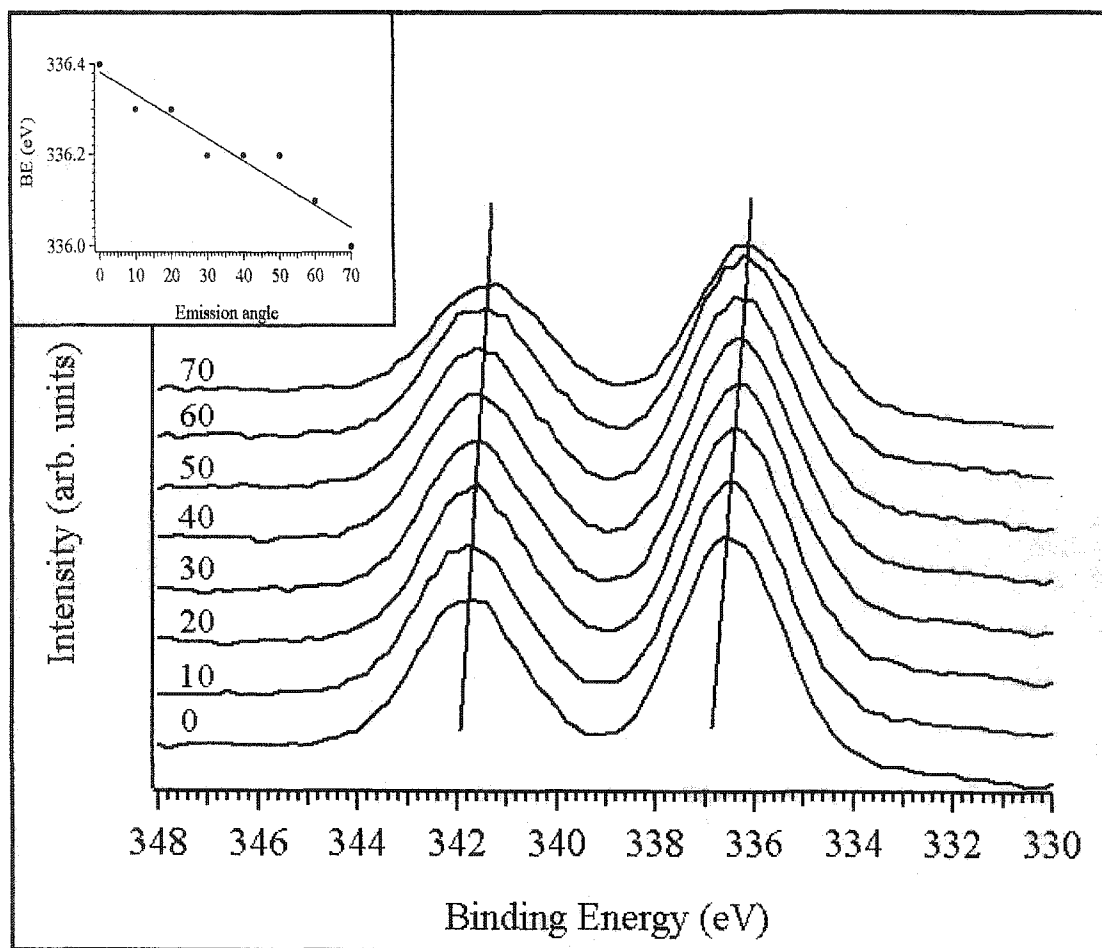
Figure 10

APPENDIX B. DATA COLLECTION RECORD

Table Captions:

1. Laser-vaporization experiments done at Argonne National Laboratory, Argonne, IL.
2. Photoemission and RHEED experiments done at the National Institute for Materials Science, Tsukaba, Ibaraki, Japan.
3. Scanning tunneling microscopy experiments done at Ames Laboratory, Ames, IA.

Date	File Location	Panels Collected	Comments
2/4/99	File location is ANL	Survey 10-150	Old rod, dual inlet source, Lambda ArF, Al calibration
2/9/99	File location is ANL	10,30,120	Old rod, dual inlet source, Lambda ArF, Al calibration, added O_2 to He looking for magic- none seen
3/31/99	File location is ANL	120	Old rod, High temp source, Lambda ArF and F_2, Al calibration, temperature ramp looking for magic- none seen
4/2/99	File location is ANL	10-240	Old rod, 21.1mm flat plate on standard block survey, Lambda ArF, Al calibration
6/2/99	File location is ANL	120-150	Old rod, dual inlet source, Questek KrCl, Al calibration, no magic
9/8/99	File location is ANL	40-120	Old rod, dual inlet source, Questek XeCl, Al calibration, magic found
9/10/99	File location is ANL	40-120	Old rod, High Temp source, Questek KrCl, Al calibration
3/8/00	File location is ANL	45-150	Newer natural abundance rod, has a cheesy look, YAG blasted through it after only one day, Lambda ArF
3/13/00	File location is ANL	Various	Old rod, 21.1mm flat plate on collection block, Lambda ArF, focused and unfocused, study oil in chamber 4

Table 1

Date	File Location	Panels Collected	Comments
3/14/00	File location is ANL	15-60 linear	Old rod, 21.1mm flat plate, Lambda KrF, focused, survey, Al calibration
7/12/00	File on Data Backup Disk Hardcopies in Argonne Binder	20-70	Old rod, flat plate, Lambda ArF, Al calibration, unfocused, every 10µs
7/14/00	File on Data Backup Disk Hardcopies in Argonne Binder	20-70	New 106Pd rod, flat plate, Lambda ArF, Al calibration, unfocused, every 10µs
8/7/00	File location is ANL	60-105	New 106Pd rod, flat plate, Lambda ArF, Al calibration, unfocused, every 10µs, shut down due to rod drive problems
8/9/00	File location is ANL	Various	Old rod, flat plate, Lambda ArF, double lens focusing, nozzle plugging problems
8/10/00	File location is ANL	Various	Old rod, flat plate, Lambda KrF (probe), Questek XeCl (pump), attempted two color experiments looking for magic
8/15/00	File location is ANL	Various	Old rod, flat plate, Lambda ArF (probe), Questek XeCl (pump), attempted two color experiments looking for magic
8/16/00	File location is ANL	Various	Old rod, flat plate, Lambda ArF (probe), Questek XeCl (pump), attempted two color experiments looking for magic

Table 1 (Continued)

Date	File Location	Panels Collected	Comments
8/18/00	File location is ANL	Various	Old rod, flat plate, Lambda ArF (probe), Questek XeCl (pump), attempted two color experiments looking for magic
8/23/00	File on Data Backup Disk Hardcopies in Argonne Binder	20-70	106Pd rod, flat plate. Lambda F_2, Al calibration, unfocused
10/17/00	File on Data Backup Disk Hardcopies in Argonne Binder	30-70	106Pd rod, flat plate, Lambda ArF, focused ArF (MPI) shows magic, unfocused ArF (SPI) does not show magic.
10/18/00	File on Data Backup Disk Hardcopies in Argonne Binder	30-150	106Pd rod, flat plate, Questek XeCl, (MPI) shows magic

Table 1 (Continued)

Date	Sample	File Location	Experimental Notes and Comments
9/17/02	i-AlCuFe (ARR-4-8-a)	XPS: ACF_0917_	Sample mounted and inserted into chamber. XPS done.
9/18/02	i-AlCuFe (ARR-4-8-a)	RHEED: ACFx_spt1	RHEED done in-situ with sputter, development of crystalline phase during sputter.
9/18/02	i-AlCuFe (ARR-4-8-a)	RHEED: ACFx_spt2	Sputter/anneal cycles to clean sample
9/19/02	i-AlCuFe (ARR-4-8-a)	XPS: ACF_0918_	Sputtering with sputter gun in XPS chamber. This gun is too low energy to clean the sample.
9/19/02	i-AlCuFe (ARR-4-8-a)		Transfer sample back to RHEED chamber. Sputter/anneal cycles.
9/20/02	i-AlCuFe (ARR-4-8-a)	XPS: ACF_0919_	XPS shows no improvement. Continue sputter/anneal cycles.
9/22/02	i-AlCuFe (ARR-4-8-a)		Getting large pressure increases during annealing. Outgas sample stages overnight.
9/24/02	i-AlCuFe (ARR-4-8-a)		Continue sputter/anneal
9/25/02	i-AlCuFe (ARR-4-8-a)	XPS: ACF_0925_	Sample looks clean, STM surface is very rough
9/26/02	i-AlCuFe (ARR-4-8-a)	XPS: ACF_0926_ STM: 092602 folder	STM surface still very rough. Visible discoloration on sample surface
9/27/02	i-AlCuFe (ARR-4-8-a)	XPS: ACF_0927_ UPS: ACF_0927_	Trying out the UPS

Table 2

Date	Sample	File Location	Experimental Notes and Comments
9/28/02	i-AlCuFe (ARR-4-8-a)	RHEED: ACF_92802_angle	Measuring angles between different RHEED patterns of sputtered surface.
9/28/02			Chamber accidentally vented! Bake out 24hrs.
10/1/02	i-AlCuFe (ARR-4-8-a) i-AlPdMn (ARR-4-21-4.1)		Insert AlPdMn sample into chamber. Begin sputter/anneal cycles on this sample.
10/2/02	i-AlCuFe (ARR-4-8-a) i-AlPdMn (ARR-4-21-4.1)		Sputtering samples in RHEED chamber and annealing in XPS and RHEED chamber, so we can anneal both samples at once.
10/4/02			Take sputter gun apart to fix short. Vacuum break not required.
10/5/02	i-AlCuFe (ARR-4-8-a)	RHEED: ACF_100502_angle	More angle measurements of sputtered surface patterns
10/8/02	i-AlCuFe (ARR-4-8-a)	XPD: ACF_1008_	Begin XPD to run Cu2p
10/9/02	i-AlCuFe (ARR-4-8-a)		Break vacuum to retrieve sample that have been dropped.
10/11/02	i-AlCuFe (ARR-4-8-a) ξ'-AlPdMn (from V. Fournee)		Inserted ξ'-AlPdMn and began sputter/anneal of both samples.
10/14/02	ξ'-AlPdMn (from V. Fournee)	STM: 101402 folder XPD: APM_1014_	STM looks good. Surface bumpy, but good size terraces. Begin XPD on the Pd3d

Table 2 (Continued)

Date	Sample	File Location	Experimental Notes and Comments
10/16/02	ξ'-AlPdMn (from V. Fournee)	STM: 101602 folder	~1 ML Dose of Pd on surface ~5 ML total dose of Pd on surface. STS also collected.
10/17/02	ξ'-AlPdMn (from V. Fournee)	STM: 101702 folder XPS: APM_polar	Experiment continued 8hrs later. Surface appears unchanged. Used XPS to check the coverage. Also heated sample to 450C and 650C. Saw no apparent change in surface by STM.
10/20/02	i-AlCuFe (ARR-4-8-a)	RHEED: ACF_rheed\102002	Several RHEED images collected at different angles and annealing temperatures.
10/22/02	i-AlCuFe (ARR-4-8-a)	RHEED: ACF_rheed\102202 XPS: ACF_xps UPS: ACF_ups	Collected more RHEED images. XPS and UPS data is confusing. Heater stage is not working properly.
10/23/02	i-AlCuFe (ARR-4-8-a)	XPS: ACF_xps UPS: ACF_ups	More confusing XPS and UPS data. Problem turns out to be with Sample-detector alignment.
10/24/02	i-AlCuFe (ARR-4-8-a)	RHEED: ACF_rheed\102402 XPS: ACF_xps UPS: ACF_ups	Began experiments to investigate effects of sputtering and annealing on surface structure.
10/25/02	i-AlCuFe (ARR-4-8-a)	RHEED: ACF_rheed\102502 XPS: ACF_xps UPS: ACF_ups	Continued surface structure experiments.

Table 2 (Continued)

Date	Sample	File Location	Experimental Notes and Comments
10/27/02	Pd (111) single crystal		Mounted and inserted sample into chamber. Began sputter and annealing cycles to clean surface.
10/28/02	Pd (111) single crystal		Continue cleaning cycles. STM shows large terraces, but still needs additional cleaning
10/29/02	Pd (111) single crystal	STM: Pd111\102902	Begin STM experiments. Files 1-6, clean surface. Files 7-14, first Pd dose. Files 15-19, second Pd dose. IV curves also collected.
10/30/02	Pd (111) single crystal	XPS: Pd111\Pd(111)_xps&ups UPS: Pd111\Pd(111)_xps&ups	Transferred sample to XPS chamber to collect XPS and UPS data.
10/30/02	Samples left in Japan for further experiments.		i-AlCuFe-5f-(ARR-4-8-a) ψ-AlCuFe-Hipped-(DJS-6-123-c) β-AlCuFe-Hipped-(DJS-6-121-d) ω-AlCuFe-Hipped-(DJS-7-21b) ξ'-AlPdMn-10f-(ARR-1-1-3a)

Table 2 (Continued)

Date	Substrate	File Location	Experimental Notes and Comments
3/20/02	Al (111)	STM-Ameslab\Al(111)\032002	Practicing using STM. Updated Omicron software to version 4.1
3/21/02	Ag (100)	STM-Ameslab\Ag(100)\032102	Dosing Al on Ag(100). Analysis of image m15 shows a dosing rate ~0.3ML/min.
3/22/02	i-AlCuFe-5f	STM-Ameslab\AlCuFe\032202	Dosing Al on i-AlCuFe. Analysis of image m22 and m25 shows a dosing rate of ~0.35ML/min. We see off-axis hexagonal islands (m68-m75), and rectangular islands (m78-m85). Summary of images on pg. 80 of notebook 2.
3/29/02	i-AlCuFe-5f	STM-Ameslab\AlCuFe\032902	Dosing Al on i-AlCuFe. Off-axis hexagonal islands again in different locations on the surface (m36-m49). They are all oriented in the same direction, but they appear to be oriented 72*2=144 degrees away from those seen on 3/22/02.
4/1/02	i-AlCuFe-5f	STM-Ameslab\AlCuFe\040102	Dosing Al on i-AlCuFe. Only see rectangular islands in this experiment.

Table 3

Date	Substrate	File Location	Experimental Notes and Comments
4/8/02	i-AlCuFe-5f	STM-Ameslab\AlCuFe\040802	Dosing Al on i-AlCuFe. See some rectangular islands. See a very large (~50nm) "crystal" with hexagaonal and rectangular facets. Summary of images begins on pg. 93 of notebook 2.
7/3/02	i-AlPdMn	STM-Ameslab\AlPdMn\070302	Dosing Al on i-AlPdMn. Long straight step-edges on clean surface. Still QC??? See some possible hexagonal islands, but images aren't very good.

Table 3 (Continued)

ACKNOWLEDGEMENTS

I would like to convey my sincere thanks to Professor Pat Thiel for all of her guidance and support. Pat, rather than trying to mold me into a copy of yourself, you have allowed me to evolve into a scientist that reflects who I am. You let me follow my interests and have provided me with fantastic opportunities. Thank you for permitting me to find my own path and for always being there when I needed guidance.

I also wish to thank Dr. Cynthia Jenks, Dr. Tony Layson, and Dr. Tanhong Cai for the assistance they have given me along the way. Thank you to Dr. Vincent Fournee. I have very much enjoyed the time we have spent together, and our discussions were always enlightening.

A very special thank you to my best friend and favorite colleague, Rachel Millen. You are the Hermione Granger of chemistry… always getting the A and making me look second best! You helped keep me motivated and smiling through it all. And without you, I probably never would have discovered the joy of monkeys in little plastic balls or the happiness that comes from fragging a bunch of bots with double cyclones. But most of all, I've enjoyed the time we've spent together doing nothing in particular, just talking about whatever and acting like a couple of goofballs.

Thank you to my Uncle Leonard Morel. You were always there to help my path seem brighter. You encouraged me to learn new things and to always keep an open mind. Thank you for always finding a way to buy the books I couldn't afford.

I would have never made it this far without the help of Paul Sasse and Michael Connor. You have both contributed so much to who I have become. Don't ever underestimate the power you have to shape the young minds in your classrooms. My recent achievements began with you, in those classrooms.

Thank you to Claudia Hein, Scott Hein, and Terry Ramus at Diablo Analytical, Inc. I learned to be an analytical chemist working for you before I even had my Bachelor's Degree. I was always surprised by how much you guys let me do. "Here's a drill, a schematic, and a brand new $40,000 instrument... go put it together!" The confidence you've shown in my abilities has given me greater confidence to this day.

To my beautiful wife, Christa: Thank you for being so supportive of me over the past eight years. Our love has inspired me to overcome many difficult challenges. And now, as I complete this chapter of my life, I look toward my future: raising our family, seeing Jacob grow, spending a lifetime with the woman I love... and it makes me happy.